Gating of the Hv1 proton channel

Dissertation

zur

Erlangung des Doktorgrades (Dr. rer. nat.)

der

Mathematisch-Naturwissenschaftlichen Fakultät

der

Rheinischen Friedrich-Wilhelms-Universität Bonn

vorgelegt von

Till Moritz Schladt

aus

Ingolstadt

Bonn 2021

Angefertigt mit Genehmigung der Mathematisch-Naturwissenschaftlichen Fakultät der
Rheinischen Friedrich-Wilhelms-Universität Bonn

1. Gutachter: Prof. Dr. U. Benjamin Kaupp
2. Gutachter: Prof. Dr. Günter Mayer

Tag der Promotion: 30.09.2021
Erscheinungsjahr: 2022

Hv1 ist ein spannungsgesteuerter protonenselektiver Ionenkanal, der unter anderem in Immunzellen an der Regulation des intrazellulären pH (pH_i) beteiligt ist. Unter den spannungsgesteuerten Ionenkanälen ist Hv1 einzigartig, da der Kanal keine klassische Porendomäne aufweist und seine Spannungssensordomäne (VSD) auch die Pore bildet. Damit unterscheidet sich seine Porenstruktur, sowie das Öffnen und Schließen der Pore (*Gating)* von klassischen, spannungsgesteuerten Ionenkanälen. Molekulare Mechanismen, die dem *Gating* zugrunde liegen, insbesondere die Kopplung von Spannungsdetektion und Porenöffnung, sind nicht gut verstanden. Im Rahmen dieser Arbeit benutzte ich gezieltes Quervernetzen (*Crosslinking*) von künstlich eingeführten Cystein-Seitenketten, um Interaktionen sowie Abstände und Abstandsänderungen zwischen einzelnen Aminosäureseitenketten zu messen. 1,1-Methanediyl Bismethanethiosulfonate (MTS-1-MTS) eignete sich zum *Crosslinking* von bestimmten Seitenketten in Transmembransegmenten S1 (151C) und S4 (262C) im geschlossenen Zustand des Kanals, was zeigte, dass sich die Cystein-Seitenketten während des Gatings auf 3-4 Å annähern. Durch Kombination von *Crosslinking* mit *Patch-Clamp*-Fluorometrie (PCF) konnte ich zeigen, dass die Quervernetzung die S1-Gatingbewegung blockiert. Weitere Experimente mit diesem kombinatorischen Ansatz werden zu unserem Verständnis von Struktur-Funktionsbeziehungen in Hv1 beitragen.

Das *Gating* von Hv1 wird neben der Membranspannung auch durch die Differenz zwischen extrazellulärem und intrazellulärem pH (ΔpH) gesteuert. Dabei sind ΔpH- und Spannungssteuerung derart gekoppelt, dass Hv1 nur öffnet, wenn der elektrochemische Protonengradient nach außen gerichtet ist. ΔpH-Detektion, sowie die Kopplung von ΔpH- und Spannungsdetektion sind auf molekularer Ebene nicht verstanden. Hier untersuchte ich den zugrunde liegenden Mechanismus in PCF-Experimenten durch ΔpH-Änderungen mittels Perfusion oder lichtgesteuerter Protonenfreisetzung. ΔpH-Änderungen führten zu Konformationsänderungen von S4, nicht jedoch von S1. Die Ergebnisse erlauben die Schlussfolgerung, dass S4 neben der Membranspannung auch ΔpH detektiert. Darüber hinaus konnte ich zeigen, dass S4 eines anderen spannungssensitiven Proteins (spannungsgesteuerte Phosphatase, VSP) nicht ΔpH gesteuert ist, was auf Hv1-spezifische Struktur-Funktionsbeziehungen zur Detektion von ΔpH hindeutet.

Abstract

Hv1 is a voltage-gated proton channel, which is involved in the regulation of the intracellular pH (pH_i) in immune cells. Among the voltage-gated ion channels, Hv1 is unique because it lacks a classical pore domain and its voltage-sensor domain (VSD) also forms the pore. Thus, its pore structure, as well as the opening and closing of the pore (gating), differs from classical voltage-gated ion channels. Molecular mechanisms underlying gating, in particular the coupling of voltage sensing and pore opening, are not well understood. In this thesis I used targeted crosslinking of engineered cysteine side chains to measure interactions, distances, and distance changes between amino-acid side chains. 1,1-methanediyl bismethanethiosulfonate (MTS-1-MTS) was suitable for crosslinking specific cysteine side chains in transmembrane segments S1 (151C) and S4 (262C) in the closed state of the channel, which showed that the cysteine side chains approached 3-4 Å during gating. By combining crosslinking with patch-clamp fluorometry (PCF), I was able to show that crosslinking blocks the S1 gating movement. In further experiments, this combinatorial approach will contribute to our understanding of structure-function relationships in Hv1.

In Hv1, gating is controlled not only by membrane voltage but also by the difference between extracellular and intracellular pH (ΔpH), being coupled such that Hv1 opens only when the electrochemical proton gradient is outwardly directed. The coupling between voltage- and ΔpH-sensing is not understood at the molecular level. Here, I investigated the underlying molecular mechanism in PCF experiments by altering the ΔpH by means of perfusion or light-controlled proton release. I could show that a ΔpH change can induce conformational changes of S4 but not of S1. The results are consistent with the idea that S4 can sense both voltage and ΔpH. Furthermore, I could show that S4 of another voltage-sensitive protein (voltage-gated phosphatase, VSP) is not sensitive to ΔpH, indicating Hv1-specific structure-function relationships for ΔpH sensing.

$[H^+]$	proton concentration
˚C	degree Celsius
ΔpH	pH gradient
A	ampere
aa	amino acid
bp	base pair
Ca^{2+}	calcium
$CaCO_3$	calcium carbonate
cDNA	complementary DNA
Ci	*Ciona intestinalis*
C-terminus	carboxyl-terminus
dd	double distilled
DMCM	(6,7-dimethoxycoumarin-4yl)methyl
DNA	deoxyribonucleic acid
dNTP	deoxynucleotide
E.coli	Escherichia coli
EDTA	ethylendiamintetraacetic acid
EGTA	ethylene glycol-bis(2-aminoethylether)-*N*,*N*,*N'*,*N'*-tetraacetic acid
E_H	equilibrium potential for protons
EtBr	ethidium bromide
F	fluorescence
F_{dark}	dark count (fluorescence signal with closed shutter)
FV	fluorescence-voltage relationship
g	gram
GV	conductance-voltage relationship
h	hour
H^+	proton
HCO_3^-	hydrogen carbonate
HEPES	4-(2-hydroxyethyl)-1-piperazineethanesulfonic acid
H_2O_2	hydrogen peroxide
I	current
K^+	potassium ion
kHz	kilo hertz
l	liter
Li^+	lithium
log	logarithm
LP	long pass filter
m	meter
M	molar
MES	2-(N-morpholino)ethanesulfonic acid
min	minute
mRNA	messenger ribonucleic acid
MSA	methane sulfonic acid

MTS-1-MTS	1,1-methanediyl bismethanethiosulfonate
Na^+	sodium ion
NMDG	N-methyl-D-glucamine
NPE-	1-(2-nitrophenyl)ethyl-
N-terminus	amino-terminus
PCF	patch-clamp fluorometry
PCR	polymerase chain reaction
PD	pore domain
pH	negative logarithm of proton concentration
pH_i	intracellular pH
pH_o	extracellular pH
RNA	ribonucleic acid
RNase	ribonuclease
ROS	reactive oxygen species
RT	room temperature
s	second
S	transmembrane segment
SCAM	substituted-cysteine accessibility method
TAMRA	2-((5(6)-Tetramethyl-rhodamine)carboxylamino)ethyl
TCEP	tris(2-carboxyethyl)phosphine
TEA Cl	tetraethylammonium chloride
TEA OH	tetraethylammonium hydroxide
Tm	melting temperature
Tris	tris(hydroxymethyl)aminomethane
UV-light	ultra violet light (365 nm wavelength)
V	voltage
VCF	voltage-clamp fluorometry
VGIC	voltage-gated ion channel
V_m	membrane potential
VSD	voltage-sensing domain
VSP	voltage-sensing phosphatase
WT	wild type: ciHv1
Ω	Ohm

Amino Acids:

A / Ala	Alanine	L / Leu	Leucine
R / Arg	Arginine	K / Lys	Lysine
N / Asn	Asparagine	M / Met	Methionine
D / Asp	Aspartic acid	F / Phe	Phenylalanine
C / Cys	Cysteine	P / Pro	Proline
Q / Gln	Glutamine	S / Ser	Serine
E / Glu	Glutamic acid	T / Thr	Threonine
G / Gly	Glycine	W / Tyr	Tryptophan
H / His	Histidine	Y / Tyr	Tyrosine
I / Ile	Isoleucine	V / Val	Valine

1. Introduction

In organisms throughout the phylogenetic tree, voltage-gated ion channels (VGICs) generate electrical signals. They play an important role in sensory transduction, neurotransmitter release, endocrine secretion, and other physiologic processes (Hille, 2001; Yu & Catterall, 2004). VGICs open their ion-selective pore in response to membrane potential changes and allow permeant ions to cross the membrane, driven by the ion´s electrochemical driving force.

The first channel genes were identified from Na^+, K^+, and Ca^{2+} selective voltage-gated ion channels (Na_V, K_V, Ca_V, respectively) (Noda *et al.*, 1984; Tempel *et al.*, 1987; Tanabe *et al.*, 1987), and are also referred to as classical VGICs.

1.1. Expression and physiological role of Hv1

In 2006, the gene HVCN1, coding for the voltage-gated proton channel Hv1, was identified and cloned (Ramsey *et al.*, 2006; Sasaki *et al.*, 2006). Hv1 is expressed by a plethora of organisms (Taylor *et al.*, 2011; Smith *et al.*, 2011). So far, the physiological role of Hv1 was studied mainly in marine single-cell organisms and mammals (for review (DeCoursey, 2013)): in bioluminescent dinoflagellates (i.e. *Lingulodinium polyedrum*), Hv1 triggers the acid-induced production of light by conducting protons into organelles called scintillions (Rodriguez *et al.*, 2017). In calcifying phytoplankton (i.e. *Coccolithus pelagicus*), Hv1 is suggested to regulate the production of calcium carbonate structures (calcification). During calcification, according to the chemical reaction:

$$HCO_3^- + Ca^{2+} \longrightarrow CaCO_3 + H^+,$$

protons accumulate inside the cell, which decreases the calcification rate. By conducting protons out of the cell, Hv1 sustains calcification (Taylor *et al.*, 2011).

In humans, Hv1 is expressed in several immune cells (Ramsey *et al.*, 2009; Capasso *et al.*, 2010), lung epithelial cells (Iovannisci *et al.*, 2010), and sperm (Lishko *et al.*, 2010). Evidence has been found indicating that Hv1 regulates B-cell proliferation (Capasso *et al.*, 2010), the pH of the airway surface liquid at the airway epithelium (Iovannisci *et al.*, 2010), and sperm maturation (Lishko *et al.*, 2010). The physiological role of Hv1 in humans is best understood in macrophages,

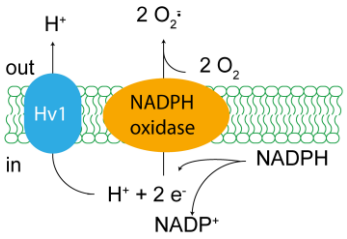

Figure 1.1. Physiological role of Hv1 in macrophages. Hv1 compensates membrane depolarization and counteracts intracellular acidification during the respiratory burst, which prolongs NADPH-oxidase activity.

where the channel regulates the production of the reactive oxygen species (ROS) as innate immune response to pathogens. To produce ROS, Nicotinamide adenine dinucleotide phosphate reduced form (NADPH) oxidase oxidizes NADPH to $NADP^+$. During this process, a proton is released into the cytosol and two electrons are released and transported via an electron transport chain across the membrane to reduce molecular oxygen into superoxide (Fig. 1.1). This process depolarizes the membrane and acidifies the cytosol, which is both self-limiting to NADPH oxidase. Hv1-mediated outward proton conduction repolarizes the membrane, counteracts acidification, and thereby sustains ROS production (Fig. 1.1) (Ramsey *et al.*, 2009; Morgan *et al.*, 2009; El Chemaly *et al.*, 2010).

Excessive Hv1 activity might have pathological consequences. In a mouse model of ischemic stroke, Hv1-dependent ROS production worsens brain damage (Wu *et al.*, 2012). Hv1 is overexpressed in breast-cancer cells (Wang *et al.*, 2012) and malignant B-lymphocytes (Hondares *et al.*, 2014). In most tissues and cells expressing Hv1, the channel exerts its physiological or pathophysiological role by outward-directed proton conduction (see (Smith *et al.*, 2011) for an exception).

1.2. Architecture and gating of VGICs and Hv1

Classical VGICs comprise a voltage-sensor domain (VSD), consisting of four transmembrane segments (S1-S4), which is coupled via the S4-S5 linker to a pore domain (PD), consisting of two transmembrane segments (S5 and S6) and the P-loop in between. A series of positively charged amino acids (arginine or lysine) at every third position along the S4 segment confer sensitivity to voltage (Aggarwal & MacKinnon, 1996; Seoh *et al.*, 1996); depolarization of the membrane displaces the S4 segment towards the extracellular side of the membrane (Yang & Horn, 1995; Mannuzzu *et al.*, 1996; Cha & Bezanilla, 1997; Starace *et al.*, 1997). The P-loop contains the

selectivity filter, a characteristic motif of amino acids that determines which ion species can permeate. Four subunits assemble such that the four PDs form one central pore (Fig. 1.2A, *left*).

Depolarization of the membrane opens the channel pore. Open- and closed-state structures (Lenaeus *et al.*, 2017); (Payandeh *et al.*, 2011; Wisedchaisri *et al.*, 2019) of the bacterial voltage-gated Na^+ channel from *Arcobacter butzleri*, Na_vAb, provide insight into the opening and closing mechanisms of the pore (gating) and provide a gating model for classical voltage-gated ion channels. In all four subunits, depolarization of the membrane translocates the S4 segments towards the extracellular side (Lenaeus *et al.*, 2017; Wisedchaisri *et al.*, 2019). In consequence, the S4 displacement pulls the S4-S5 linkers towards the membrane surface (Fig. 1.3A, *middle*) (Wisedchaisri *et al.*, 2019) and opens the pore by concerted subtle conformational changes of the four S6 segments in the pore domain (Lenaeus *et al.*, 2017; Wisedchaisri *et al.*, 2019) (Fig. 1.3 A, *left*).

In contrast to classical VGICs, Hv1 consists only of S1-S4, which is homologous to classical VSDs, i.e. Hv1 lacks a classical pore domain (Fig. 1.2A, *right*) (Ramsey *et al.*, 2006; Sasaki *et al.*, 2006). Instead of a tetramer, Hv1 forms dimers (Koch *et al.*, 2008; Lee *et al.*, 2008; Tombola *et al.*, 2008). Reconstituted Hv1 is functional in liposomes (Lee *et al.*, 2009), showing that no other accessory subunits are needed to form the pore. Dimerization is mediated mainly by the C-terminus, as its deletion yields Hv1 monomers (Tombola *et al.*, 2008; Koch *et al.*, 2008; Fujiwara *et al.*, 2012). Heterologously expressed Hv1 monomers conduct protons (Tombola *et al.*, 2008; Koch *et al.*, 2008), showing that S1-S4 harbor the pore for proton permeation (Fig. 1.2A, *right*). In summary, the pore structure, ion conduction, and gating of Hv1 are different compared to classical VGICs. The X-ray crystal structure of the chimeric construct mHv1cc, consisting of mouse Hv1, *Ciona intestinalis* voltage-sensing phosphatase (ciVSP), and *Saccharomyces cerevisiae* transcriptional activator GCN4, is the only structure available that provides information on the arrangement of S1-S4 (Fig. 1.2B) (Takeshita *et al.*, 2014) and provided guidance for functional studies. However, side chains are not resolved and the structure supposedly represents an intermediate-resting state. High-resolution structures of full-length Hv1 in closed and open states are still lacking, and the molecular mechanisms underlying gating in Hv1 remain obscure.

Functional data indicate that S4, like in other VGICs, constitutes the main voltage sensor. Three arginine residues - one in every third position along the S4 segment - confer voltage

sensitivity (Gonzalez *et al.*, 2013). The S4 segment moves towards the extracellular side during depolarization (Fig. 1.3B, *middle*) (Gonzalez *et al.*, 2010) followed by movement of S1 (Mony *et al.*, 2015); this movement seems to be involved in the final gating step of activation that opens the pore (Fig. 1.3B, *right*). As the VSD of Hv1 is the only membrane spanning region, the pore with the permeation pathway, selectivity filter, as well as the gate must be located along the voltage sensor in the VSD. This stands in contrast to the pore in classical VGICS, being separated from the voltage sensor and gate. It is proposed that, the conformational changes of S4 and S1 in Hv1 translate membrane depolarization into pore opening by aligning residues in S4 and S1 to *form* the selectivity filter and permeation pathway in the open state (Berger & Isacoff, 2011). At least two residues seem to be involved in the formation of the selectivity filter during the transition from the closed to the open state and are supposed to localize the pore: a highly conserved aspartate in S1 (D112 in human Hv1) (Musset *et al.*, 2011) and an arginine in S4 (R211 in human Hv1) (Berger & Isacoff, 2011) determine proton selectivity and seem to interact in the open state (Berger & Isacoff, 2011). The structure of the pore remains unresolved and gating of the pore, namely how voltage sensing is coupled to pore opening in Hv1 is not well understood. Using the open-channel blocker 2-guanidiniumbenzimidazole (2GBI), a vestibule on the intracellular side, in the open state was revealed (Hong *et al.*, 2013). The state dependence of the block may result from the widening of the intracellular vestibule during opening, suggesting an intracellular gate.

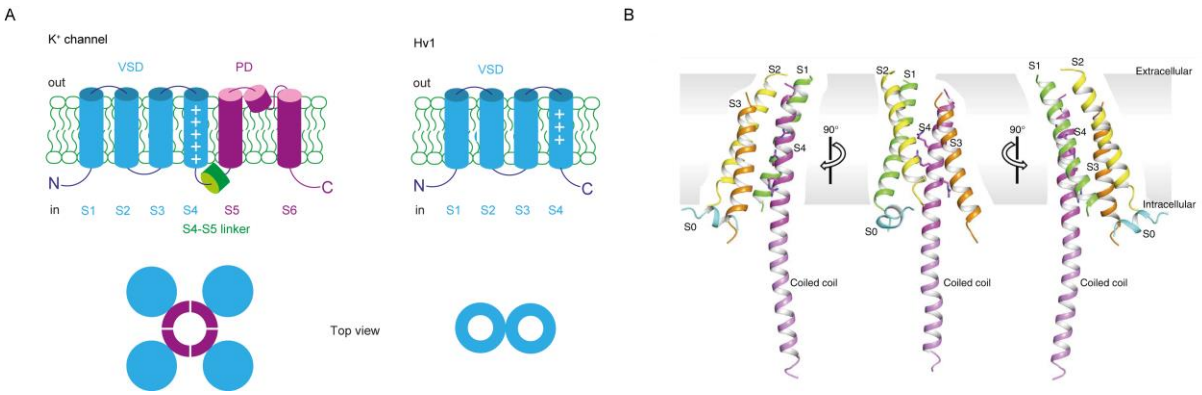

Figure 1.2. Architecture of Hv1 and Kv. *A*, *left*, architecture of classical voltage-gated potassium channels consisting of VSD and PD. *Bottom left*, the permeation pathway for potassium is formed by four pore domains. *Right*, Hv1 consists of four transmembrane segments (S1 to S4) forming the VSD and lacks a PD. Three regularly spaced arginines (+) on S4 constitute the voltage sensor. *Bottom right*, the permeation pathway for protons is located within the VSD. *B*, X-ray crystal

structure of a protomer of mHv1cc, viewed parallel to the membrane from three different angles rotated 90° along the vertical axis. The four transmembrane segments S1 (green), S2 (yellow), S3 (orange) and S4 (magenta) connected to the cytoplasmic coiled-coil region (pink) and the N-terminal cytoplasmic helix S0 (cyan) are shown. Three arginine residues (Arg201, Arg204 and Arg207) in S4 are shown as stick models. Panel B adapted from (Takeshita et al., 2014).

Hv1 is highly selective for protons, favoring protons more than 10^6 times over K^+ and Na^+ [for review (DeCoursey, 2003)]. The molecular mechanism underlying proton-specific conduction in Hv1 is currently under debate (Bennett & Ramsey, 2017*a*, 2017*b*; DeCoursey, 2017*a*, 2017*b*). Conduction might occur via proton transfer, involving a transient protonation of the aspartate D112 (Musset *et al.*, 2011), or Grotthuss-type proton hopping via a continuous network of water molecules ("wire"), which is stabilized by surrounding amino acids in a narrow pore (Ramsey *et al.*, 2010).

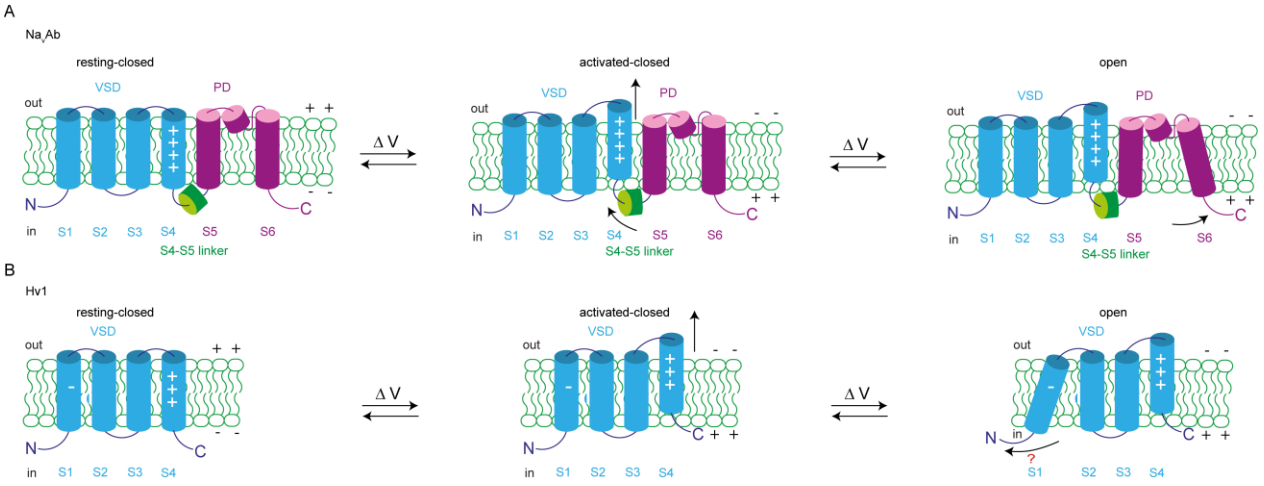

Figure 1.3. Gating scheme of Hv1. *A, left-right,* cartoon of a single Na_vAb subunit, depicting voltage-evoked conformational changes which open the channel pore. Depolarization pushes the S4 segment towards the extracellular side of the membrane (*middle*), which triggers a conformational change of the S4-S5 linker (green) (*middle*) and subtle conformational changes of the S6 segment in the pore domain (*right*). *B, left-right,* cartoon of an Hv1 protomer, depicting voltage-evoked conformational changes which are supposed to open the channel pore: Depolarization pushes the S4 segment towards the extracellular side of the membrane (*middle*) and subsequent S1 conformational change occurs with the actual pore opening (*right*). For clarity, only S4 and S1 are shown. "+" signs on S4 denote the positively charged arginines on S4, "-" sign on S1 denotes a negatively charged aspartate on S1 (D112 in human Hv1).

The Hv1 channel only opens when the electrochemical gradient is directed towards the extracellular side. This outward rectification is achieved as Hv1 is not only gated by membrane potential, but also by the pH difference across the membrane ($\Delta pH = pH_o - pH_i$). At $\Delta pH = 0$, Hv1 starts to open at +10 to +30 mV (Musset *et al.*, 2008). The activation curve is shifted by approximately 40 mV/ΔpH unit to more negative and positive potentials for $\Delta pH > 0$ and < 0, respectively (40 mV rule) (Fig. 1.4) (Cherny *et al.*, 1995).

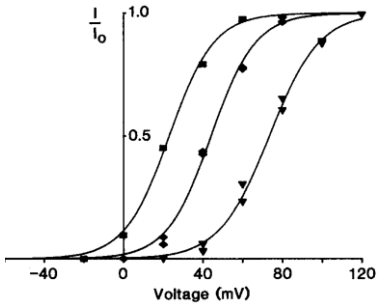

Figure 1.4. Voltage dependence of Hv1 is coupled to the difference between pH_o and pH_i (ΔpH). Conductance-voltage relationships in a cell at pH_i 6.5 and three different pH_o, fitted with Boltzmann function and normalized to the fitted maximum. *Left,* pH_o 7.5: $V_{1/2}$ = 23.1; *middle,* pH_o 7.0: $V_{1/2}$ = 44.3; *right,* pH_o 6.5: $V_{1/2}$ = 73.5 mV [taken from (Cherny *et al.*, 1995)].

By contrast, changes in pH_o or pH_i that leave ΔpH constant do not alter the voltage dependence of activation. The amino-acid residues that convey ΔpH sensing remain elusive. Although mutants with enhanced or diminished ΔpH sensing have been identified (Ramsey *et al.*, 2010; Cherny *et al.*, 2015, 2018), no mutants are known that lack ΔpH sensing entirely. Voltage- and ΔpH-dependent gating as well as the coupling of both is not understood. So far, Hv1 carries the only known VSD that is sensitive to ΔpH. However, it is not clear whether other VSDs are either ΔpH insensitive, or whether ΔpH sensitivity is not relayed to the pore (effector domain) and, therefore, escaped from being detected.

1.3. Aim of this thesis

Hv1 is a unique member of the superfamily of VGICs, because its VSD also contains the pore. Gating of the pore, distances and interactions between residues within the gate, as well as the mechanism underlying ΔpH sensing and its coupling to voltage sensing, are not well understood.

In the first part of my thesis, I developed a novel approach to study channel gating by combining crosslinking with electrophysiological techniques. In the second part, I studied the molecular mechanism underlying the coupling of voltage- and ΔpH sensing in ciHv1. In the last part, I studied the pH sensitivity of the VSD of the voltage-sensing phosphatase (VSP), another

voltage-sensing protein, to test whether ΔpH sensing is specific to Hv1. This thesis addresses the following questions:

- How can distances between residues and conformational changes that open Hv1 be measured?
- How is ΔpH sensed by Hv1?

To this end, I used different electrophysiological, optical, photolytic, biochemical, and molecular techniques

2. Material and Methods

2.1. Molecular Methods

2.1.1. Site-directed mutagenesis

CiHv1 (accession number NP_001071937), ciVSP (accession number NM_001033826.1) and mutant DNAs were used in the pSD64TF vector [for ciHv1 constructs (Sasaki *et al.*, 2006); for ciVSP constructs (Murata *et al.*, 2005)] for amplification and *in vitro* transcription. Point mutations were introduced in a polymerase-chain reaction (PCR) by primer mismatch following the QuickChange strategy (Stratagene, La Jolla, CA, USA).

Construct	**Primer sequence (5'--3')**	**Reading direction**
ciHv1-H150C	CATTCTAAACCAATATGTGTTGCAATCATAGTCC	forward
	GGACTATGATTGCAACACATATTGGTTTAGAATG	reverse
ciHv1-V151C	CTAAACCAATACATTGTGCAATCATAGTC	forward
	GACTATGATTGCACAATGTATTGGTTTAG	reverse
ciHv1-I153C	CAATACATGTTGCATGCATAGTCCTAGTAG	forward
	CTACTAGGACTATGCATGCAACATGTATTG	reverse
ciHv1-I154C	CATGTTGCAATCTGTGTCCTAGTAGTG	forward
	CACTACTAGGACACAGATTGCAACATG	reverse
ciHv1-V157C	CAATCATAGTCCTATGTGTGTTGGACAGTTTC	forward
	GAAACTGTCCAACACACATAGGACTATGATTG	reverse
ciHv1-I175C	GACCTCAAAGTATGTATTGTACCACATG	forward
	CATGTGGTACAATACATACTTTGAGGTC	reverse
ciHv1-I202C	CAATATTTATGGTGGAATGCGCTTTGAAGATAATC	forward
	GATTATCTTCAAAGCGCATTCCACCATAAATATTG	reverse
ciHv1-K205C	GGTGGAAATCGCTTTGTGCATAATCGCCGATC	forward
	GATCGGCGATTATGCACAAAGCGATTTCCACC	reverse
ciHv1-V226C	GTTGGATGCGGTTGTCTGCGTGATATCGTTCGGTG	forward

	CACCGAACGATATCACGCAGACAACCGCATCCAAC	reverse
ciHv1-L245C	GAGAGTGAAGCCTGCGCTGCTATCGGAC	forward
	GTCCGATAGCAGCGCAGGCTTCACTCTC	reverse
ciHv1-I262C	GTCTTCAGATGCATTAATGGTATC	forward
	GATACCATTAATGCATCTGAAGAC	reverse
ciHv1-N264C	CTTCAGAATCATTTGTGGTATCATCGTAAC	forward
	GTTACGATGATACCACAAATGATTCTGAAG	reverse
ciVSP-G214C	GAAACAGGAGCCGATTGTTTGGGGAGATTG	forward
	CAATCTCCCCAAACAATCGGCTCCTGTTTC	reverse

Table 1. Forward and reverse primer for site-directed mutagenesis. Primers were purchased at Eurofins Genomics GmbH (Ebersberg, Germany).

KOD Hot Start DNA polymerase (Novagen, Billerica, MA, USA) was used for mutagenesis. The reaction mixture was assembled on ice as described in Table 2.

Chemical	**Volume**
ddH_2O	35.5 µl
KOD Polymerase buffer (10 x)	5 µl
dNTP	5 µl
$MgSO_4$	2 µl
Reverse primer (10 µM)	1 µl
Forward primer (10 µM)	1 µl
DNA of pSD64TF ciHv1 constructs	0.2 µl
KOD polymerase	1 µl

Table 2. Pipetting scheme for PCR.

All PCRs were performed using the protocol described in Table 3.

Phase	Temperature	Duration (minutes)	Iterations
Initial denaturation	95°C	3:20	1x
Denaturation	95°C	1:00	26x
Annealing	51 - 61°C	1:00	26x
Elongation	72°C	2:00-3:00	26x
Final elongation	72°C	10:00	1x
Termination	8°C	∞	1x

Table 3. PCR protocol.

After mutagenesis PCR, 1.5 µl DpnI, a methylation-sensitive restriction enzyme, was added to the samples and incubated for 1.5 h at 37 °C. DpnI cleaves only the methylated template DNA originating from bacterial replication. Unmethylated mutated DNA originating from the *in vitro* PCR remains intact.

2.1.2. Amplification

Chemical	Volume
XL Blue	40 µl
ddH_2O	54.5 µl
10 x CM-buffer (400 mM $CaCl_2$, 100 mM $MgCl_2$)	5 µl
DNA from PCR (DNA in case of retransformation)	5 µl (0.5 µl)

Table 4. Pipetting scheme for DNA transformation.

Via transformation, DNA constructs were taken up by competent XL1-Blue *E. coli* cells: XL1-Blue cells (stored at 80°C) were thawed on ice. DNA together with buffer containing $CaCl_2$ and $MgCl_2$ (CM-buffer, Table 4) was pipetted to the cells (see pipetting scheme in Table 4) and the suspension was incubated 15 minutes on ice, followed by a heat shock of one minute at 42 °C and incubation for five minutes on ice. 100 µl of the cell suspension was plated on an ampicillin-containing LB-medium plate (LB medium, 15 g/l agar; 100 µg/ml ampicillin) and incubated over night at 37°C. Colonies were picked and added to 5 ml LB medium containing 10 µl ampicillin. The cell suspension was incubated over night at 37°C in a stirring rack.

2.1.3. Mini-preparation of plasmid DNA

The cell suspension was centrifuged for 30 s at 11.000 x g. The supernatant was discarded. Pellet resuspension, cells lysis and DNA isolation was done with the NucleoSpin Plasmid Miniprep Kit (Macherey-Nagel, Düren, Germany) following the standard protocol. Subsequently, the DNA was eluted in 50 µl ddH_2O (expected DNA concentration: >1 µg/µl). All DNA constructs were sequenced (Eurofins Genomics GmbH, Ebersberg, Germany).

2.1.4. *In vitro* transcription

Chemical	**Volume or mass**
DNA	5 µg
Cut Smart enzyme buffer	10 µl
SacI	1 µl
ddH_2O	Adj to 100 µl

Table 5. Pipetting scheme for restriction digest.

Prior to *in vitro* transcription (IVT), DNA constructs in the pSD64TF vector were linearized by the restriction enzyme SacI (New England Biolabs, Frankfurt, Germany). The pipetting scheme for the restriction digest is shown in Table 5. The reaction was incubated for 1.5 h at 37 °C.

The Nucleospin Gel and PCR Clean-up kit (Macherey-Nagel) was used to purify the linearized DNA (L-DNA), following the manufacturer´s protocol. The L-DNA was eluted with 30 µl RNAse-free water (Ambion) into an RNAse-free reaction tube. Residual ethanol was removed by incubation for 5 minutes in a pre-heated vacuum-concentrator centrifuge (Univapo 150H, Uniequip, Planegg, Germany). L-DNA concentration was measured via NanoDrop (ND-1000 spectrophotometer). Successful purification yielded > 0.1 µg/µl L-DNA. The purified L-DNA was transcribed (see Table 6) using the SP6 mMessage mMachine kit (Ambion, Austin, TX, USA). Work space was kept RNAse free. The (IVT) reaction was incubated for 4-5 hours at 37 °C. To stop the reaction and to precipitate RNA, 30 µl LiCl precipitation solution (7.5 M LiCl and 50 mM EDTA,

Chemical	Volume
Linearized DNA (roughly 1 µg)	6 µl
(2x) NTP mix	10 µl
(10x) Buffer	2 µl
Enzyme (SP6)	2 µl

Table 6. Pipetting scheme for *in vitro* transcription.

Ambion) was pre-mixed with 30 µl RNase free water and added to the IVT reaction. The precipitation was incubated at -20 °C to -25 °C overnight. To purify the precipitated mRNA, the IVT reaction was centrifuged for 60 minutes at 16000 x g and 4 °C. The supernatant was discarded and the pellet was washed three times with 500 µl ethanol (70 %, 200 proof, premixed with RNAse-free DEPC H_2O) and centrifuged for 5 minutes at 16000 x g and 4 °C. After the last washing step, the supernatant was discarded and the pellet was dried for more than 10 minutes at 37 °C to remove residual ethanol. The pellet was resuspended in 15 µl RNAse free water (Ambion). For all pipette steps handling mRNA, only RNAse-free tips were used. The quality of mRNA was checked by gel-electrophoresis (1% agarose in TEA buffer: 40 mM tris/acetate, 1 mM EGTA, 1 µg/ml ethidium bromide, pH 7.5).

2.2. *Xenopus* oocytes preparation and heterologous expression

Chemical	Concentration (mM)
NaCl	96
KCl	2
$CaCl_2$	1.8
$MgCl_2$	1
(HEPES)	10
Na-pyruvate	5
gentamicin	100 mg/l
NaOH	adjusted to pH 7.5

Table 7. ND 96 medium for *X. laevis* oocytes.

In this thesis, frog oocytes from *Xenopus laevis* served as expression system. Oocytes were provided by Christopher Volk (Bonn-Rhein-Sieg University of Applied Sciences, Sankt Augustin, Germany), purchased from Ecocyte (Castrop-Rauxel, Germany), or harvested from the in-house colony: frog surgery followed standard procedures and was in agreement with the animal testing approval 84-02.04.2016.A077. To introduce the gene of interest, oocytes were injected with 50 nl mRNA (0.25–2 µg/µl) by a nano-injector apparatus (Nanoliter2010, World Precision Instruments Europe, Berlin, Germany) and incubated at 14–16 °C for 1–7 days in ND96 medium (Table 7).

2.3. Patch-clamp technique

With the patch-clamp technique, a small patch of membrane is electrically isolated by a fire-polished glass capillary pressed against the surface of the cell membrane. With this technique, a current can be measured with high resolution from the isolated area (Neher & Sakmann, 1976). By applying negative pressure to the pipette interior, sucking at the membrane, a seal of high electrical resistance (tens of gigaohms) and of mechanical stability is formed (Sigworth & Neher, 1980). This so called "gigaseal" is crucial to reduce noise, coming from leak currents between membrane and patch pipette. The pipette is in the so called on-cell or cell-attached recording configuration (Fig. 2.1, *top left*).

2.3.1. Excised-patch configurations

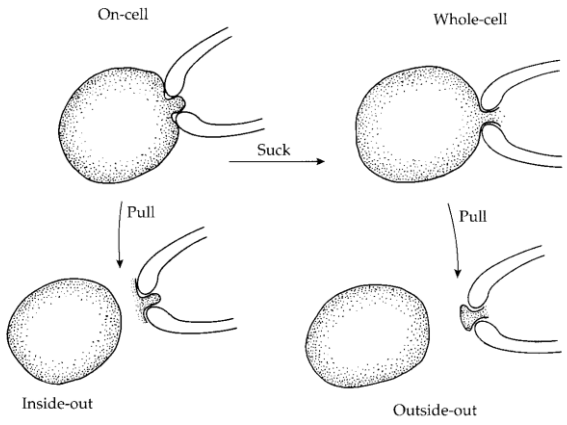

Figure 2.1. Different recording configurations. Drawing taken from (Hille, 2001).

In the on-cell configuration the patch is mechanically so stable that the patch can be pulled off the cell, still sealed to the pipette, giving the excised inside-out configuration (Fig. 2.1, *bottom left*) (Hamill & Sakmann, 1981; Hamill *et al.*, 1981). Now the inner side of the membrane faces the solution in the chamber and can be washed with different test solutions. Instead of pulling the patch pipette from the membrane in the on-cell configuration, one can apply suction to break the membrane with the pipette still sealed to the cell. This results in the whole-cell configuration (Fig. 2.1, *top right*). Pulling the pipette away from the cell membrane will excise a patch of membrane in the outside-out configuration (Fig. 2.1, *bottom right*) (Hamill *et al.*, 1981). All patch-clamp experiments in this thesis are performed in the inside-out or outside-out configuration.

2.3.2. Patch-clamp setup and electrophysiological recordings

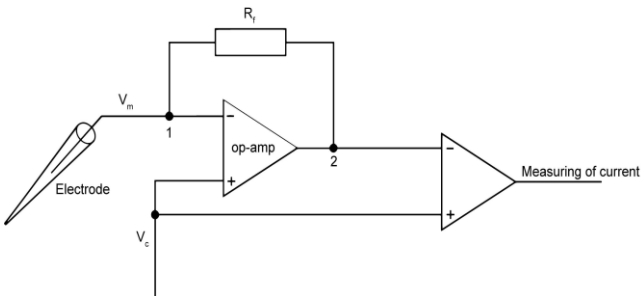

Figure 2.2. Electric circuit underlying the patch-clamp technique. Detailed description in text; adapted from (Hamill *et al.*, 1981).

With the patch-clamp technique the actual membrane potential (V_m) can be clamped to a desired command potential (V_c) by injecting a current (I). One crucial element of the electric circuit is the pre-amplifier located at the head stage. It consists of the operational differential amplifier (op-amp) and the feedback resistance (R_f) (Fig. 2.2). V_m is applied at the anode, the Vc at the cathode of the op-amp.

As soon as V_m differs to V_c, the op-amp creates a potential at its output, V_{out} (point 2 in Fig. 2.2), which is proportional to the potential difference between V_m and V_c, but amplified with a factor x:

$$V_{out} = x\,(V_c - V_m)$$

In this case, a potential difference between points 1 and 2 (in Fig. 2.2) exists, and I can flow over R_f:

$$I = \frac{V_{out}}{R_f}$$

As there is a high resistance at the input of the op-amp, the current can only flow through the electrode via the $AgCl_2$-wire to the membrane patch, adjusting V_m to V_c. By this circuit, V_m is clamped to V_c. The necessary injected current is the recorded current signal. A positive membrane voltage means that the intracellular side of the membrane is charged positively, while the extracellular side is charged negatively and *vice versa*. Cations that flow from the intracellular to the extracellular side of the patch constitute an outward current, and *vice versa*.

An inverted IX71 microscope (Olympus, Tokyo, Japan) equipped with a 10x or 20x objective was mounted on top of a vibration-dampened table, protected from electromagnetic fields by a Faraday cage. By two micromanipulators (Scientifica, Uckfield, UK) the recording chamber and the head stage with the patch pipette were moved under the microscope into the field of view. The recording chamber was connected to a gravity-driven perfusion system. A

reference electrode ($AgCl_2$) was connected to the solution in the recording chamber via an agar bridge containing 3M KCl. The pipette solution was electrically coupled to the pre-amplifier via a patch-pipette electrode ($AgCl_2$).

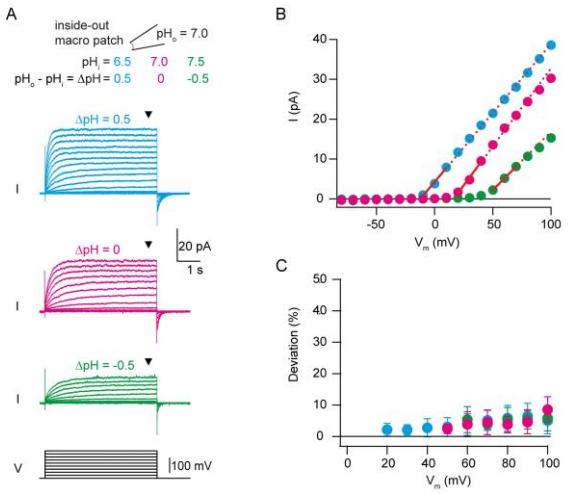

Figure 2.3. Control of pH during excised giant patch-clamp recordings. *A*, inside-out patch-clamp recordings from oocytes expressing ciHv1 at different ΔpH conditions. *B*, IVs derived from steady-state currents (at time points specified by triangles in A) at different ΔpH conditions, fitted with a linear function (red line). The dashed line is an extrapolation of the linear fit. *C*, deviation of I from extrapolated linear fit as a function of V_m, normalized to I.

Patch pipettes were pulled from 1.5 mm thick borosilicate glass capillaries (Hilgenberg, Malsfeld, Germany) on a DMZ puller (Zeitz Instruments GmbH, Martinsried, Germany) and subsequently fire polished with a Narishige MF-830 microforge (Narishige, Tokyo, Japan). The resulting initial electrode resistance was 0.6–1.5 MΩ (about 10–30 µm inner tip diameter) in the used recording solutions. Prior to recording, oocytes were mechanically devitellinated under a stereoscope (SMZ045, Nikon, Tokyo, Japan) using fine forceps and then placed into the recording chamber. Excised macro patches were obtained within seconds to minutes. Holding potentials were 60 or – 80 mV. Recordings were performed at room temperature (RT, 22–25°C) using an Axopatch 200B amplifier (Molecular Devices, Union City, CA, USA), connected to a PC running pClamp 10 (Molecular Devices) via a Digidata 1440A acquisition board. Data were filtered at 2 or 5 kHz and the sampling rate was 10 kHz.

Large proton currents via proton channels can lead to accumulation or depletion of protons at either side of the membrane, thereby changing the pH in the vicinity of the proton channel (De-la-Rosa *et al.*, 2016). As a consequence, the electrochemical driving force for protons can change (reduction for outward currents during channel activation), precluding stable recording conditions. In order to keep the pH during Hv1 activation as stable as possible, recording solutions contained high pH buffer concentrations (100 mM, see Table 8), patch pipettes with large tip diameters were pulled to obtain a large pH-buffer volume-to-membrane surface ratio,

and only oocytes with low Hv1 expression levels were considered for experiments to record rather small proton currents. To estimate the error due to changes in pH in my recordings, the deviation of the linear extrapolation of small outward current amplitudes was compared with the outward current amplitudes in response to the large voltage steps (Fig. 2.3B). The deviations did not exceed 8.6 % for the maximal stimulation amplitude (Fig. 2.3C). CiHv1 displays robust heterologous expression (Gonzalez *et al*., 2010) and faster activation kinetics than human Hv1, which facilitates data acquisition.

2.3.3. Patch-clamp fluorometry

The study of conformational changes in ion channels by electrophysiological methods is limited to structural rearrangements that move charges or dipoles in the membrane electric field, or open the channels permeation pathway. Optical methods based on site-specific labeling of ion channels using environmentally-sensitive fluorophores allow to study conformational changes directly. For this purpose, a cysteine mutation is introduced into the channel by site-directed mutagenesis at the site of interest (see 2.1.1). In the membrane-embedded cysteine-mutant channel, the introduced cysteine is then modified (labeled) with a thiol-reactive environmentally-sensitive fluorophore. Environmental changes around the fluorophore, such as a changed distance to quenching groups of other parts of the protein (e.g. a charged amino acid) and/or exposure to different solvents (e.g. when moving from a hydrophobic membranous environment to a more hydrophilic aqueous environment) change the fluorescence-emission intensity in real time. Thereby structural rearrangements during channel gating can be reported in real time. Mannuzzu *et al.* (1996) combined the site-specific fluorescent labeling, with the voltage-clamp technique. This so called voltage-clamp fluorometry (VCF) technique allows for measuring structural rearrangements with sub-millisecond resolution, while controlling the gating state of VGICs. Zheng & Zagotta (2000) modified VCF to develop the patch-clamp fluorometry (PCF): instead of whole-cell voltage clamp, they combined excised inside-out patch clamping with fluorometry, which adds the advantage of controlling both, the extracellular and intracellular milieu. PCF has proven useful to identify and measure gating motions in real time in Hv1 channels (Berger & Isacoff, 2015; Mony *et al.*, 2015).

Here, as in mentioned PCF studies with Hv1, I used 2-((5(6)-Tetramethyl-rhodamine)carboxylamino)ethyl methanethiosulfonate (MTS-TAMRA) (Figure 2.4A) for site-specific labeling of the channels in PCF experiments. To better understand the mechanism underlying fluorescence changes of TAMRA, I measured its absorbance using the UV-VIS-NIR spectrophotometer 5000 (Varian, acquired by Agilent Technologies, Santa Clara, USA), and emission using a photometer [Photon Technology International (PTI), Birmingham, New Jersey, USA] with the DeltaRam X monochromator (PTI). Absorbance and emission was measured in solvents with different polarities (Fig. 2.4B). Both, absorbance (543 nm) as well as emission (572 nm) in ethanol (dielectric constant ε = 24), shifted about 10 nm towards longer wave lengths when measured in water, a more polar solvent (ε = 78) (Fig. 2.4B). These rather small red shifts of TAMRAs absorbance and emission did not result in an increased Stokes shift. However, emission intensity in water was five times lower compared to the intensity in ethanol (Fig. 2.4B, *right*), suggesting that (collisional) quenching (Fig. 2C), probably by oxygen, is involved. Therefore, TAMRA-fluorescence changes seen in PCF experiments might result from changed emission intensity (quantum yield) due to differential collisional quenching in different environments such as in water, membrane, or other parts of the channel. This mechanism also underlies tetramethylrhodamine maleimide (TMRM)-fluorescence changes in VCF experiments with *Shaker* potassium channels (Cha & Bezanilla, 1997).

Importantly, pH did not have an effect on TAMRA absorbance and emission peaks; no changes in water, buffered to different pH was observed (Fig. 2.4B). These results show that TAMRA can be used in PCF experiments to track conformational changes at different pH.

TAMRA binds covalently to the cysteine forming a disulfide bridge. As TAMRA is added to an aqueous labeling solution, the cysteine needs to be solvent exposed. For TAMRA labeling, single cysteines were introduced either at positions I175C (in ciHv1, labeling on S1), L245C (ciHv1, labeling S4) or G214C (ciVSP, labeling S4). Oocytes were injected with mRNA 5 to 7 days prior to the recording. On the day of recording, oocytes were labeled at 4 °C for 40–60 min in a depolarizing, high potassium labeling solution (Table 10) containing 0.05 mM MTS-TAMRA. Subsequently, oocytes were washed three times in ND96 and stored at 12 °C until recording. PCF experiments were performed in the dark to prevent bleaching of the fluorophore. Excised patches were obtained under visual control using a 10x objective. For PCF recordings, large patch pipettes with an initial pipette resistance between 0.6 and 1.5 MΩ (10–30 µm diameter) that gave rise to steady-state current amplitudes of around 1.5–5 nA at maximal opening probability of the channel were used. After excision of a membrane patch, the objective was changed to a 60x oil-immersion objective (Olympus Apo N 60XOTIRF) to observe fluorescence. TAMRA was excited with a Spectra X light source (Lumencor, Beaverton, OR) at 550/15 nm, filtered with 543/22 nm, and the fluorescence emission was

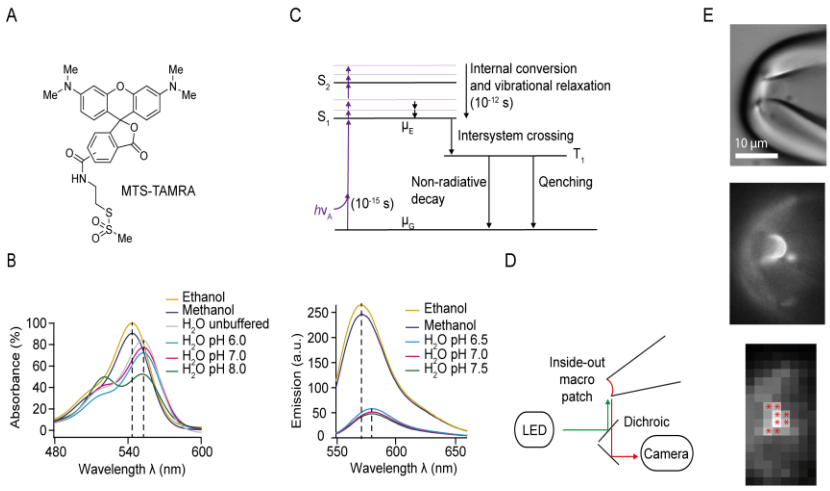

Figure 2.4. MTS-TAMRA is an environmentally-sensitive fluorophore but not sensitive to pH. *A,* chemical structure of MTS-TAMRA. *B*, *left,* absorbance of MTS-TAMRA (50 µM) in ethanol, methanol, and aqueous solutions without buffer and buffered to various pH values. Vertical dashed lines indicate the wavelength of the absorbance peaks. *Right,* emission spectrum of MTS-TAMRA (50 nM) in ethanol, methanol, and aqueous solutions buffered to various pH values. Excitation wavelength was 542 nm. Vertical dashed lines indicate the wavelength of the emissions peaks. *C,* Jablonski diagram for fluorescence of a fluorophore in the presence of a collisional quencher (T for triplett, μ_E for excited state, μ_G for ground state, S only here for singlet), adapted from (Lakowicz, 2006). *D*, scheme of the PCF recording condition. *E*, excised inside-out patch containing ciHv1-L245C-TAMRA (*top*, bright-field image; *middle*, epifluorescent image; *bottom*, 8x8-binned epifluorescent image). Red stars mark pixels included in analysis.

monitored through a TRITC filter cube (Semrock, Rochester, NY, USA; dichroic: 562LP, emission: 593/40) and detected with an iXon Ultra DU-897U emCCD camera (iXon Ultra, Andor Technologies, Belfast, UK) (Fig. 2.4D). The membrane patch was visible as a curved fluorescent stripe (Fig. 2.4E, *middle*). The frame rate was 200 Hz, 8x8 pixels were binned (Fig. 2.4E, *bottom*) and registered in the frame transfer mode using the camera's conventional output amplifier. Acquisition was triggered externally via the ClampEx software. The light intensities, measured with a PS19Q sensor connected to a FieldMax-TOP power meter for visible light (Coherent, Dieburg, Germany) at the level of the recording stage, were ~ 0.16 mW/mm^2. From the brightest pixels (around 5–30 binned pixels, marked with stars in Fig. 2.4E, *bottom*), the mean (i.e. spatial average) fluorescence was calculated and the dark count of the camera was subtracted to obtain the fluorescence F. F was then normalized to the initial baseline level at –80 mV to obtain $\Delta F/F$. The fluorescence ($\Delta F/F$) is the spatial average of the pixel intensities of the marked pixels as exemplified in Fig. 2.4E. For the average fluorescence traces in different pH conditions or in presence or absence of MTS-1-MTS (Fig. 3.7E-H; 3.11B; 3.12B; 3.13B; 3.17C,F; 3.19B; 3.20B), only traces in steady-state conditions (i.e. when solution exchange was completed) were used. The voltage-induced change in fluorescence is denoted as F_{signal}, and the amplitude of F_{Signal} is reported as the difference between the fluorescence at – 80 mV or –60 mV, F(–80 mV) or F(–60mV), respectively, and the steady-state fluorescence at the end of the voltage step.

2.4. Proton uncaging

Photoactivatable proton precursors ("caged protons") allow for control of spatial and temporal pH distribution without diffusional mixing delays. Light is used to trigger structural changes in photosensitive cages ("uncaging", Fig. 2.5A), resulting in a rapid release of protons. Here, two different cages, the salt of sodium (6,7-dimethoxycoumarin-4yl)methyl sulfate (DMCM-caged-proton) (Geißler *et al.*, 2005) (Fig. 3.16G) and 1-(2-nitrophenyl)ethyl sulfate (NPE-caged-proton) (Barth & Corrie, 2002) (Fig. 2.5A), are used in patch-clamp and PCF experiments with ciHv1 and ciHv1-L245C-TAMRA channels. To acidify on one side of the membrane, recording solution with low buffer concentration (0.1 mM HEPES, Table 9) containing caged protons is present at the side

of the proton release, while high-buffered recording solution (Table 8) without caged protons is present at the other side. If all caged protons in the pipette were uncaged by a single light stimulus, the concentration after the light stimulus can be calculated by using the Henderson-Hasselbalch-equation:

$$pH = pK_a + log \frac{[A-]}{[HA]}$$

with the acid dissociation constant pK_a (for HEPES: 7.5), and the concentrations of deprotonated and protonated buffer, [A-] and [HA], respectively. In a recording solution with pH 7.5, buffered by 0.1 mM HEPES (and thus [A-] = 50 µM, [HA] =50 µM), uncaging of 40 µM caged compound changes the pH to

$$pH = 7.5 + log \frac{10\ \mu M}{90\ \mu M} = 6.54\,,$$

which means that the pH of the pipette solution is decreased by roughly 1 pH unit. As the Nernst potential for protons (E_H) is calculated by

$$E_H = 58.2\ mV\ log \frac{[H^+]_o}{[H^+]_i},$$

extracellular acidification of 1 unit pH shifts E_H from 0 mV (prior to uncaging at symmetric pH) to +58.2 mV, or in case of intracellular acidification of 1 unit pH to -58.2 mV after uncaging (at 20°C).

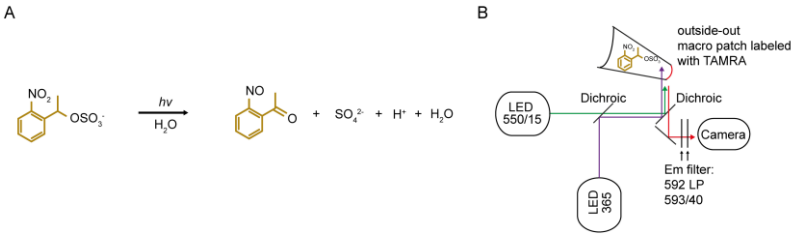

Figure 2.5. Uncaging of protons by light, combined with PCF. *A*, chemical structure and photolytic proton release (uncaging) of NPE-caged-proton. *B,* Scheme of outside-out PCF recording condition with NPE-caged-protons in the pipette. TAMRA was excited with a Spectra X light source at 550/15 nm. NPE-caged-protons were excited with a mounted LED at 365 nm. 365 nm light (purple) was applied via two dichroic 562 LP filter (Dichroic) fluorescence emission was monitored through filter cube containing a dichroic: 562LP and two emission filters (EM filters) and detected with an iXon Ultra DU-897U emCCD camera.

Excised patches were obtained under visual control using a 10x objective. Then, the objective was changed to a 60x oil-immersion objective (Olympus Apo N 60XOTIRF) for proton uncaging. Caged compounds were excited for 1 s with a mounted LED (Thorlabs, Newton, New Jersey, United States). 365 nm

light was applied via two dichroic 562 LP filter (Fig. 2.5B). The light intensities, measured with a PS19Q sensor connected to a FieldMax-TOP power meter for visible light (Coherent, Dieburg, Germany) at the level of the recording stage, were ~ 0.86 mW/mm^2. PCF experiments with ciHv1-L245C-TAMRA were performed in the outside-out configuration with 500 µM NPE-caged-proton in the pipette. MTS-TAMRA was excited by Spectra X light source (see 2.3.3 Patch-clamp fluorometry) unfiltered at 550/15 nm (see Fig. 2.5B). The light stimulus was triggered by the pClamp software.

2.5. Crosslinking

Crosslinking of two segments on the intracellular side of ciHv1 was established as tool to reveal structural rearrangements, distance, and interactions of transmembrane segments in the intracellular gate of ciHv1. For crosslinking, a pair of cysteines on two different helices was introduced (see 2.1.1) either as substrate for hydrogen peroxide (H_2O_2), or binding site for MTS-1-MTS. Cysteine-substitution sites for crosslinking S1 and S4 fulfill certain criteria: The sites are located on the intracellular side of the channel and are solvent exposed as assessed earlier by SCAM analysis (Gonzalez *et al.*, 2010; Mony *et al.*, 2015). Excised inside-out patch configuration allowed for wash in of different reagents to the intracellular gate. Patch-clamp experiments were performed with high-buffered recording solution at pH 6.0 (Table 8) extra- and intracellularly. PCF experiments were performed with high-buffered recording solution at pH 7.0 (Table 8) extra- and intracellularly.

To catalyze the formation of a disulfide bridge between the thiol-reactive groups of two cysteines in close proximity (≈ 2 Å), the oxidizing agent H_2O_2 (40 mM) was added to the pH 6.0 recording solution (Table 8) and washed into the recording chamber. The patch was incubated for at least 5 minutes. To discriminate a potential crosslink from an unspecific rundown of the current amplitude, the reducing agent Tris(2-carboxyethyl)phosphin (TCEP) (500 µM or 800 µM) was washed into the recording chamber to break the putative disulfide bridge. TCEP was directly dissolved in the pH 6.0 recording solution (Table 8), followed by readjustment of the pH by TEAOH.

The homobifunctional crosslinker 1,1-methanediyl bismethanethiosulfonate (MTS-1-MTS, Fig.3.3A) has two thiol-reactive groups allowing to bind covalently to the thiol groups of two cysteines. Therefore, one MTS-1-MTS molecule can crosslink two cysteines up to 3–4 Å apart from each other (Zhang *et al.*, 2002; Zhou *et al.*, 2011). To discriminate a crosslink from independent binding of two MTS-1-MTS molecules to the cysteines, the change in current amplitude due to MTS-1-MTS in the double cysteine mutant was compared to the changes in both single cysteine mutants. In case of independent binding, the change in the double mutant would corresponding to the sum of the changes in the two single mutants. In case of a crosslink, however, the effect should deviate from the sum of the changes in the single mutants, as a crosslink might add additional or different disturbances, e.g. block of gating motions in addition to block of proton permeation. A crosslink was considered to be present, if the residual current in the cysteine-double mutant C_1C_2 was significantly smaller than the calculated residual current for the double mutant, defined as the sum of the block effects of MTS-1-MTS in both single mutants C_1 and C_2:

$$\frac{Ipost(C1C2)}{Ipre(C1C2)} < 1 - \left(\frac{Ipost(C1)}{Ipre\ (C1)} + \frac{Ipost(C2)}{Ipre\ (C2)}\right)$$

MTS-1-MTS was dissolved in DMSO (stock solution 50 mM). MTS-1-MTS was added to the pH 6.0 recording solution (Table 8) for patch-clamp experiments, diluting it 1:1000 (working concentration 50 µM). MTS-1-MTS was added to pH 7.0 recording solution (Table 8) for PCF experiments (working concentration 200 µM). MTS-1-MTS was washed into the recording chamber via gravity-driven perfusion.

2.6. Data analysis and statistics

Conductance-voltage relationship (GV) were obtained from normalized tail currents (I_{tail}) measured 5–25 ms after the end of the depolarizing voltage step and fitted with the Boltzmann equation:

$$G/G_{max} = \frac{1}{\left(1 + e^{\left(\frac{-(V - V_{0.5})}{s}\right)}\right)},$$

where G_{max} is the maximal conductance, s the slope, V the membrane voltage, and $V_{0.5}$ the voltage at which 50% of the maximal current is reached.

CiHv1 WT and mutant activation time constants of current (I) and fluorescence (F) were obtained from double-exponential fits, and the deactivation time constants of F were obtained from mono-exponential fits. The minimum of F was taken as starting point for the deactivation. The relationship between voltage dependence or kinetics and pH or ΔpH was tested with linear regression analysis and tested for significant deviations from a zero-slope line with a significance level of α= 0.05. For ciHv1-I175C-TAMRA, the ΔpH dependence of fast and slow activation time constants of F was compared to the respective slopes of fast and slow activation time constants of I by two-tailed paired t tests with a significance level of α = 0.05. r^2 denotes the coefficient of determination. The ΔpH-induced effects on the F_{signal} amplitude and F(-80mV) in ciHv1 WT and mutants were tested for significance with repeated measures ANOVA, followed by Tukey´s test *post-hoc* analysis.

The ΔpH-induced effects on F_{signal} amplitude and F(-80mV) in ciVSP-G214C-TAMRA were tested with repeated measures ANOVA followed by Bonferroni-corrected *post-hoc* analysis. CiVSP-G214C-TAMRA activation time constants of F_{signal} were obtained from double-exponential fits. The relationship between kinetics and ΔpH was tested with linear regression analysis and tested for significant deviations from a zero-slope line with a significance level of α = 0.05.
The H_2O_2-induced effect on current amplitude in mutant channels was tested for significance with one-way ANOVA, followed by Tukey´s test *post-hoc* analysis for individual comparison of each mutant to WT. A total of 10 mutants were analyzed. TCEP-induced effect on current amplitude within the same patch was tested comparing amplitudes after wash out with current amplitudes after TCEP incubation using the two-tailed paired t test.

The MTS-1-MTS-induced effect on current amplitude in single and double mutant channels was tested for significance with one-way ANOVA, followed by Tukey´s test *post-hoc* analysis for individual comparison of each mutant to WT. A total of 17 mutants were analyzed. MTS-1-MTS-induced effect on current amplitude in double mutants was compared to the respective calculated (theoretical) current amplitude for the same double mutant by two-tailed Student´s t-test. The MTS-1-MTS-induced effects on current, F_{signal}, and F(–80 mV) in TAMRA-

labeled mutant channels were each tested for significance with one-way ANOVAs, followed by Tukey´s test *post-hoc* analysis for individual comparison of each mutant to ciHv1-I175C-TAMRA. A difference was considered as statistically significant with $p < 0.05$. All values are reported as mean ± SD.

2.6.1. Software

Clampfit 10.7 (Molecular Devices, Union City, CA, USA) was used to analyze the patch-clamp data. Igor Pro (Wavemetrics, Portland, OR, USA) was used to analyze the patch-clamp and fluorometry data, and to perform statistical tests. Andor Solis (Oxford instruments company) and Matlab (MathWorks) were used to analyze fluorometry data. Pymol (Schrödinger LLC, NY, USA) was used to visualize 3D-structures of Hv1 and introduce mutations in the ciHv1-model *in silico*. I-Tasser (https://zhanglab.ccmb.med.umich.edu/I-TASSER/) was used to adapt the X-ray crystal structure of mHv1cc (Takeshita *et al.*, 2014) to ciHv1.

2.7. Chemicals and solutions

2-((5(6)-tetramethyl-rhodamine) carboxylamino) ethyl methanethiosulfonate (TAMRA-MTS) and 1,1-methanediyl bismethanethiosulfonate (MTS-1-MTS) were purchased from Toronto Research Chemicals (North York, ON, Canada). 1-(2-nitrophenyl)ethyl sulfate (NPE-caged-proton) was purchased from Tocris (Bristol, UK). All other Chemicals were purchased from Sigma-Aldrich (St. Louis, MO, USA), Carl Roth (Karlsruhe, Germany), Thermo Fisher (Waltham, MA, USA), or Merck Millipore (Darmstadt, Germany).

Prior to all experiments, the pH of the recording solutions was measured and adjusted if necessary. The solution that was filled into the patch pipette was pre-filtered using syringe filters with 0.2 µm pore size (VWR, Darmstadt, Germany).

Chemical	Concentration (mM)				
	pH 6.0	**pH 6.5**	**pH 7.0**	**pH 7.5**	**pH 8.0**
HEPES	-	-	100	100	-
Tris	-	-	-	-	130
MES	100	100	-	-	-
MS	30	30	30	30	40
TEACl	5	5	5	5	5
EGTA	5	5	5	5	5
Set pH with	TEA-OH	TEA-OH	TEA-OH	TEA-OH	MS

Table 8. High-buffer recording solutions at different pH.

Chemical	Concentration (mM)
HEPES	0.1
NMDG	90
MS	30
TEACl	5
EGTA	5
Caged protons	0.5
TEAOH	Set to pH 7.5

Table 9. Low-buffer pipette solutions with pH = 7.5.

Chemical	Concentration (mM)
KCl	92
$CaCl_2$	0.75
$MgCl_2$	1
HEPES	10
KOH	Set pH to 7.5

Table 10. Labeling solution.

3. Results

3.1. Crosslinking

In Hv1, voltage determines the conformation of the S4 segment (Gonzalez *et al.*, 2010), which controls channel activation. Subsequent opening of the pore occurs concomitantly with a conformational change of the S1 segment (Mony *et al.*, 2015) (Fig. 1.3B). The coupling of S4 and S1, i.e. voltage-sensing with pore opening, is not well understood. An electrostatic interaction between the selectivity-filter residues in S4 and S1 in the open state of the channel was suggested (Berger & Isacoff, 2011; Mony *et al.*, 2015). High-resolution structures of Hv1 in the closed and open state are lacking, which limits our understanding of state-dependent changes of distance or interaction between amino-acid residues. Information about the structure of ion channels can be also obtained by cysteine-based crosslinking (Larsson & Elinder, 2000; DeCaen *et al.*, 2008). Here, I used this technique in several experiments combined with PCF, to measure distances, distance changes, and coupling of S4 and S1 segments.

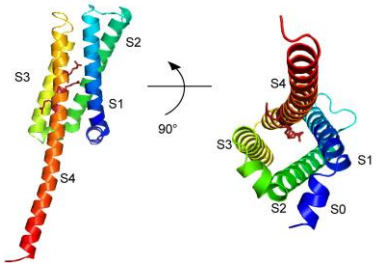

Figure 3.1. Homology model of ciHv1. *Left,* side view (viewed parallel to the membrane) of the ciHv1 transmembrane segments, depicted as follows: S1 in blue, S2 in green, S3 in yellow and S4 in orange, C-terminus in red. The three arginine residues (R255, R258 and R261) in S4 are shown as stick models. *Right,* the same subunit viewed from a different angle, rotated 90° along the horizontal axis, showing the intracellular gate and the N-terminal cytoplasmic helix (S0). The homology model is based on the X-ray crystal structure of mHv1cc (Takeshita *et al.*, 2014) and adapted to ciHv1.

3.1.1. Crosslinking S1 and S4

To measure distances and amino-acid interactions between helices S1 and S4 (Fig 3.1), I screened for cysteine-double mutants that can be crosslinked. Guided by previous studies (Mony et al., 2015, Gonzalez et al., 2010), I introduced cysteines at intracellular, solvent-accessible sites of segments S1 and S4 of ciHv1 (Fig. 3.2D). Ten S1-S4 cysteine-double mutants were heterologously expressed in *X. laevis* frog oocytes. Recordings were performed in the excised inside-out patch-clamp configuration, allowing for direct superfusion of the intracellular side with a crosslinking reagent. I tested several crosslinking reagents.

Crosslinking with hydrogen peroxide

I used hydrogen peroxide (H_2O_2), because H_2O_2 oxidizes thiol groups of cysteines and, thereby, catalyzes disulfide-bridge formation between nearby residues (length of disulfide bridge ≈ 2 Å). I expected that crosslinking S1 and S4 interferes with conformational changes of S1 and S4 during the gating process, which might result in a blocked channel, a locked open channel, or in altered activation or deactivation kinetics. Recordings from ciHv1 WT and from the cysteine-double mutant ciHv1-I153C-I262C are shown in Fig. 3.2. Proton currents were recorded in response to repetitive voltage steps from –80 mV to 80 mV (Fig. 3.2B,F). WT current amplitude changed only weakly after incubation for minutes in H_2O_2 (Fig. 3.2B,C), suggesting that H_2O_2 either does not oxidize endogenous cysteines (C6, C26, C315) or that H_2O_2-induced oxidation of endogenous cysteines does not change gating. By contrast, the current amplitude of CiHv1-I153C-I262C decreased by almost 40% during the first 6 min of incubation with H_2O_2 (Fig. 3.2F), however without reaching a steady-state level after 6 min (Fig. 3.2G). If the decrease of current amplitude results from an H_2O_2-dependent crosslink, wash out of H_2O_2 and wash in of the reductant TCEP, which breaks disulfide bridges between cysteines, should stop or attenuate the decrease of current amplitude. However, neither wash out of H_2O_2 nor incubation in TCEP did change the decrease of current amplitude (Fig. 3.2G), suggesting that the decrease of current amplitude was unspecific and no crosslink was formed between the introduced cysteines. In all but one cysteine-double mutant (ciHv1-I154C-N264C), a decrease in current amplitude after ≥ 5 min incubation in

H_2O_2 was observed (Fig. 3.2I; Appendix Table 11), suggesting a general sensitivity to oxidation in the mutants compared to the WT. In mutant ciHv1-I154C-I262C, the decrease of current amplitude was significant compared to WT (one-way ANOVA, p = 0.003; *post-hoc* analysis, p = 0.002). However, because TCEP did not have a clear effect in any of the mutants (Fig. 3.2I) (paired t-test for "wash out" vs. "TCEP", p > 0.05), I conclude that the pairs of introduced cysteines are not crosslinked. This shows that the application of H_2O_2 and TCEP to screen for nearby residues on S1 and S4 does not work under my experimental conditions.

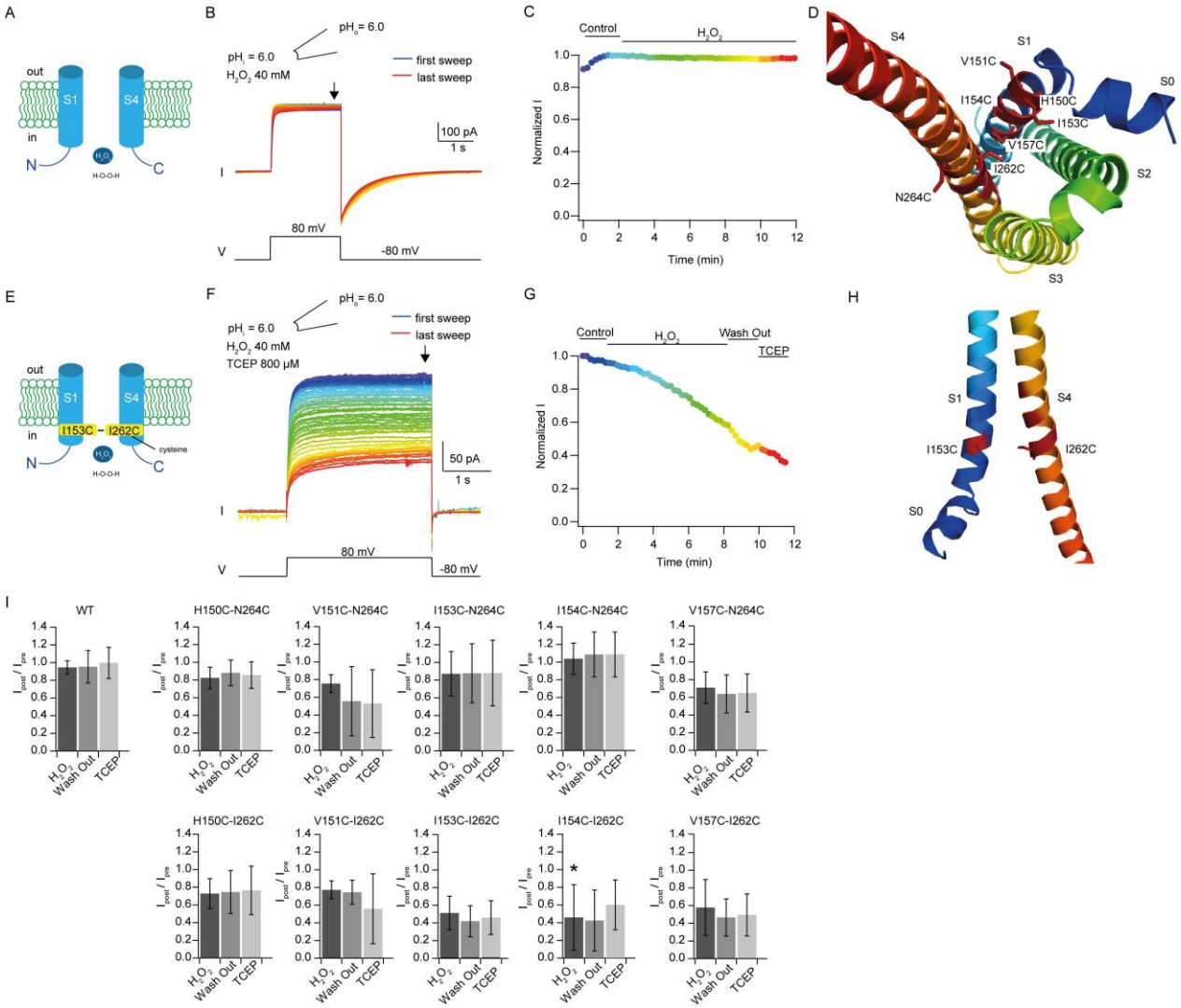

Figure 3.2. H_2O_2 blocks certain cysteine-double mutants after minutes of incubation and block effect is contaminated by rundown. *A,* cartoon of ciHv1-WT with H_2O_2 near the intracellular gate. For clarity, only S1 and S4 are shown. B, representative inside-out patch-clamp recording of ciHv1-WT in response to repetitive voltage steps from –80 mV to +80 mV and back. During the recording, H_2O_2 (40 mM) was washed to the intracellular side, keeping $pH_i = pH_o = 6.0$. C, normalized current amplitude of each iteration in B (time point indicated by arrow) as function of time. *D,* homology

model of a protomer of ciHv1 showing the intracellular gate. Engineered cysteine residues on S1 and S4 used for the screen are shown in red sticks. *E,* cartoon of the target site of H_2O_2 in the cysteine-double mutant ciHv1-V153C-I262C. For clarity, only S1 and S4 are shown. *F,* representative inside-out patch-clamp recording of ciHv1-I153C-I262C in response to repetitive voltage steps from –80 mV to +80 mV and back. During the recording, H_2O_2 (40 mM) and afterwards TCEP (800 µM) was washed to the intracellular side, keeping pH_i = pH_o = 6.0. *G,* normalized current amplitude of each iteration in C (time point indicated by arrow) as function of time. *H*, homology model of ciHv1-I153C-I262C. The engineered cysteine residues on S1 and S4 are shown in red sticks. For clarity, only S1 and S4 are shown *I,* current amplitude of ciHv1-WT and all double-cysteine mutants after wash in of H_2O_2, wash out of H_2O_2 (see Appendix Table 11 for means and n), and wash in of TCEP, in relation of the current before wash in of H_2O_2. * indicates significant difference between mutant and WT channel ($p < 0.05$). Error bars indicate SD.

3.1.2. MTS-1-MTS crosslinks S1 and S4

I next tested whether MTS-1-MTS (Fig. 3.3A), a membrane-permeable (Fig. 3.8), homo-bifunctional sulfhydryl reagent can crosslink the cysteines introduced in S1 and S4. WT current amplitude only slightly changed in response to MTS-1-MTS (Fig.3.3B,C; Fig. 3.5A), suggesting that MTS-1-MTS by itself or by interaction with endogenous cysteines in ciHv1 (C6, C26, C315) does not change gating. By contrast, the current amplitude of ciHv1-V151C-I262C decreased by more than 90% within 1 minute during incubation with MTS-1-MTS (Fig. 3.3E,F). Wash out of MTS-1-MTS did not change the current amplitude (Fig. 3.3F), suggesting that MTS-1-MTS bound covalently to at least one of the two cysteines which in turn resulted in channel blocking.

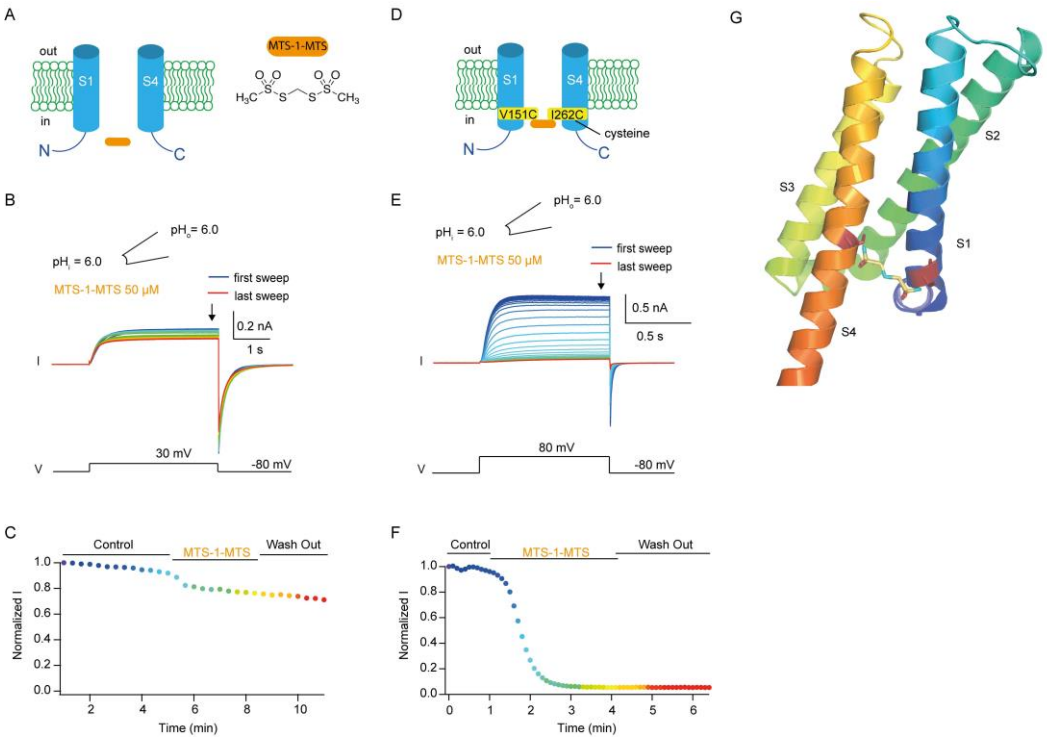

Figure 3.3. MTS-1-MTS wash in results in rapid and almost complete block of ciHv1-V151C-I262C. *A,* cartoon of ciHv1-WT with MTS-1-MTS in orange (*left*) and chemical structure of MTS-1-MTS (*right*). For clarity, only S1 and S4 are shown. *B*, inside-out patch-clamp experiments of ciHv1-WT in response to repetitive voltage steps from –80 mV to 30 mV. MTS-1-MTS (50 µM) was washed to the intracellular side, keeping $pH_i = pH_o = 6.0$. *C*, normalized current amplitude of each iteration in B (time point indicated by arrow) as function of time. *D*, cartoon of the cysteine-double mutant ciHv1-V151C-I262C and MTS-1-MTS in orange. For clarity, only S1 and S4 are shown. *E,* inside-out patch-clamp experiments of ciHv1-V151C-I262C in response to repetitive voltage steps from –80 mV to 80 mV. MTS-1-MTS (50 µM) was washed to the intracellular side, keeping $pH_i = pH_o = 6.0$. *F,* normalized current amplitude of each iteration in E (time point indicated by arrow) as function of time. *G,* side view (viewed parallel to the membrane) of the homology model for ciHv1-V151C-I262C and MTS-1-MTS. The introduced cysteines are red.

Noteworthy, in 8 out of 10 double-mutants MTS-1-MTS blocked the channel without decreasing the current amplitude during depolarization. Therefore, successive channel block must have occurred during hyperpolarization while channels were closed (see Fig. 3.3E for example with ciHv1-V151C-I262C). Exceptions to this observation are the I153C mutants, which show current changes also during depolarization, indicating that in these mutants, MTS-1-MTS can also block the open state (Fig. 3.4).

In all 10 cysteine-double mutants MTS-1-MTS decreased the current amplitude significantly compared to WT (Fig. 3.5, Appendix Table 12) (one way ANOVA, $p < 0.0001$; p*ost-hoc*

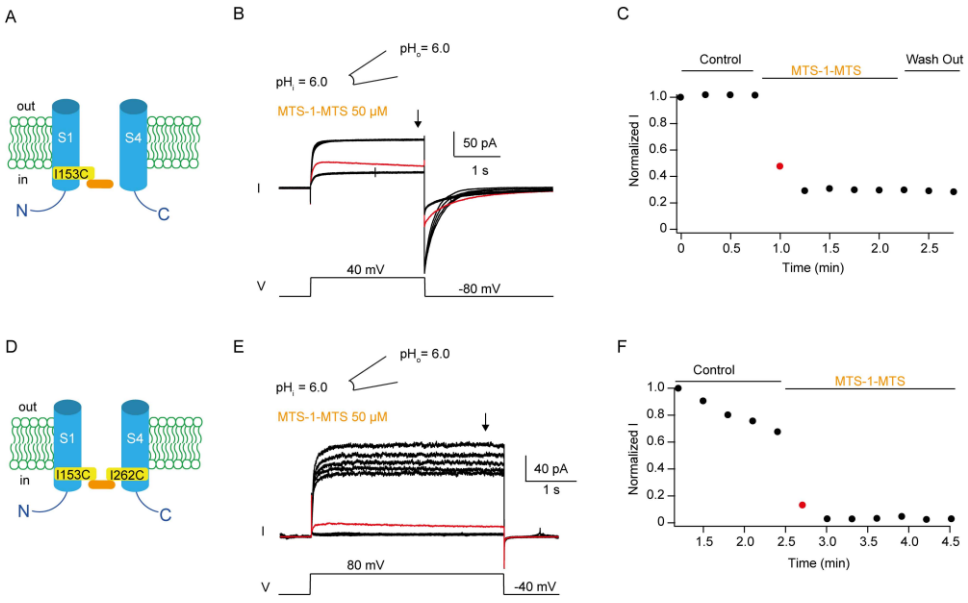

Figure 3.4. CiHv1-I153C and ciHv1-I153C-I262C are blocked by MTS-1-MTS also in the open state. *A,* cartoon of ciHv1-I153C with MTS-1-MTS. For clarity, only S1 and S4 are shown. *B*, inside-out patch-clamp experiments of ciHv1-I153C in response to repetitive voltage steps from –80 mV to 40 mV. MTS-1-MTS (50 µM) was washed to the intracellular side, keeping $pH_i = pH_o = 6.0$. *C*, normalized current amplitude of each iteration in B (time point indicated by arrow) as function of time. The red data point corresponds to current amplitude of red labeled current trace in B. *D*, cartoon of ciHv1-I153C-I262C with MTS-1-MTS. For clarity, only S1 and S4 are shown. *E,* inside-out patch-clamp experiments of ciHv1-I153C-I262C in response to repetitive voltage steps from –40 mV to 80 mV. MTS-1-MTS (50 µM) was washed to the intracellular side, keeping $pH_i = pH_o = 6.0$. *F,* normalized current amplitude of each iteration in E (time point indicated by arrow) as function of time. The red data point corresponds to current amplitude of red labeled current trace in E.

analysis, $p < 0.0001$ for WT vs. all cysteine-double mutants). However, in some single-cysteine mutants MTS-1-MTS also decreased the current amplitude significantly (*post-hoc* analysis, $p < 0.0001$ for WT vs. H150C, I153C, I262C, N264C) (Fig. 3.5, Appendix Table 12), although in these mutants a crosslink cannot occur. Crosslinking of the introduced cysteine with an endogenous cysteine is unlikely to occur, because endogenous cysteines are located in the N- and C-terminal region, distant from S1 and S4. This shows that MTS-1-MTS binding to a single cysteine is sufficient to decrease the current amplitude. Thus, a current decrease in double mutants does not necessarily result from a crosslink. Instead, the effect might result from binding of one MTS-1-MTS molecule to a single cysteine, or from binding of two MTS-1-MTS molecules, each binding to one of the two cysteines independently. If there is no crosslink but instead independent binding to both cysteines in the double mutant, the

block effect in the double mutant should then equal the sum of the block effects in the respective single mutants. Whereas if there is a crosslink in a double mutant, the block effect could deviate from the sum of the block effects in the respective single mutants. Therefore, to identify crosslinks, I calculated the residual current for every double mutant based on the sum of the effects measured in the single mutants (for calculation see Methods 2.5). I assumed that a crosslink took place when the actual measured residual current in the double mutant was significantly smaller than the calculated residual current amplitude. Fig. 3.5 shows mean current amplitude ratios after and before MTS-1-MTS wash in (I_{post}/I_{pre}) of the double mutants, single mutants, and the calculated (theoretical) I_{post}/I_{pre} (red lines). Only in the double mutant V151C-I262C the actual measured current amplitude I_{post}/I_{pre} = 0.07 ± 0.04 (n = 9) was significantly (two-tailed Student's t-test, p = 0.00002) smaller than the calculated theoretical ratio I_{post}/I_{pre} = 0.185 (Fig 3.5D and Appendix Table 12), suggesting MTS-1-MTS crosslinked residues 151 and 262.

To corroborate the finding that the channel block in V151C-I262C results from a crosslink rather than steric changes due to cysteine substitutions, I performed the same experiment with a double mutant of similar steric changes, ciHv1-V151S-I262C, that cannot be crosslinked. Lacking the cysteine on S1, a crosslink by MTS-1-MTS is not possible; however, the steric change by substitution with an isosteric serine (V151S) is assumed to be similar to a cysteine substitution. The current ratio I_{post}/I_{pre} = 0.43 ± 0.14, n = 10 in mutant V151S-I262C (Fig. 3.5D and Appendix Table 12) was six-fold higher than the current ratio in the mutant V151C-I262C and this difference was statistically significant (two-tailed Student's t-test, p = 0.00001), suggesting that the MTS- 1- MTS block in the double mutant V151C-I262C depends on the presence of both cysteines and that MTS-1-MTS crosslinks those cysteines. It is assumed that MTS-1-MTS can bridge a distance of 3-4 Å between the sulfur atoms of two crosslinked cysteines (Zhang *et al.*, 2002; Zhou *et al.*, 2011). This estimate was extrapolated from the length of other longer spacers (Green *et al.*, 2001; Loo & Clarke, 2001). Therefore, the distance between the two S1 and S4 residues is about 3-4 Å at some point during gating.

Hv1 forms dimers (Koch *et al.*, 2008; Lee *et al.*, 2008; Tombola *et al.*, 2008). Parts of S1 (Lee *et al.*, 2008; Mony *et al.*, 2020) and S4 (Fujiwara *et al.*, 2014) are involved in the dimer interface, but not the C-terminus (Tombola *et al.*, 2008; Lee *et al.*, 2008; Koch *et al.*, 2008; Fujiwara *et al.*, 2012). Therefore, the crosslink might form between residues V151C and I262C of

different subunits. However, neither V151 (Mony *et al.*, 2020) nor I262 (Lee *et al.*, 2008; Fujiwara *et al.*, 2014) are functionally involved in dimer interfaces of S1 and S4, respectively. In addition, I262 was located outside the dimer interface of S4 (Takeshita *et al.*, 2014; Bayrhuber *et al.*, 2019). Therefore, it is likely that MTS-1-MTS crosslinks V151C and I262C in the same subunit.

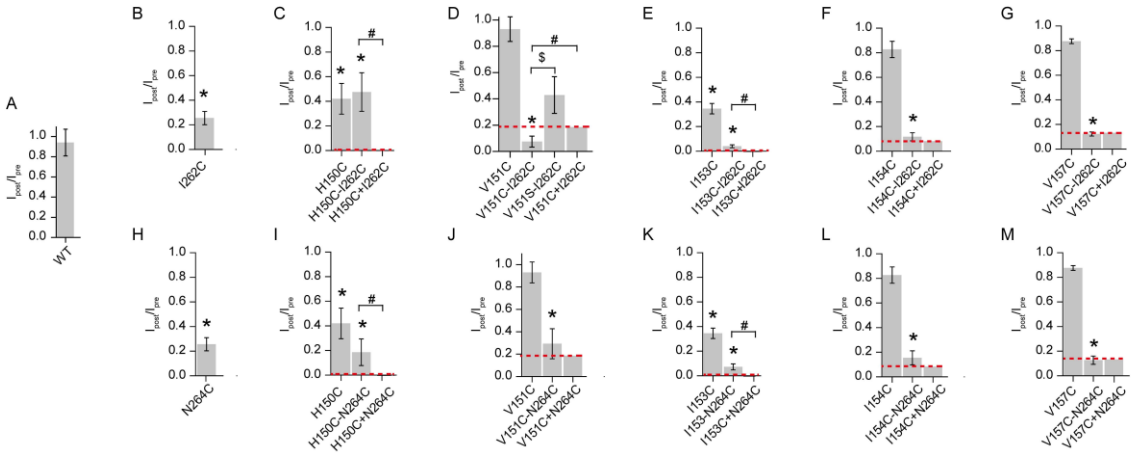

Figure 3.5. Block effect of MTS-1-MTS is higher than calculated in ciHv1-V151C-I262C *A-M,* mean current ratio after and before MTS-1-MTS wash in (I_{post}/I_{pre}) of ciHv1 WT (A) or single and double mutants and the respective calculated (theoretical) I_{post}/I_{pre} (red line; see Methods 2.5). * indicates a statistically significant difference ($p < 0.05$) between mutant and WT channel; # indicates a statistically significant difference ($p < 0.05$) between double mutant and the corresponding calculated (theoretical) value. $ indicates a statistically significant difference between V151C-I262C and V151S-I262C ($p = 0.00001$). See Appendix Table 12 for means, n, exact p-values, and distances between the two engineered cysteines in each double mutant. Error bars indicate SD.

3.1.3. Crosslinking S1 and S4 interferes with S1-gating motion

Because the VSD of Hv1 encompasses also the pore, the MTS-1-MTS-dependent crosslink between residues on S1 and S4 might block proton conduction without disturbing gating motions. To clarify if and how the crosslink changes gating in Hv1, I studied gating motions. A previous study showed that S1 moves upon depolarization (Mony *et al.*, 2015). Using the patch-clamp fluorometry (PCF) technique (Zheng & Zagotta, 2003; Berger & Isacoff, 2015; Mony *et al.*, 2015), I investigated whether crosslinking residues on S1 and S4 can change the S1 gating motion. As readout for gating motions, I used the environmental-sensitive thiol-reactive fluorophore MTS-TAMRA (Fig. 2.4A). For MTS-TAMRA labeling, a single cysteine was introduced at position I175C, which is located at the extracellular end of S1 (Takeshita *et al.*, 2014) (Fig. 3.6A). Here, I probed S1 conformational changes by stepping from – 80 to +40 mV such that the Hv1 channel preferentially populates the open state. Using a camera, changes in fluorescence was recorded from voltage-clamped, excised inside-out macro-patches (Fig. 2.4D,E). Upon a voltage step from a holding potential of –80 to +40 mV, the fluorescence of ciHv1-I175C-TAMRA increased together with the current amplitude. The change was reversible: upon stepping back to –80 mV, the fluorescence intensity returned to its original value together with tail currents (Fig. 3.6B). The voltage-evoked fluorescence change (F_{Signal}) is consistent with a previous study (Mony *et al.*, 2015) and was interpreted as the S1 motion during pore opening (Fig. 3.6A). To obtain a readout for S1 gating motions, I introduced the labelling site I175C in the V151C-I262C background and labeled with

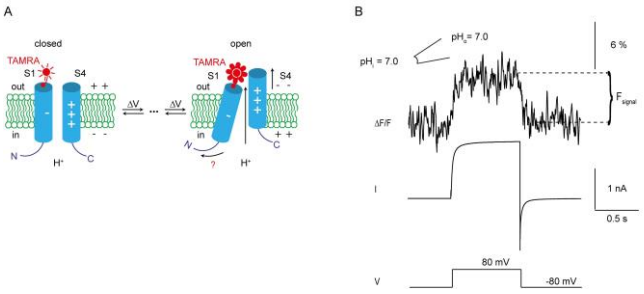

Figure 3.6. Voltage-evoked S1 conformational changes can be observed in the TAMRA fluorescence. *A*, cartoon depicting voltage-evoked S1 conformational change of ciHv1-I175C-TAMRA. For clarity, only S1 and S4 are shown. "-" sign denotes a conserved aspartate on S1, "+" signs denote the charged arginines in S4. Depolarization induces structural changes that open the channel. Arrows indicate voltage-driven transitions through different functional states. *B*, representative mean fluorescence and current signal of an inside-out PCF recording of ciHv1-I175C-TAMRA, in response to voltage steps from –80 to +80 mV.

MTS-TAMRA. Similar to ciHv1-175C-TAMRA, the fluorescence recorded from ciHv1-V151C-I262C-I175C-TAMRA (denoted V151C-I262C-I175C* in the following) increased in response to a voltage step from –80 mV to +80 mV (Fig. 3.7D,H black); stepping back to –80 mV, the fluorescence showed a monotonic decrease back to baseline (Fig. 3.7D,H black). The F_{signal} and currents indicate that the two cysteines at the intracellular side do not affect gating. If crosslinking V151C with I262C interferes with gating, it might interfere either with the conformation or gating motion of S1 and/or S4, which in turn changes F_{signal}. Indeed, wash-in of MTS-1-MTS to the intracellular side drastically altered fluorescence in two aspects: first, the baseline fluorescence intensity at –80 mV, F(-80mV), was lowered (F-80 mV (post)/F-80 mV (pre) = 0.82 ± 0.05) (Fig. 3.7D,I *left*, Appendix Table 13), indicating that crosslinking changes the S1 conformation in a non-conducting closed state. Second, the F_{signal} amplitude was decreased by approximately 80% (F_{signal} (post)/F_{signal} (pre) = 0.2 ± 0.1) (Fig. 3.7D,H,I *middle*, Appendix Table 13), indicating that crosslinking interferes with the S1-gating motion. Comparison of the MTS-induced effects in V151C-I262C-I175C* and S1-labeled control mutants V151C-I175C* (Fig. 3.7B,F) and I262C-I175C* (Fig.3.7C,G) to 175C* (Fig. 3.7 A,E) showed that the decrease of F(–80 mV) and the decrease in F_{signal} was most prominent and only significant in V151C-I262C-I175C* channels (for quantification see Fig. 3.7 I *left* and *middle*; for statistical analysis see Appendix Table 13). This indicates that the crosslink between residues 151C and 262C, but not binding of MTS-1-MTS to either 151C or 262C, impedes S1 gating motion and changes resting-state conformation of S1. In addition to fluorescence changes, MTS-1-MTS also decreased the current amplitude in V151C-I262C-I175C* channels significantly compared to I175C* channels (I_{post}/I_{pre} = 0.2 ± 0.1) (Fig. 3.7I *right*, Appendix Table 13), indicating that crosslinking blocks both, conduction and S1 gating motion. A decrease of current amplitude was expected for V151C-I262C-I175C*, as this was observed in V151C-I262C channels before (Fig. 3.3 and 3.5D), however, the block did not amount to the same extent as observed in V151C-I262C channels (I_{post}/I_{pre} = 0.07 ± 0.04; Fig. 3.5D, Appendix Table 12). The difference might result from the additionally introduced labeling side I175C*or different pH conditions in PCF ($pH_o = pH_i$ = 7.0, Fig. 3.7) and patch-clamp experiments ($pH_o = pH_i$ = 6.0, Fig. 3.3 and Fig. 3.5). Importantly, the measured residual current in V151C-I262C-I175C* was significantly smaller (two-tailed Student´s t-test, p = 0.03) than the calculated (theoretical) residual current in V151C-I262C-I175C* channels

(based on block effect of V151C-I175C* and I262C-I175*, calculated I_{post}/I_{pre} = 0.34; Fig. 3.7I *right*, red line), corroborating that MTS-1-MTS crosslinks also V151C-I262C-I175C* channels.

Binding of MTS-1-MTS to S4 in mutant I262C-I175C* did not significantly decrease F_{signal} compared to I175C* (Table 13, p = 0.06) (Fig. 3.7I *middle*). However, similar to observations for single-mutant channel I262C (Fig. 3.5, Appendix Table 12), binding of MTS-1-MTS to S4 decreased significantly the current amplitude in mutant channels I262C-I175C* compared to I175C* (I_{post}/I_{pre} = 0.41 ± 0.14, p = 0.00003) (Fig. 3.7 *right*, Appendix Table 13). A significant decrease of current amplitude but not in F_{signal} suggests that S1 gating motion is not coupled to current flux, which is in line with other results reported elsewhere in this thesis (Fig. 3.13E) and a previous study (Mony *et al.*, 2015).

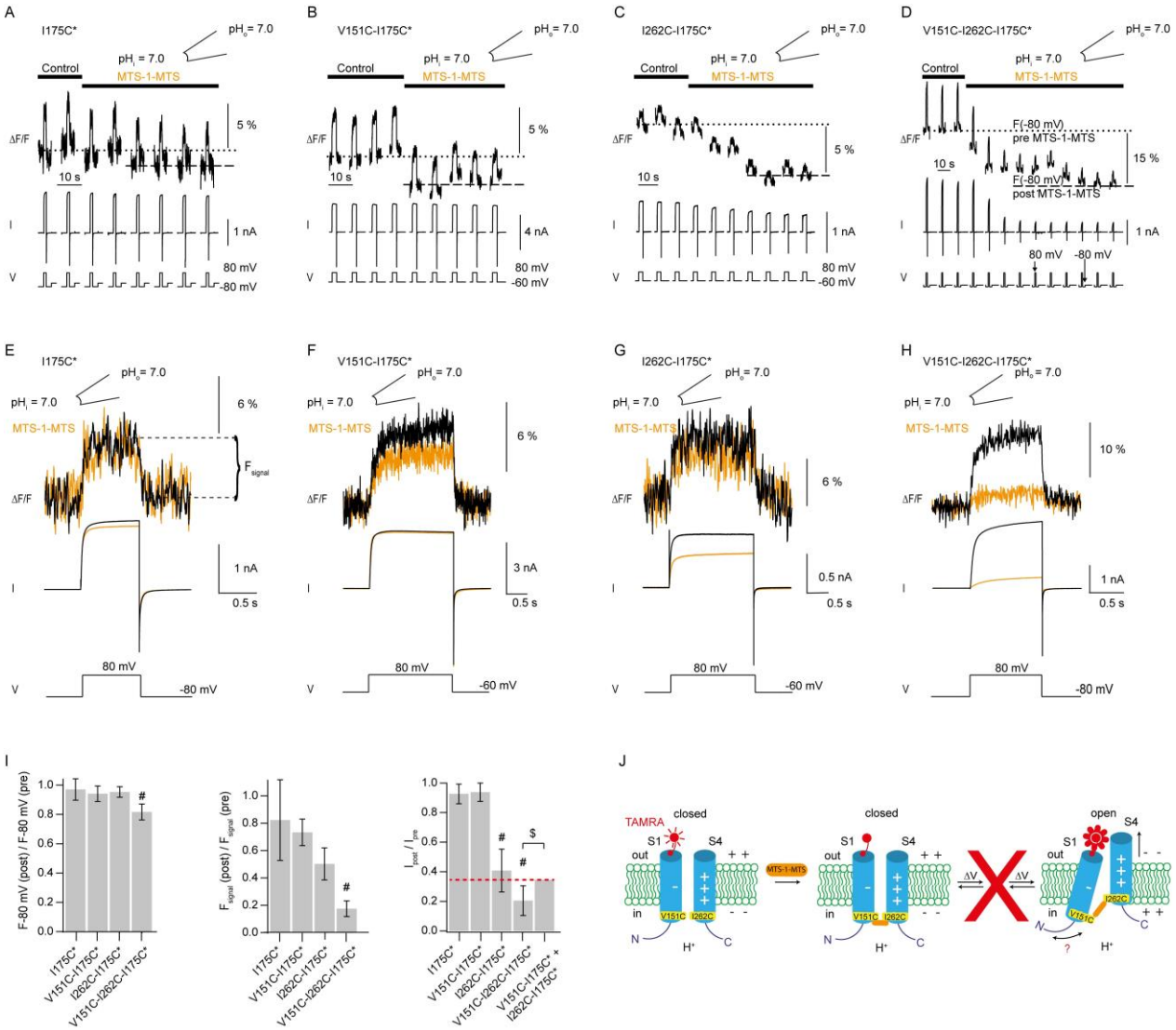

Figure 3.7. MTS-1-MTS block interferes with S1-gating motion. *A-D,* inside-out PCF recordings from patches containing I175C*, V151C-I175C*, I262C-I175C*, or V151C-I262C-I175C* in response to repetitive voltage steps from –60 or –80 mV to 80 mV. MTS-1-MTS (200 µM) was washed to the intracellular side, keeping $pH_i = pH_o = 7.0$. Horizontal lines (dotted, pre MTS-1-MTS; dashed, post MTS-1-MTS) indicate the mean F(-80mV). *E-H*, calculated mean fluorescence signals from A-D before (black) and after (orange) MTS-1-MTS incubation. Fluorescence traces were baseline adjusted. *I,* (*left)* mean F(–80 mV) ratio after and before MTS-1-MTS incubation (F- 80 mV (post) /F-80 mV (pre)). *Middle*, mean F_{signal} ratio after and before MTS-1-MTS incubation (F_{signal} (post) / F_{signal} (pre)). *Right*, mean current ratio after and before MTS-1-MTS incubation (I_{post}/I_{pre}), red line indicates calculated (theoretical) residual current for V151C-I262C-175C* (I_{post}/I_{pre} = 0.34). # indicates a statistically significant difference between mutant and I175C* channel (Appendix Table 13). $ indicates a statistically significant difference (p = 0.03) between V151C-I262C-I175C* and the corresponding calculated (theoretical) value. Error bars indicate SD. *J,* gating scheme of V151C-I262C-I175C*, blocked by MTS-1-MTS. Wash in of MTS-1-MTS changes the conformation in a non-conducting state (*middle*) and blocks structural changes that open the channel.

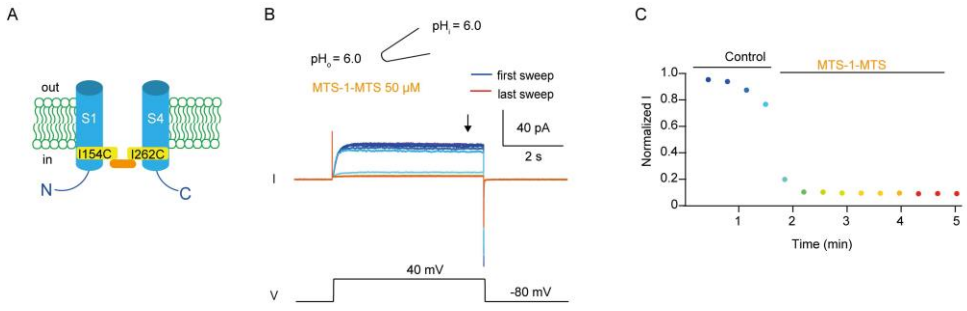

Figure 3.8. MTS-1-MTS extracellularly applied blocks ciHv1-I154C-I262C. *A,* cartoon of ciHv1-I154C-I262C with MTS-1-MTS in orange. For clarity, only S1 and S4 are shown. *B*, outside-out patch-clamp experiments of ciHv1-I154C-I262C in response to repetitive voltage steps from -80 mV to 40 mV. MTS-1-MTS (50 µM) was washed to the extracellular side, keeping $pH_i = pH_o = 6.0$. *C*, normalized current amplitude of each iteration in B (time point indicated by arrow) as function of time.

MTS-1-MTS is membrane permeable (Fig. 3.8) and therefore might interact with the fluorophore or the extracellularly introduced cysteine for labeling (I175C). However, F_{signal} (Fig. 3.7I *middle*, Table 13) and F(–80 mV) (Fig. 3.7I *left*, Table 13) in I175C* channels were only slightly decreased by MTS-1-MTS (F_{signal} (post)/F_{signal} (pre) = 0.8 ± 0.3, (F-80 mV (post)/F-80 mV (pre) = 0.97 ± 0.07), indicating that there was only negligible interaction between MTS-1-MTS and the extracellularly introduced labeling side I175C* or quenching of TAMRA. Thus, MTS-1-MTS is suitable to perform crosslinking during PCF recordings.

To conclude, I established a novel approach to identify structure-function relationships in an ion channel by combining cysteine-based crosslinking with PCF. While Hv1 is crosslinked, both, current changes and changes in (electrophysiological silent) gating motions can be observed at the same time. I identified residues on S1 and S4 that can be crosslinked with MTS-1-MTS. Crosslinking of S1 and S4 results in block of conduction. Furthermore, by labeling S1, I showed that crosslinking changes the S1 conformation, while the channel is in a non-conducting closed state, and impedes S1 gating motion (Fig. 3.7J).

3.2. ΔpH-dependent gating

3.2.1. Voltage dependence of Hv1 is sensitive to ΔpH, but not to pH itself

In Hv1, gating is controlled not only by voltage but also by ΔpH. ΔpH-sensing and its coupling to voltage-sensing is not understood at the molecular level. To study this coupling in ciHv1, I recorded currents from excised inside-out membrane patches under various pH conditions (Fig. 3.9). Depolarizing voltage steps (up to +100 mV) gave rise to outward currents (Fig. 3.9A). From the tail currents (Fig. 3.9A, arrows), the normalized conductance-voltage relationship (GV) was calculated (Fig. 3.9B, see Methods). When pH_i was changed from 7.0 to 6.5 (resulting in ΔpH = 0.5) or from 7.0 to 7.5 (ΔpH = –0.5), the voltage of half-maximal activation ($V_{1/2}$) of the GV relation shifted towards more negative or positive potentials, respectively (Fig. 3.9B). Similar to previous reports (Cherny *et al.*, 1995; Ramsey *et al.*, 2006; Sasaki *et al.*, 2006), the $V_{1/2}$ shifted by –48.6 ± 9.5 mV/ΔpH unit (Fig. 3.9D, E, Appendix Table 14). By contrast, at symmetrical pH (ΔpH = 0), $V_{1/2}$ shifted only by –9.1 ± 4.6 mV/pH unit between pH 6.5 and 7.5 (Fig. 3.9C, F, G), indicating that within this pH range, the voltage dependence of ciHv1, like the voltage dependence of its orthologues from human and mice, is relatively insensitive to pH itself (Fig. 3.9G).

Similar to the ΔpH-dependent changes in kinetics seen in voltage-gated proton currents in rat alveolar epithelial cells (Cherny *et al.*, 1995), I also observed that the kinetics of ciHv1 activation depend on ΔpH: the fast and slow activation time constants τ_{fast} and τ_{slow} become faster when ΔpH becomes more positive, i.e. when $pH_i < pH_o$ (Fig. 3.9H, Appendix Table 15). The relationship between $\log(\tau_{fast})$ and ΔpH, and between $\log(\tau_{slow})$ and ΔpH was linear in the investigated pH range. As previously reported for human Hv1 (Berger *et al.*, 2017), the activation time constants of ciHv1 are faster at acidic symmetric pH than at alkaline symmetric pH (Fig. 3.9I and Appendix Table 15). However, the dependence of channel activation kinetics on ΔpH is steeper than the dependence of channel activation kinetics on symmetric changes in pH itself (compare Fig. 3.9H and I). Taken together, the activation kinetics suggest that channel gating depends more on pH_i than on pH_o.

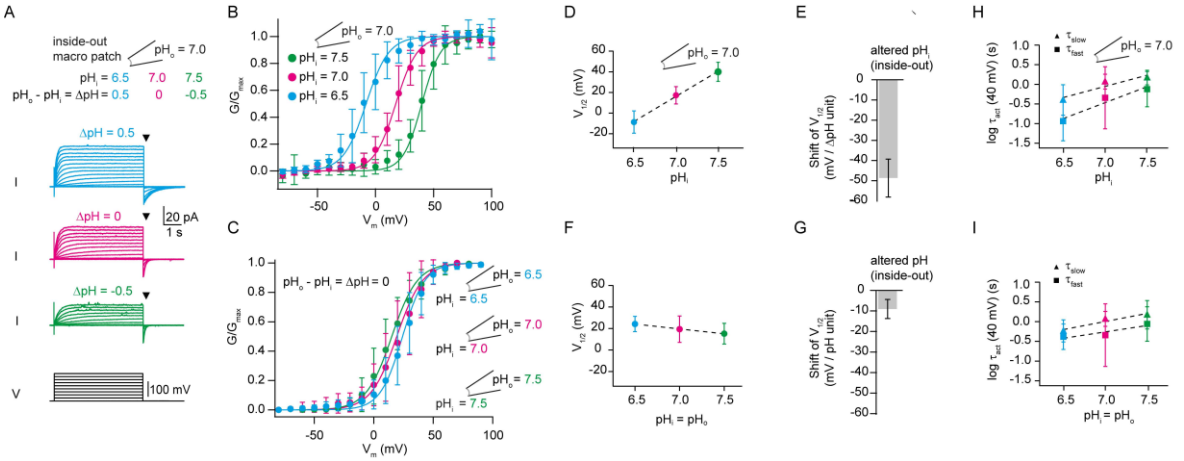

Figure 3.9. Voltage dependence of ciHv1 is coupled to the difference between pH_i and pH_o (ΔpH), but not to pH itself. A, inside-out patch-clamp recordings of ciHv1 at different ΔpH conditions. B, Mean GVs derived from tail currents (at time points specified by triangles in panel A) at different ΔpH conditions. Data from individual patches were fitted with Boltzmann functions (not shown), and the resulting mean slopes and mean $V_{1/2}$ values were used to construct Boltzmann fits for the mean GVs (see Appendix Table 14 for fit parameters). C, GVs derived from tail currents of inside-out patch-clamp recordings of ciHv1 at different pH, leaving ΔpH = 0, fitted with Boltzmann functions. D, $V_{1/2}$ as a function of pH_i while pH_o = 7. The dashed line is a linear fit with a slope of –48.6 mV/ΔpH unit; r^2 = 0.8, $p < 0.05$. E, shift of $V_{1/2}$ per ΔpH unit (altered pH_i, –48.6 ± 9.5 mV). F, $V_{1/2}$ as a function of the pH itself. The dashed line is a linear fit with a slope of –9.1 mV/pH unit; r^2 = 0.1, n.s. G, shift of $V_{1/2}$ per pH unit (–9.1 ± 4.6 mV). H, activation time constants τ_{fast} and τ_{slow} as function of pH_i while pH_o = 7 (see also Appendix Table 15). The dashed lines are linear fits with slope(τ_{fast}) = –0.8 log(s)/ΔpH unit, r^2 = 0.3, $p < 0.05$, and slope(τ_{slow}) = –0.6 log(s)/ΔpH unit, r^2 = 0.4, $p < 0.05$. I, activation time constants τ_{fast} and τ_{slow} as function of pH (ΔpH = 0, see also Appendix Table 15). The dashed lines are linear fits with slope(τ_{fast}) = 0.3 log(s)/pH unit, r^2 = 0.2, $p < 0.05$, and slope(τ_{slow}) = 0.4 log(s)/pH unit, r^2 = 0.3, $p < 0.05$. Error bars indicate the SD.

3.2.2. S4 motion is similar for different symmetric pH, but depends on ΔpH

To identify the molecular mechanism of the coupling between voltage- and ΔpH-sensing, I studied the underlying conformational changes of Hv1. Previous studies showed that S4 is the main voltage sensor that moves outwardly upon depolarization (Gonzalez *et al.*, 2010; Tombola *et al.*, 2010; Mony *et al.*, 2015). Using the PCF technique (Zheng & Zagotta, 2003; Berger & Isacoff, 2015; Mony *et al.*, 2015), I investigated whether altering ΔpH alone can change the S4 conformation. As readout for conformational changes, I used MTS-TAMRA (Fig. 2.4A). For MTS-TAMRA labeling, a single cysteine was introduced at position L245C, which is located at the extracellular end of S4 (Takeshita *et al.*, 2014) (Fig. 3.10A). Introduction of a cysteine or labeling can change key characteristics of Hv1. The $V_{1/2}$ of ciHv1-L245C-TAMRA, however, still depends on ΔpH (Fig. 3.10B and Appendix Table 14), showing that the labeling site and the fluorophore can be used to monitor conformational changes. Here, I probed S4 conformational changes by stepping from – 80 to –40 or +40 mV such that the Hv1 channels preferentially populate the activated closed state or the activated open state, respectively. Upon a voltage step from a holding potential of – 80 to –40 mV (activated closed state), the fluorescence of ciHv1-L245C-TAMRA decreased. The change was reversible: upon stepping back to –80 mV, the fluorescence intensity returned to its original value (Fig. 3.10C *top*). This F_{Signal} is consistent with a previous study (Qiu *et al.*, 2013) and was interpreted as the initial outward S4 motion during voltage sensing. F_{Signal} is similar in overall shape (Fig. 3.10C *top*) and amplitude (F_{signal} [%] = 5 ± 5; 4 ± 4; 6 ± 7) for various symmetric pH conditions (pH_i = pH_o = 6.5, 7.0, or 7.5, respectively, thus ΔpH = 0; one-way ANOVA, p = 0.6). The activation kinetics tend to be faster in acidic conditions; the differences were, however, not significant (Fig. 3.10D). Likewise, the deactivation kinetics do not depend on the pH itself (Fig. 3.10F).

A voltage step from a holding potential of –80 to +40 mV (activated open state) led to a more complex F_{Signal}: a biphasic decrease of the fluorescence intensity. In addition, upon stepping back to –80 mV, the fluorescence further decreased and then returned back to baseline, producing a characteristic “hook” in the fluorescence (Fig. 3.10C *bottom*). Such an F_{Signal} was also

observed in a previous study (Qiu *et al.*, 2013) and was interpreted to indicate voltage-dependent activation from a resting closed state (high fluorescence intensity) via an activated closed state (low fluorescence intensity) to an activated open state (intermediate fluorescence intensity). Like F_{Signal} at –40 mV, F_{Signal} at +40 mV is similar in overall shape at various symmetric pH conditions ($pH_i = pH_o$ = 6.5, 7.0, or 7.5; thus $\Delta pH = 0$; Fig. 3.10C *bottom*). However, some kinetics change for different symmetric pH conditions: at +40 mV, but not at –40 mV, the fast and slow activation kinetics of F_{signal} are significantly faster at acidic than at alkaline pH (Fig. 3.10D, E, Appendix Table 16). This might suggest that the transition of the intermediate to the open state is dependent on the pH itself. Interestingly, it has been predicted for human Hv1 that intermediate states are particularly dependent on pH_i (Villalba-Galea, 2014). The deactivation kinetics did not change for different symmetric pH conditions (Fig. 3.10F, G, Appendix Table 16). By stepping from –80 mV to –40 mV, only small inward currents were elicited, suggesting that only few channels opened and therefore the fluorescence signal reports mostly on closed-state channel transitions. This is supported by a G/G_{max} of about 0.2 for $\Delta pH = 0$ at –40 mV (Fig. 3.10B), showing that 20 % of the channels were open and 80 % of the channels remained in a non-conducting state.

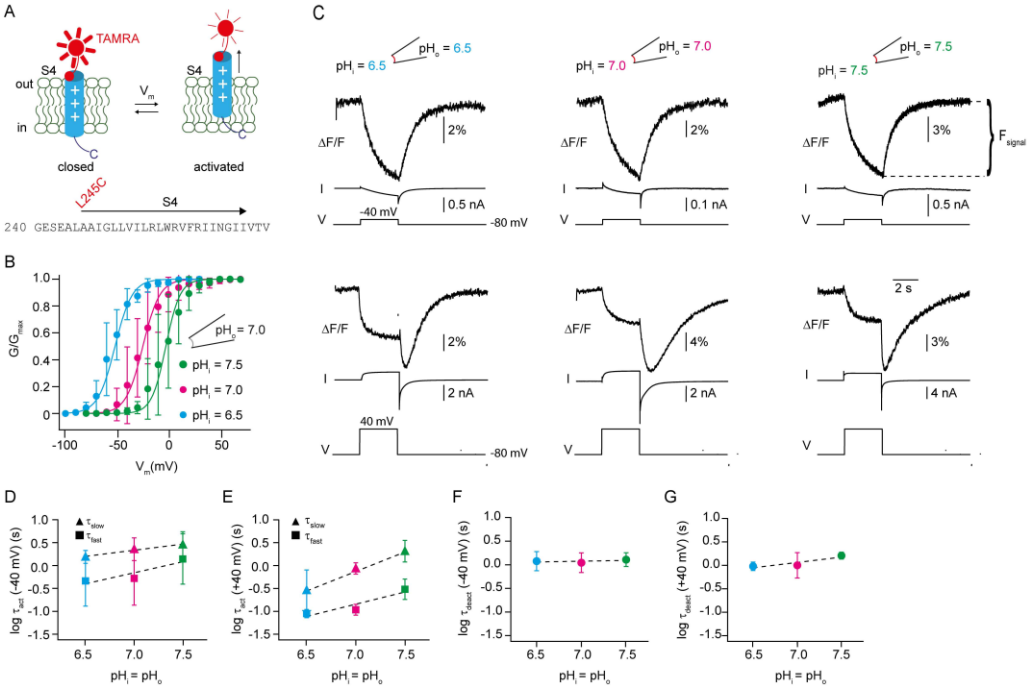

Figure 3.10. Voltage-evoked S4 fluorescence signal is not sensitive to pH itself. *A, top*, cartoon depicting voltage-evoked S4 conformational change of ciHv1-L245C-TAMRA. For clarity, only S4 is shown. "+" signs denote the charged arginines in S4. *Bottom*, amino-acid sequence of the S4 voltage sensor of ciHv1 and the site of labeling. *B,* GVs derived from tail currents of inside-out

patch-clamp recordings of ciHv1-L245C-TAMRA at different ΔpH conditions, fitted with Boltzmann functions (see Appendix Table 14 for fit parameters). *C,* representative inside-out PCF recordings of ciHv1-L245C-TAMRA, in response to voltage steps from –80 to –40 (*top*) or +40 mV (*bottom*) at different pH conditions leaving ΔpH = 0. (*D-E*), mean activation time constants τ_{fast} and τ_{slow} of F_{signal} at −40 mV (panel D) or +40 mV (panel E) as a function of pH (see also Appendix Table 16). The dashed lines are linear fits with the following slopes: slope(τ_{fast}) = 0.5 log(s)/pH unit, r^2 = 0.2, n.s., and slope(τ_{slow}) = 0.3 log(s)/pH unit, r^2 = 0.1, n.s., at −40 mV; slope(τ_{fast}) = 0.5 log(s)/pH unit, r^2 = 0.6, $p < 0.05$ and slope(τ_{slow}) = 0.9 log(s)/pH unit, r^2 = 0.5, $p < 0.05$, at +40 mV. (*F-G*) mean deactivation time constants τ_{deact} of F_{signal} during repolarization from −40 mV (panel F) or +40 mV (panel G) to −80 mV as function of pH (see also Appendix Table 16). The dashed lines are linear fits with the following slopes: slope(τ_{deact}) = 0.03 log(s)/pH unit, r^2 = 0.005, n.s., for −40 mV; slope(τ_{deact}) = 0.2 log(s)/pH unit, r^2 = 0.3, n.s., for +40 mV. Error bars indicate the SD.

I next tested whether changes in ΔpH affect the voltage-dependent motion of the S4 voltage sensor. While recording from an excised inside-out patch containing ciHv1-L245C-TAMRA, I changed ΔpH by switching to bath solutions of different pH_i, whereas pH_o was kept constant (7.0), and repetitively stepped V_m from –80 mV to –40 mV and back (Fig. 3.11A). For clarity, the average of the F_{signal} is shown in Fig. 3.11B. When a more acidic solution was washed in (pH_i = 6.5, resulting in ΔpH = 0.5), the characteristic F_{signal} under symmetric pH conditions ($pH_i = pH_o$ = 7, ΔpH = 0) was drastically altered in two aspects: first, F(–80 mV) was lowered, indicating that changes in ΔpH affect the S4 conformation in a non-conducting closed state (Fig. 3.11A, B). Second, the voltage step to –40 mV induced an increase rather than a decrease of F_{signal} compared to the ΔpH = 0 condition; upon stepping back to –80 mV, the fluorescence returned to baseline fluorescence intensity (Fig. 3.11A, B). At more alkaline pH_i (pH_i = 7.5, ΔpH = –0.5), the baseline fluorescence and F_{signal} resembled those under ΔpH = 0 conditions (Fig. 3.11A, B). Fig. 3.11C shows the mean amplitudes of the F_{signal} and the normalized F(–80 mV) at different ΔpH. Taken together, these data indicate that changes in pH_i that introduce a ΔpH > 0 can alter the S4 conformation in a non- conducting state, suggesting that S4 conformation is not only sensitive to the membrane potential, but also sensitive to changes in ΔpH.

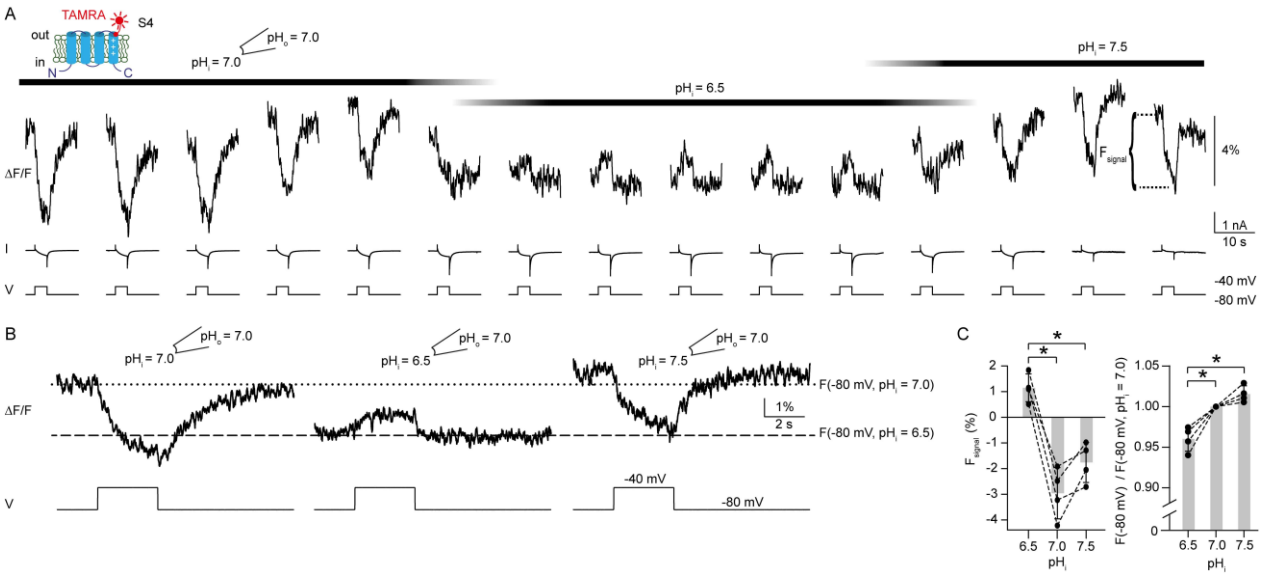

Figure 3.11. Changes in pH_i induce S4 conformational changes. *A*, representative inside-out PCF recording of ciHv1-L245C-TAMRA in response to repetitive voltage steps from –80 mV to –40 mV and back while changing pH_i and keeping pH_o = 7.0. The voltage-evoked fluorescence signal is denoted as F_{signal}. *B*, mean fluorescence signals calculated from (A) for different pH_i while pH_o = 7.0. Horizontal lines (dotted, pH_i = 7.0; dashed, pH_i = 6.5) indicate the average fluorescence at – 80 mV. *C, left*, amplitude of F_{signal} as a function of pH_i while pH_o = 7.0 (n = 4 patches from 4 different cells). For pH_i = 6.5, F_{signal} = 1.1 ± 0.5; for pH_i = 7.0, F_{signal} = –3.0 ± 1.0; for pH_i = 7.5, F_{signal} = –1.8 ± 0.8; repeated measures ANOVA, p = 0.0001; *post-hoc* analysis: F_{signal} for pH_i =7.0 vs. F_{signal} for pH_i =6.5: p = 0.0001; F_{signal} for pH_i =7.0 vs. F_{signal} for pH_i =7.5: p = 0.1; F_{signal} for pH_i =6.5 vs. F_{signal} for pH_i =7.5: p = 0.002. *Right*, baseline fluorescence at –80 mV (F(–80 mV)) as a function of pH_i while pH_o = 7.0, normalized to F(–80 mV) at pH_i = 7.0 (n = 4 patches from 4 different cells). For pH_i = 6.5, F(–80 mV) = 0.96 ± 0.02; for pH_i = 7.5, F(–80 mV) = 1.02 ± 0.01; repeated measures ANOVA: p = 0.002; *post-hoc* analysis: F(–80 mV) for pH_i = 7.0 vs. F(–80 mV) for pH_i = 6.5, p = 0.001; F(–80 mV) for pH_i = 7.0 vs. F(–80 mV) for pH_i = 7.5, p = 0.15; F(–80 mV) for pH_i = 6.5 vs. F(–80 mV) for pH_i = 7.5, p = 0.0001. * indicates statistically significant difference (p < 0.5). Error bars indicate the SD.

To further corroborate that the S4 conformation is sensitive to changes in ΔpH (and therefore independent of the side of pH change), I tested whether changes in ΔpH introduced by changing pH_o can also alter the S4 conformation. I changed ΔpH, while recording from an excised outside-out patch, by switching to solutions of different pH_o, whereas pH_i was kept constant (7.0), and repetitively stepped V_m from –80 mV to +20 mV and back (Fig. 3.12A). Averages of F_{Signal} from Fig. 3.12A are shown in Fig. 3.12B. When a more alkaline solution was washed in (pH_o = 8.0, ΔpH = 1.0), the F(–80 mV) and F_{signal} under symmetric pH conditions (pH_i = pH_o = 7, ΔpH = 0) were similarly altered as the F(–80 mV) and F_{signal} recorded from inside-out patches in the similar ΔpH conditions: first, F(–80 mV) was lowered, affirming that changes in ΔpH affect the S4

conformation in a non-conducting closed state (Fig. 3.12A, B). Second, the voltage step to +20 mV induced an increase rather than a decrease of the fluorescence compared to the ΔpH = 0 condition; upon stepping back to –80 mV, the fluorescence returned to baseline fluorescence intensity (Fig. 3.12A, B). At more acidic pH_o (pH_o = 6.0, ΔpH = –1.0), the F(–80 mV) and F_{Signal} resembled those under ΔpH = 0 conditions (Fig. 3.12A, B). This indicates that a ΔpH > 0 changes S4 conformation in a non-conducting state, independent of the site of pH change.

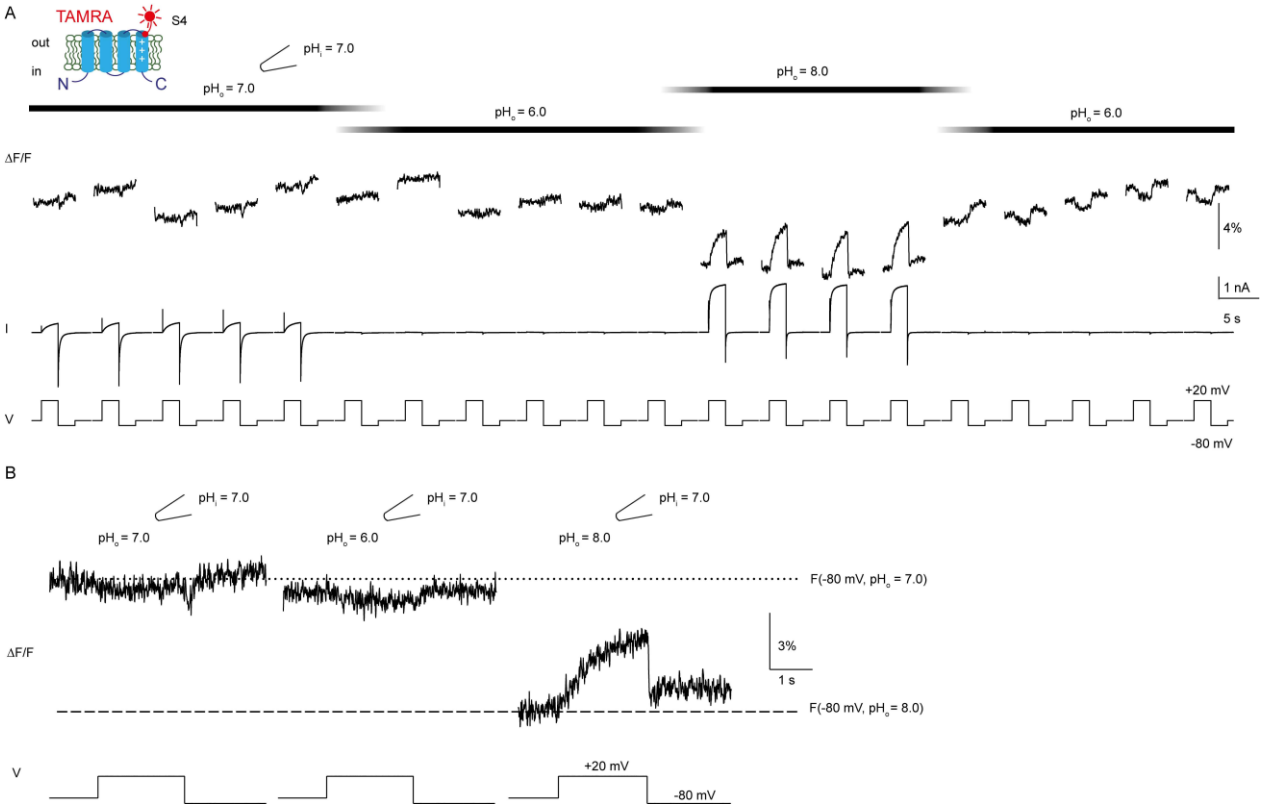

Figure 3.12. Changes in pH_o induce S4 conformational changes. *A*, representative outside-out PCF recording of ciHv1-L245C-TAMRA in response to repetitive voltage steps from –80 mV to +20 mV while changing pH_o and keeping pH_i = 7.0. *B*, mean F_{signal}s calculated from (A) for different pH_o while pH_i = 7.0. Horizontal lines (dotted, pH_o = 7.0; dashed, pH_o = 8.0) indicate the average fluorescence at –80 mV.

3.2.3. S1 motion is not uncoupled from channel opening by changes in pH_i

During pore opening, Hv1 undergoes an additional conformational change that can be monitored fluorometrically at the extracellular end of S1 (position I175C in ciHv1) (Mony *et al.*, 2015). To test whether a change in ΔpH also directly affects S1 motion, PCF recordings were done on ciHv1-I175C (Fig. 3.13A). During recording from an excised inside-out patch containing ciHv1-I175C-TAMRA, I changed ΔpH by switching to solutions of different pH_i, while pH_o was kept constant (7.0) and repetitively stepped V_m from – 80 mV to +40 mV and back (Fig. 3.13A). To better compare outward currents and fluorescence, normalized averages of the data from Fig. 3.13A are shown in Fig. 3.13B. As reported previously (Mony *et al.*, 2015), in response to a voltage step from –80 mV to +40 mV, the S1 F_{signal} and the outward current both increase with similar kinetics (Fig. 3.13A, B, C, Appendix Table 17). In contrast to the S4 F_{signal}, the S1 F_{signal} does not change much when ΔpH is changed: F(–80 mV) did not change and the sign of S1 F_{Signal} remained positive (Fig. 3.13D). To show that the direction of current alone is not sufficient to determine the sign and kinetics of the fluorescence change, I recorded from the double mutant ciHv1-I153C-I175C-TAMRA (Fig. 3.13E): as shown previously (Mony *et al.*, 2015), the I153C mutation shifts the GV relationship to more negative potentials as compared to WT background, so that inward currents can be recorded at negative membrane potentials and symmetric pH conditions. The same holds for ciHv1-I153C-I175C-TAMRA, allowing to record inward currents at -10 mV and outward currents at 10 mV. For both conditions, the S1 F_{Signal} recorded at position I175C is positive and does not change the sign, confirming that the direction of current does not change the sign of the S1 F_{Signal}. The kinetics of the S1 F_{Signal} and the outward current co-varied for different ΔpH: intracellular acidification accelerated and alkalization decelerated kinetics of both the S1 F_{Signal} and the outward current (Fig. 3.13C). Thus, current and S1 F_{Signal} kinetics stay coupled even when ΔpH is changed, corroborating that ΔpH- and voltage-sensing are linked to each other via the S4 voltage sensor.

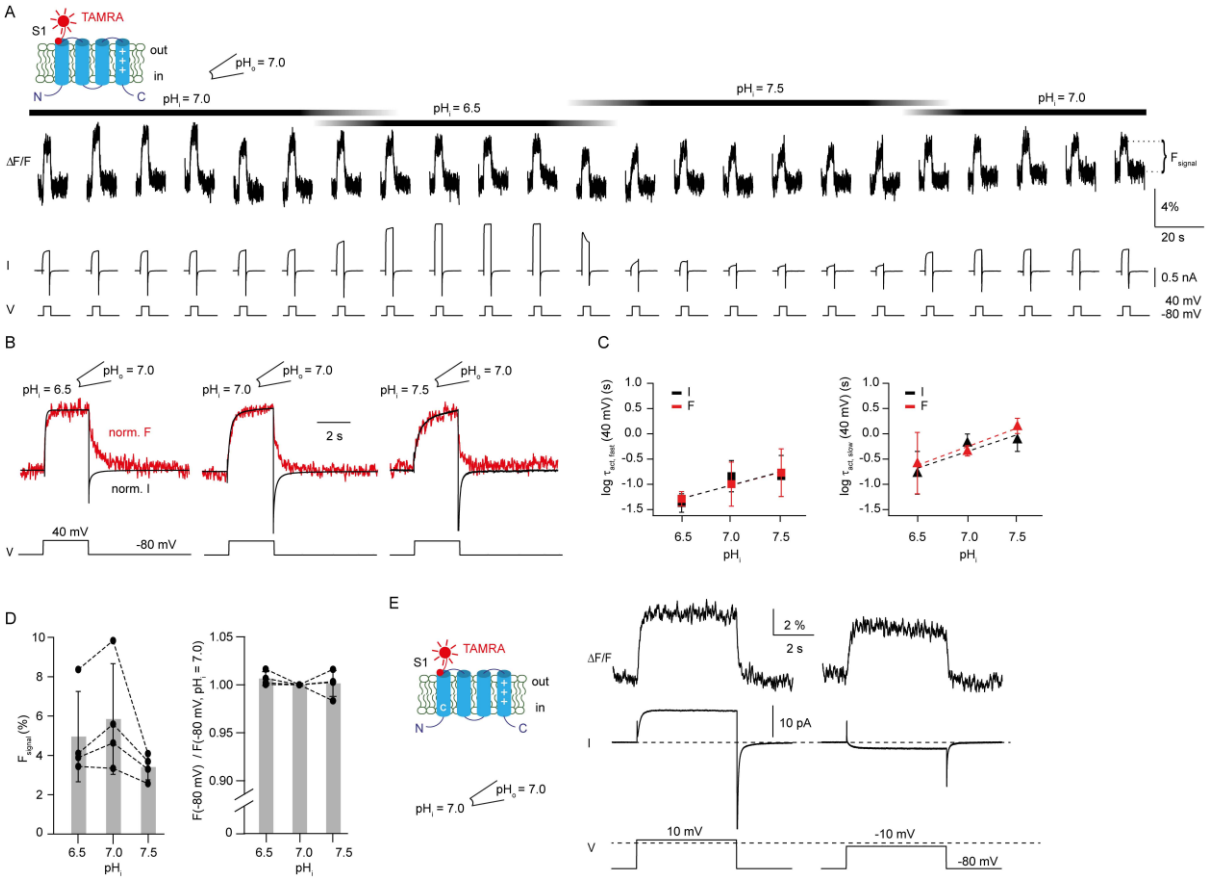

Figure 3.13. Changes in pH$_i$ do not uncouple gating from S1 motion. *A*, representative inside-out PCF recording of ciHv1-I175C-TAMRA in response to repetitive voltage steps from –80 mV to +40 mV and back while changing pH$_i$ and keeping pH$_o$ = 7.0. *B*, overlay of normalized mean current and fluorescence derived from the recording in (A). *C*, mean fast (*left*) and slow (*right*) activation time constants of current (black) and F$_{Signal}$ (red) of ciHv1-I175C-TAMRA as function of pH$_i$ while pH$_o$ = 7 (see also Appendix Table 17). The dashed lines are linear fits with the following slopes: slope($\tau_{I\ fast}$) = –0.5 log(s)/ΔpH unit, r^2 = 0.3, n.s.; slope($\tau_{F\ fast}$) = –0.5 log(s)/ΔpH unit, r^2 = 0.4, $p < 0.05$; slope($\tau_{I\ slow}$) = –0.67 log(s)/ΔpH unit, r^2 = 0.5, $p < 0.05$; slope($\tau_{F\ slow}$) = –0.73 log(s)/ΔpH unit, r^2 = 0.5, $p < 0.05$; slope($\tau_{I\ fast}$) vs. slope($\tau_{F\ fast}$), n.s.; slope($\tau_{I\ slow}$) vs. slope($\tau_{F\ slow}$), n.s. *D*, *left*, amplitude of F$_{signal}$ as a function of pH$_i$ while pH$_o$ = 7.0 (n = 4 patches from 4 different cells). For pH$_i$ = 6.5, F$_{signal}$ = 5.0 ± 2.3; for pH$_i$ = 7.0, F$_{signal}$ = 5.8 ± 2.8; for pH$_i$ = 7.5, F$_{signal}$ = 3.4 ± 0.6; repeated measures ANOVA, p = 0.08. *Right*, baseline fluorescence at –80 mV (F(–80 mV)) for different pH$_i$ while pH$_o$ = 7.0, normalized to F(–80 mV) for pH$_i$ = 7.0 (n = 4 patches from 4 different cells). For pH$_i$ = 6.5, F(–80 mV) = 1.006 ± 0.007; for pH$_i$ = 7.5, F(–80 mV) = 1.001 ± 0.013; repeated measures ANOVA, p = 0.65. *E*, representative inside-out PCF recording of ciHv1-I153C-I175C-TAMRA in response to voltage steps from –80 to +10 (*left*) or –10 mV (*right*). Dashed line at the *bottom* indicates 0 mV. Error bars indicate SD.

Taken together, the PCF data are consistent with the idea that higher proton concentrations at the intracellular side (low pH_i, $\Delta pH > 0$) or a positive membrane potential push S4 to the extracellular side and *vice versa*, higher proton concentrations at the extracellular side (low pH_o, $\Delta pH < 0$) or a negative membrane potential push S4 to the intracellular side (Fig. 3.14A). This suggests that both ΔpH and voltage determine the position of S4 in the membrane (Fig. 3.14B).

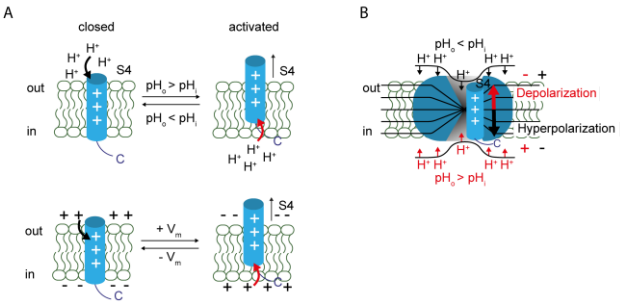

Figure 3.14. ΔpH and the membrane potential both control S4 conformation. *A*, proposed S4 conformation in the membrane as a function of either ΔpH (*top*) or voltage (*bottom*). Protons on one side of the membrane move S4 to the opposite side of the membrane (*top*), similar to the effect of membrane voltage (*bottom*). S1-S3 are omitted for clarity. "+" signs denote the charged arginines in S4. *B*, cartoon depicting how S4 position is determined by both voltage and ΔpH across the membrane. Protons might exert electrostatic forces on Hv1, i.e. by protonation of a water wire in the VSD. The position of the mobile S4 segment depends on both, the electrochemical potential for protons and the membrane potential: Excessive protons at the extracellular side ($pH_o < pH_i$) and/or hyperpolarization push S4 to the intracellular side, stabilizing the closed state. Excessive protons at the intracellular side ($pH_o > pH_i$) and/or depolarization push S4 to the extracellular side, stabilizing the activated state.

3.3. Proton uncaging

So far, I set the pH in the recording chamber by exchanging solution using a gravity-driven perfusion system connected to the recording chamber (Fig. 3.11A, 3.12A, 3.13A). Although the exchange of solutions in patch pipettes during a recording is also possible (Lapointe & Szabo, 1987), it is relatively slow and likely to be incomplete. Here, I developed another approach, combining patch-clamp and PCF with light-controlled proton uncaging (see Methods 2.4, Fig. 2.5B). To change the pH (i.e. lower the pH) in the patch pipette rapidly and without solution exchange (which can introduce artifacts), I used the photolytically cleavable cage 1-(2-nitrophenyl)ethyl sulfate (NPE-caged-proton).

3.3.1. Proton uncaging changes proton currents

NPE-caged-proton releases a sulfate and a proton in response to UV-light (Barth & Corrie, 2002) (Fig. 3.15A) on a ~100 ns time scale (Abbruzzetti *et al.*, 2005). Large pH jumps (down to about pH 2) can be achieved in solutions without pH buffer (Barth & Corrie, 2002). For defined pH changes evoked by proton uncaging, buffer and caged-compound concentrations need to be carefully considered (see Methods 2.4): if the buffer concentration is too high, it rapidly scavenges released protons and prevents or attenuates pH changes. If the buffer concentration, however, is too low, it prevents stable Hv1-mediated proton currents because small proton currents can change the pH on both sides of the membrane, changing not only the driving force for protons but also the open probability of the ΔpH-sensitive Hv1 channel. I tested whether 0.1 mM HEPES buffer with 500 µM caged compound in the pipette solution (Table 9), at the side of proton uncaging, and 100 mM HEPES in the bath solution allow for stable proton current recordings and sufficiently large UV light-induced pH changes.

I tested acidification at the extracellular side of the patch membrane in excised inside-out patches containing ciHv1 (Fig. 3.15). Prior to photolysis by UV light, robust outward proton currents (Fig. 3.15A, *left*) were recorded in response to voltage steps from –50 to +30 mV (mean I_{pre} = 44.4 ± 37.3 pA; n = 6). During depolarization, a 1-s long light stimulus first rapidly diminished

the outward current, then gave rise to an inward current, and finally abolished the current (mean time between onset of light stimulus and reversal of current: 0.05 ± 0.01 s, n = 6; mean I at time point indicated by arrow = –65.0 ± 49.0 pA, n = 6.; time between onset of stimulus and inward current peak: 0.4 ± 0.2 s, n = 6) (Fig. 3.15A, *right*). The recording is consistent with a light-induced extracellular acidification (and hence a change in the electrochemical driving force for protons) and the coupled ΔpH- and voltage-sensing of Hv1, as depicted in Fig. 3.15B: depolarization to +30 mV opens the proton channels and leads to a proton outward current (Transition 1). Light-induced extracellular acidification changes the electrochemical driving force for protons to such an extent that the proton current reverses direction (Transition 2, indicated by arrow in Fig. 3.15A). With depolarization to +60 mV, an inward current is also recorded that, however, is smaller in amplitude (Fig. 3.15C, indicated by arrow). This indicates that the light-induced extracellular acidification establishes a $\Delta pH < -1$. The negative ΔpH also closes the channel (Transition 3), implying that the open state of ciHv1 is also sensitive to ΔpH. Thus, it is indeed possible to change the pH in the patch pipette during recording. Subsequent depolarizing voltage steps after light application did not elicit proton currents (Fig. 3.15D). After several minutes, however, the proton-current amplitude recovered (Fig. 3.15D), showing that the initial pH at the extracellular side of the membrane (facing the lumen of the patch pipette) has been reestablished. This suggests that proton uncaging took predominantly place locally in the direct vicinity of the patch membrane (in the focal plane where light intensity is maximal) and not in the bulk volume of the patch pipette, and that subsequent diffusion of buffer and protons equilibrates the pH. If this is the case, NPE-caged-proton should diffuse from the bulk volume back to the vicinity of the patch membrane and allow further local uncaging. Indeed, after several minutes, a second light application again diminished the proton current (Fig. 3.15E,F). This also shows that the light stimulus does not degrade the functionality of the ciHv1 proton channel.

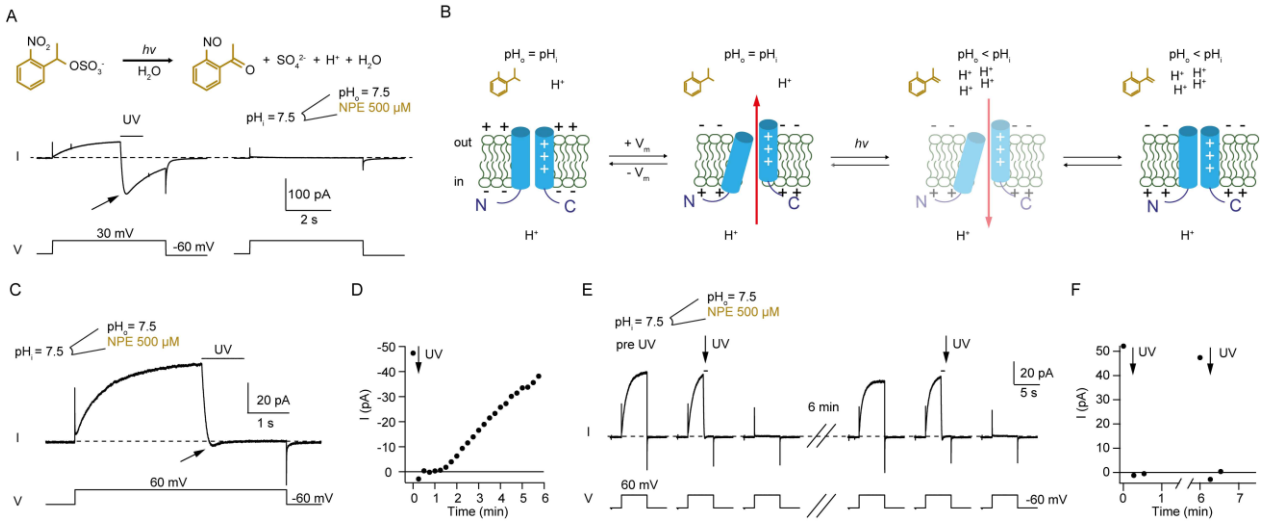

Figure 3.15. Proton uncaging on extracellular side allows for fast but transient acidification of pH$_o$. *A, top*, chemical structure and uncaging reaction of NPE-caged-proton. *Bottom,* representative inside-out patch-clamp recording of ciHv1 in response to repetitive voltage steps from –50 mV to +30 mV and -60 mV. UV light was applied for 1 s. Arrow indicates inward-current peak. The patch pipette contained 500 µM NPE-caged-proton buffered to pH$_i$ = 7.5 with 0.1 mM HEPES, while the bath solution was buffered to pH$_o$ = 7.5 with 100 mM HEPES. *B*, gating scheme of ciHv1. For clarity, only S1 and S4 are shown. "+" signs denote the charged arginines in S4. Red arrows indicate the direction of proton current. *C,* representative inside-out patch-clamp recording of ciHv1 as in (A), in response to repetitive voltage steps from –60 mV to +60 mV and back. *D*, current amplitude of stimulations in (C) over time (time point indicated by arrow in C). Arrow indicates light stimulus. *E,* representative inside-out patch-clamp recording of ciHv1 as in (A), in response to repetitive voltage steps from –60 mV to +60 mV and back. UV-light stimulation was applied twice to the same patch as indicated by the arrows; the pause between stimulations was approximately 6 minutes. *F*, maximal outward current amplitude of the recording in E over time. Arrows indicate iterations with light stimulus.

Next, I tested light-induced acidification by uncaging NPE-caged-proton at the intracellular side in excised outside-out patches containing ciHv1 (with 500 µM NPE-caged-proton and 0.1 mM HEPES buffer in the pipette solution; Table 9) (Fig. 3.16A). In addition to NPE-caged-proton, I tested sodium (6,7-dimethoxycoumarin-4yl)methyl sulfonate (DMCM-caged-proton), which releases a sulfate and a proton in response to UV light (Geißler *et al.*, 2005) (Fig. 3.16G). Prior to photolysis by light, no or minimal outward proton currents in response to voltage steps from –50 to +5 mV were recorded (for NPE-caged-proton, I_{pre} = 0.96 ± 0.9 pA, n = 6; for DMCM-caged-proton, I_{pre} = 0.9 ± 0.9 pA, n = 6) (Fig. 3.16A,B,E). Uncaging of NPE-caged-proton (Fig. 3.16A) as well as DMCM-caged-proton (Fig. 3.16B) by a 1-s-long light stimulus increased the proton-current amplitude significantly (for NPE-caged-proton, I_{post} = 5.5 ± 4.1 pA, p = 0.01; for DMCM-caged-

proton, I_{post} = 4.9 ± 1.6 pA, p < 0.01) (Fig. 3.16E). This suggests that uncaging of NPE-caged-proton (Fig. 3.16C) and DMCM-caged-proton (Fig. 3.16D) acidified the intracellular side of the membrane and increased the chemical driving force for protons and increased the opening probability of Hv1. The two cages were similar regarding their light-induced effect on current amplitude and time course of uncaging (Fig. 3.16E,F). Because I had only limited stock of DMCM-caged-proton, and because DMCM-caged-proton were not commercially available at the time of the experiments, I proceeded with NPE-caged-proton. Taken together, UV-light induced uncaging of NPE-caged-proton can rapidly and transiently acidify the pipette solution at the excised membrane patch.

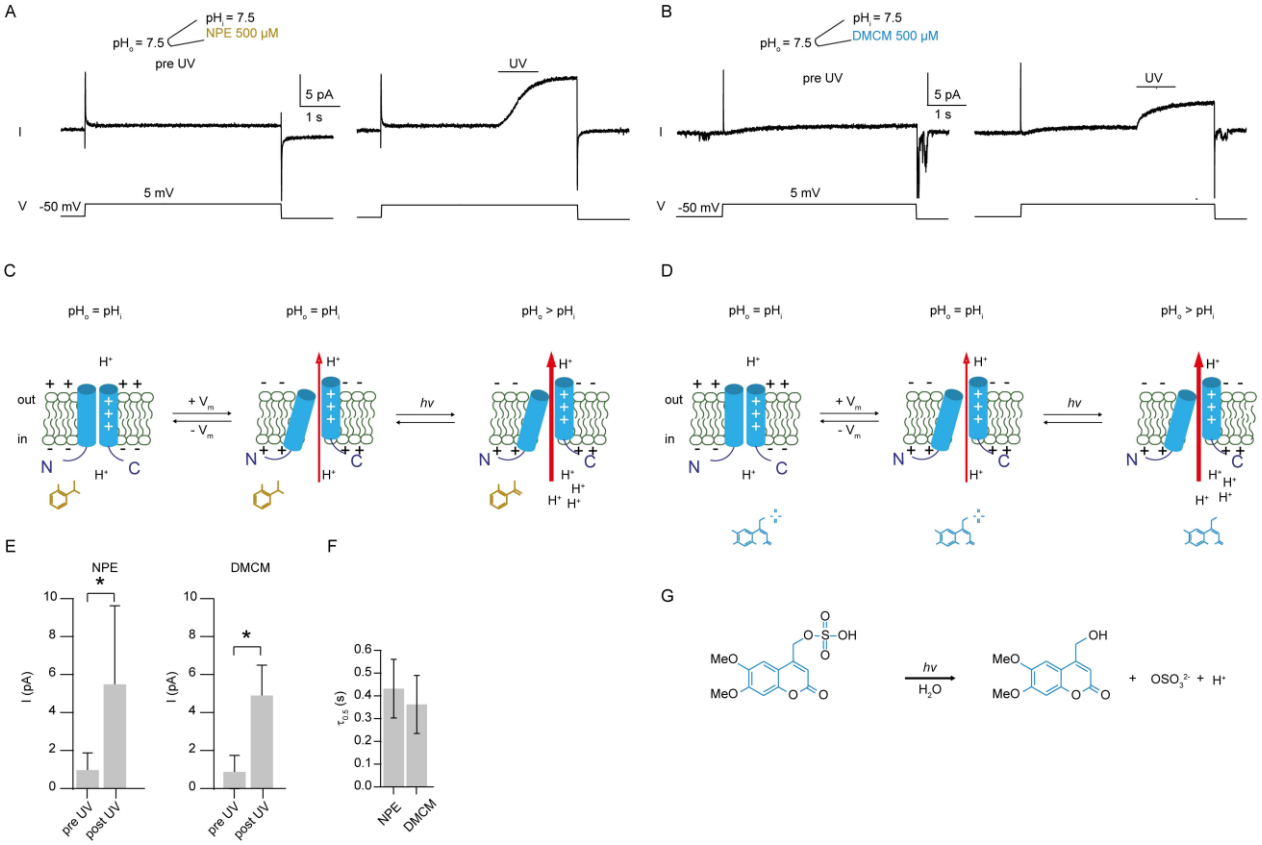

Figure 3.16. Proton uncaging on intracellular side allows for fast acidification of pH$_i$. *A,B*, representative outside-out patch-clamp recording of ciHv1 in response to repetitive voltage steps from – 50 mV to +5 mV and -60 mV. UV light was applied for 1 s. The patch pipette contained 500 µM NPE-caged-proton (A) or 500 µM DMCM-caged-proton (B) at pH$_i$ = 7.5, buffered with 0.1 mM HEPES; pH$_o$ was 7.5, buffered with 100 mM HEPES. *C,D,* gating scheme of ciHv1 with NPE- (C) or DMCM-caged-proton (D) at the intracellular side. For clarity, only S1 and S4 are shown. "+" signs denote the charged arginines in S4. Red arrows indicate the direction of proton current *E*, mean steady-state current amplitudes during depolarization to 5 mV of recordings as described in (A)

and (B) before and after UV with 500 µM NPE- (*left*) or DMCM-caged-proton (*right*) in the pipette. For NPE-caged-proton pre UV, I = 0.96 ± 0.9 pA; post UV, I = 5.5 ± 4.1 pA; n = 6 patches from 6 different cells; paired t-test, p = 0.01. For DMCM-caged-proton pre UV, I = 0.9 ± 0.9 pA; post UV, I = 4.9 ± 1.6 pA; n = 6 patches from 6 different cells; paired t-test, p < 0.01. *F*, time for half-maximal effect of light stimulation with 500 µM compound in the pipette. For NPE-caged-proton, $\tau_{0.5}$ = 0.43 ± 0.13 s, n = 6 patches from 6 different cells; for DMCM-caged-proton, $\tau_{0.5}$ = 0.36 ± 0.13 s, n = 6 patches from 6 different cells. *G*, chemical structure and uncaging reaction of DMCM-caged-proton. * indicates statistically significant difference (p < 0.5). Error bars indicate SD.

3.3.2. Proton uncaging can induce motion of the S4 segment

Next, I tested whether changing pH by proton uncaging can also induce conformational changes of the S4 voltage sensor. NPE-caged-proton was uncaged at the intracellular side of an outside-out patch containing ciHv1-L245C-TAMRA while at the same time changes of the fluorescence were recorded with PCF (Fig. 3.17A). The membrane patch was clamped at –80 mV throughout the experiment, keeping ciHv1-L245C-TAMRA in a non-conducting, closed state (Fig. 3.17B). During the 1-s long UV-light stimulus, which was bleeding through to the camera, no fluorescence could be recorded (Fig. 3.17B). After the light stimulus, the fluorescence decreased monotonically to a lower steady-state fluorescence intensity (Fig. 3.17B). The mean steady-state fluorescence ratio between after and before the light stimulus at –80 mV (F(–80 mV, post UV)/F(-80 mV, pre-UV)) decreased (Fig. 3.17D *left*), which agrees with the change in the fluorescence ratio in response to intracellular acidification (ΔpH > 0) by gravity-driven perfusion (Fig. 3.11C, *right*). Subsequent light stimulation further decreased the fluorescence intensity (Fig. 3.17B, bar label 2 and 3), however, to a lower extent, suggesting that most of the NPE-caged-proton present at the membrane were already released by the first light stimulus.

I next tested whether the UV light changes the properties of TAMRA directly. This is not expected, because the spectrum of the UV light (peaking at 365 nm) and the absorbance spectrum of TAMRA (peaking at 543 nm) do not overlap. Nevertheless, as the light stimulus is applied with high intensity (0.86 mW/mm^2), it might affect the fluorescence. To test whether 1 s of 365-nm light stimulus itself changes the fluorescence, e.g. by photobleaching, I recorded fluorescence from excised outside-out patches containing ciHv1-L245C-TAMRA, without NPE-caged-proton in the pipette. In this recoding condition, a UV-light stimulus did not change the fluorescence (Fig. 3.17E); F(–80 mV, post UV)/F(-80 mV, pre UV) without NPE-caged-proton was significantly less

decreased compared to F(–80 mV, post UV)/F(-80 mV, pre UV) with NPE-caged-proton ($p = 0.02$, Fig. 3.17D), suggesting that it is not the light stimulus directly but indeed the proton uncaging that is responsible for the change in fluorescence. Without NPE-caged-proton, the F_{signal} under symmetric pH conditions ($pH_i = pH_o = 7.5$, $\Delta pH = 0$) was still detectable after the 1 s-light stimulus (Fig. 3.17F, *right*), suggesting that TAMRA fluorophores were not significantly bleached after UV-light stimulations. Therefore, acidification by uncaging corroborates results from acidification by gravity-driven perfusion, suggesting that the decrease of fluorescence reports on movement of S4 in response to the ΔpH at –80 mV.

To test whether F_{signal} is also changed by proton uncaging, membrane patches were depolarized by voltage steps to –5 mV before and after proton uncaging. The mean F_{signal} (same patch as in Fig. 3.17A) is shown in Fig. 3.17C. When pH_i was lowered by proton uncaging, the F_{signal} was altered similarly as seen with gravity-driven perfusion of a solution with a lower pH_i: the voltage step to –5 mV induced an increase rather than a decrease of the fluorescence as compared to the $\Delta pH = 0$ condition; upon stepping back to –80 mV, the fluorescence returned to baseline-fluorescence intensity (compare Fig. 3.17 C with Fig. 3.11B), corroborating that proton uncaging affects S4 gating motion similar to gravity-driven ΔpH changes. Taken together, both methods - proton uncaging and gravity-driven perfusion - show that the S4 conformation changes when a ΔpH is applied (by lowering pH_i). I show here for the first time, that proton uncaging by UV light can be applied in PCF experiments to study gating of the Hv1 proton channel.

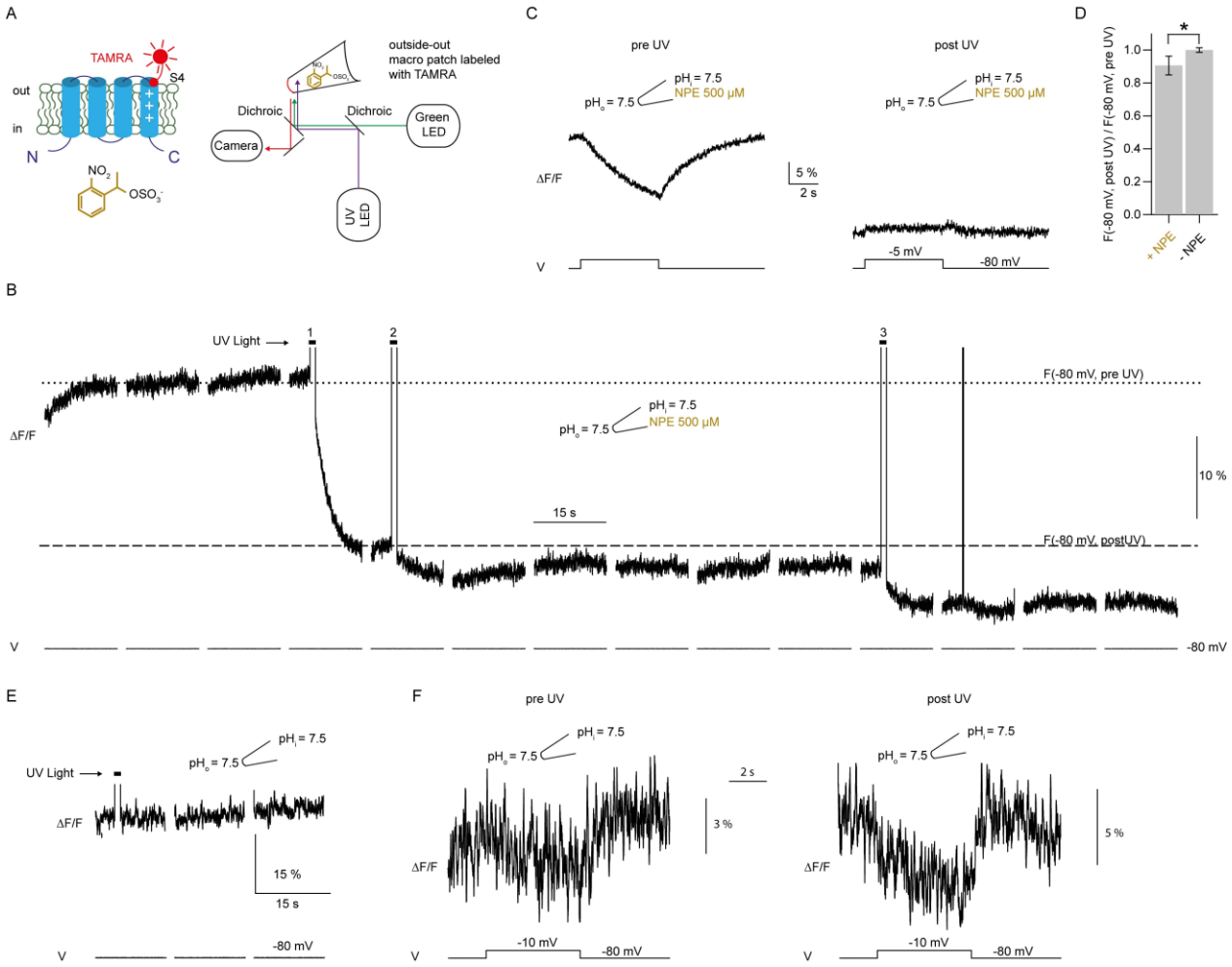

Figure 3.17. Proton uncaging changes S4 conformation in closed state. *A*, *left,* cartoon depicting ciHv1-245C-TAMRA and chemical structure of NPE-caged-proton at the intracellular side. *Right*, scheme of an outside-out PCF recording condition with NPE-caged-proton in the pipette. *B,* representative outside-out PCF recording of ciHv1-L245C-TAMRA held at –80 mV, and 1 s UV-light exposure at time points indicated by bars. Horizontal lines (dotted = pre UV, dashed = after UV) indicate the mean F(–80 mV). *C,* mean F_{signal}s in response to repetitive voltage steps from –80 mV to –5 mV before UV (*left*) and after UV (*right*). *D*, ratio of F(–80 mV) after and before 1 s UV-light exposure, with NPE-caged-proton (0.9 ± 0.06; n = 5 different patches from 5 different cells) and without NPE-caged-proton (1.0 ± 0.01; n = 3 different patches from 3 different cells), two-tailed t test with NPE-caged-proton vs. without NPE-caged-proton, p = 0.02. *E,* representative outside-out PCF recording of ciHv1-L245C-TAMRA held at – 80 mV, and 1 s UV-light exposure at time point indicated by bar. *F,* mean F_{signal}s of the same patch in response to repetitive voltage steps from – 80 mV to –5 mV before UV (*left*) and after UV (*right*). * indicates statistically significant difference (p < 0.5). Error bars indicate the SD.

3.4. pH-sensing of the voltage-sensing phosphatase ciVSP

To determine whether ΔpH-dependent S4 conformational changes are unique to Hv1, I examined ΔpH sensitivity of the S4 voltage sensor of another voltage-sensitive protein, the voltage-sensing phosphatase from *Ciona intestinalis* (ciVSP). Previous studies on ciVSP using VCF identified the S4 segment as the main voltage sensor (Kohout *et al.*, 2008; Villalba-Galea *et al.*, 2008). To monitor voltage-dependent motion of S4 by PCF, fluorescence from inside-out patches with ciVSP-G214C-TAMRA was recorded in response to voltage steps from –80 mV up to +90 mV. Depolarizations below +10 mV elicited no fluorescence changes, whereas depolarizations above +10 mV decreased the fluorescence (Fig. 3.18A). Amplitudes of F_{signal} increased with higher depolarization (Fig. 3.18A,B). Upon stepping back to –80 mV, the fluorescence intensity returned to its original value (Fig. 3.18A). The voltage-dependent changes in F_{signal} confirm previous VCF studies (Kohout *et al.*, 2008; Villalba-Galea *et al.*, 2008) and show that voltage-dependent motion of S4 can be observed by PCF experiments.

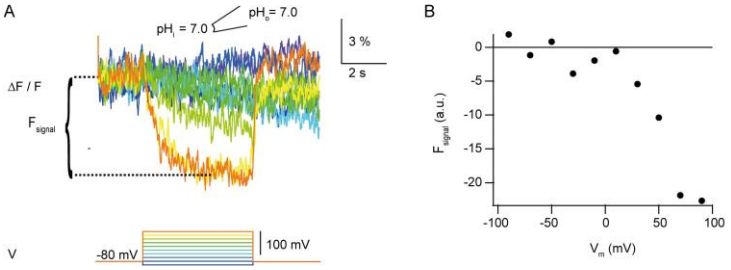

Figure 3.18. The S4 conformational change of ciVSP is voltage dependent. *A,* representative inside-out PCF recording of ciVSP-G214C-TAMRA in response to voltage steps from -90 mV to 90 mV. *B,* F_{signal}–voltage relationship of the data in A.

I next tested whether changes in ΔpH affect the F_{signal} of the S4 segment of ciVSP-G214C-TAMRA. I changed ΔpH in a recording from an excised inside-out patch by switching to solutions of different pH_i while pH_o was kept constant (7.0) and repetitively stepped V_m from –80 mV to +40 mV and back (Fig. 3.19A). For clarity, averages of the F_{signal} from Fig. 3.19A are summarized in Fig. 3.19B. In contrast to the fluorescence recorded from ciHv1-L245C-TAMRA, the fluorescence recorded from ciVSP-G214C-TAMRA does not change with pH_i: F(–80 mV) did not decrease (repeated measures ANOVA, p = 0.7; Fig 3.19D). The sign of F_{signal} remained negative and the amplitudes differed not significantly (repeated measures ANOVA, p = 0.2; Fig. 3.19C). Of note, a brief transient increase of fluorescence during the early phase of activation was visible in several

but not all recordings (arrow in Fig. 3.19B). This fluorescence component was not dependent on pH or patch configuration. Activation kinetics were not altered by different ΔpH (Fig. 3.19E; Appendix Table 18). Taken together, changing pH_i and thereby establishing ΔpH did not change TAMRA fluorescence, suggesting that S4 in ciVSP-G214C-TAMRA is not sensitive to pH_i.

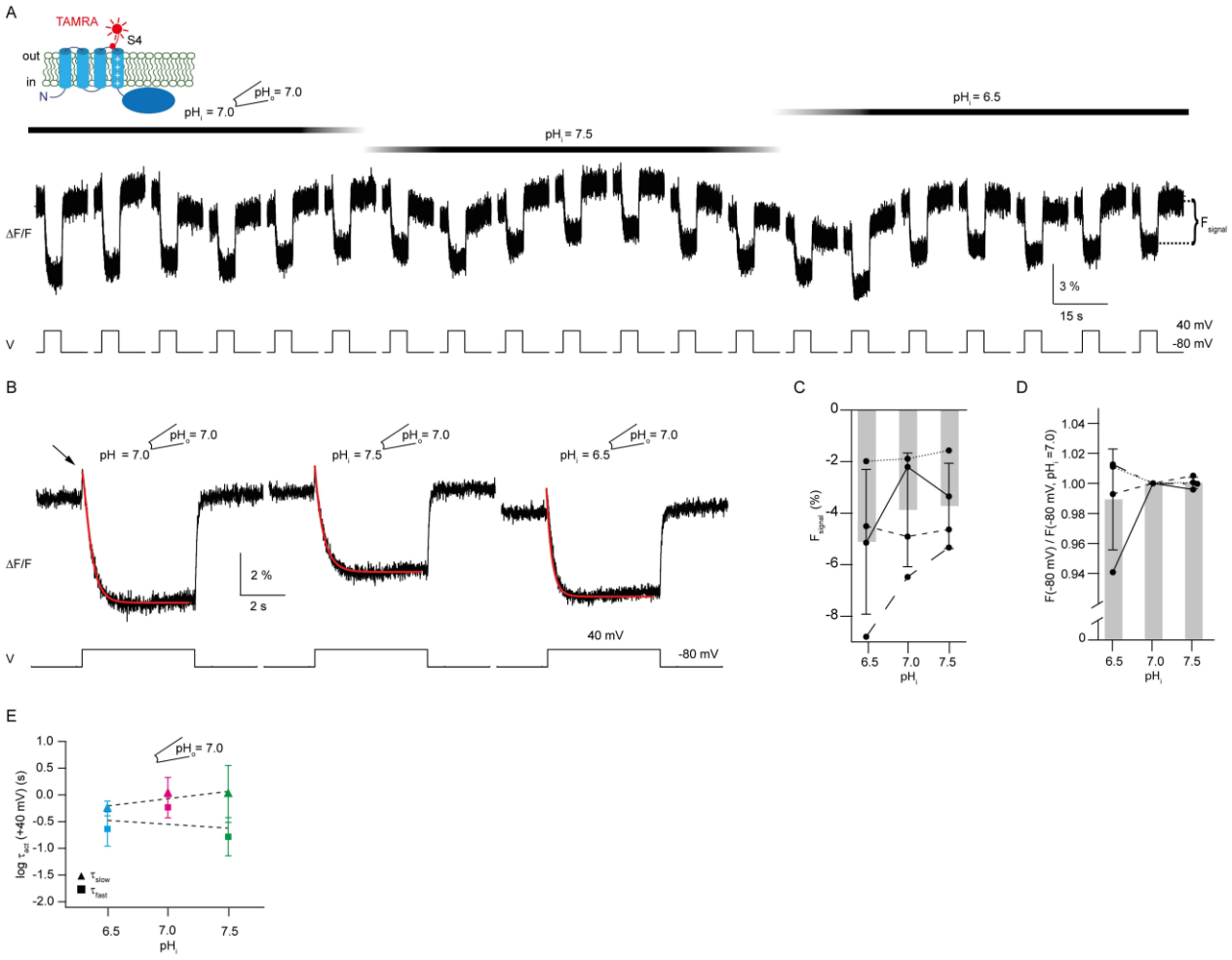

Figure 3.19. Changes in pH_i do not change voltage-induced S4 conformational change of ciVSP. *A,* representative inside-out PCF recording of ciVSP-G214C-TAMRA in response to repetitive voltage steps from –80 mV to 40 mV and back while changing pH_i and keeping pH_o = 7.0. *B*, mean F_{signal}s calculated from (A) for different pH_i while pH_o = 7.0. *C,* amplitude of F_{signal} as a function of pH_i while pH_o = 7.0 (n = 4 patches from 4 different cells). For pH_i = 6.5, F_{signal} = -5.1 ± 2.8; for pH_i = 7.0, F_{signal} = -3.9 ± 2.2; for pH_i = 7.5, F_{signal} = -3.7 ± 1.7. *D,* F(–80 mV) as a function of pH_i while pH_o = 7.0, normalized to F(–80 mV) at pH_i = 7.0 (n = 4 patches from 4 different cells). For pH_i = 6.5, F(–80 mV) = 0.99 ± 0.03; for pH_i = 7.5, F(–80 mV) = 1.00 ± 0.004. *E,* fast and slow activation time constants of F_{Signal} of ciVSP-G214C-TAMRA (derived from double-exponential fits as demonstrated in B) as function of pH_i while pH_o = 7 (n = 4 patches from 4 different cells); see Appendix Table 18. The dashed lines are linear fits with the following slopes: slope(τ_{fast}) = 0.2 log(s)/ΔpH unit, r^2 = 0.03, n.s.; slope(τ_{slow}) = –0.3 log(s)/ΔpH unit, r^2 = 0.1, n.s..Error bars indicate the SD.

To test whether S4 in ciVSP-G214C-TAMRA is sensitive to pH_o, I recorded the fluorescence from an excised outside-out patch in response to voltage steps from –80 mV to +40 mV and back, and switched to solutions of different pH_o while pH_i was kept constant (7.0) (Fig. 3.20A). Averages of the F_{signal} from Fig. 3.20A are summarized in Fig. 3.20B: at a more acidic pH (pH_o = 6.5, ΔpH = – 0.5), the F_{signal} amplitude was decreased compared to the F_{signal} amplitude in symmetric (ΔpH = 0) and alkalized pH conditions (pH_o = 7.5, ΔpH = 0.5). In contrast to the fluorescence recorded from ciHv1-L245C-TAMRA, the sign of F_{signal} remained negative (Fig. 3.20C). Yet, F_{signal} amplitudes at pH_o = 6.5 with ΔpH = –0.5 are significantly decreased compared to F_{signal} amplitudes at pH_o = 7.5 with ΔpH = 0.5 (repeated measures ANOVA, p = 0.02; Fig. 3.20C), suggesting that a change in pH_o can alter voltage-induced S4 motion. This is corroborated by recording activation kinetics for different pH_o conditions: the slow activation time constant of F_{signal} accelerates significantly at more alkaline pH_o (Fig. 3.20, E, Appendix Table 18). F(–80 mV) was not changed by these pH conditions (pH_o = 6.5, 7.0, 7.5) (repeated measures ANOVA, p = 0.5; Fig. 3.20A, B,D).

Here, I provide evidence that voltage-induced S4 motion in ciVSP is sensitive to pH_o. However, the pH-induced fluorescence changes in ciVSP are different from those in Hv1: F(– 80 mV) in ciVSP did not respond to pH_o- and pH_i- changes (Fig. 3.19, Fig. 3.20), suggesting that the resting-state conformation of S4 is neither sensitive to pH nor to ΔpH. In contrast, in Hv1, F(– 80 mV) decreased when changing pH_o and pH_i such that ΔpH becomes > 0 (Fig. 3.11, Fig. 3.12, Fig. 3.17), showing that ΔpH can change resting-state conformation in Hv1. F_{signal} in ciVSP was sensitive to pH_o (Fig. 3.20), but not to pH_i (Fig.3.19), whereas F_{signal} in Hv1 was sensitive to changes in pH_o and pH_i that led to ΔpH > 0 (Fig. 3.11, Fig. 3.12, Fig. 3.17). This data indicates different molecular mechanisms for pH sensing in ciVSP and ciHv1.

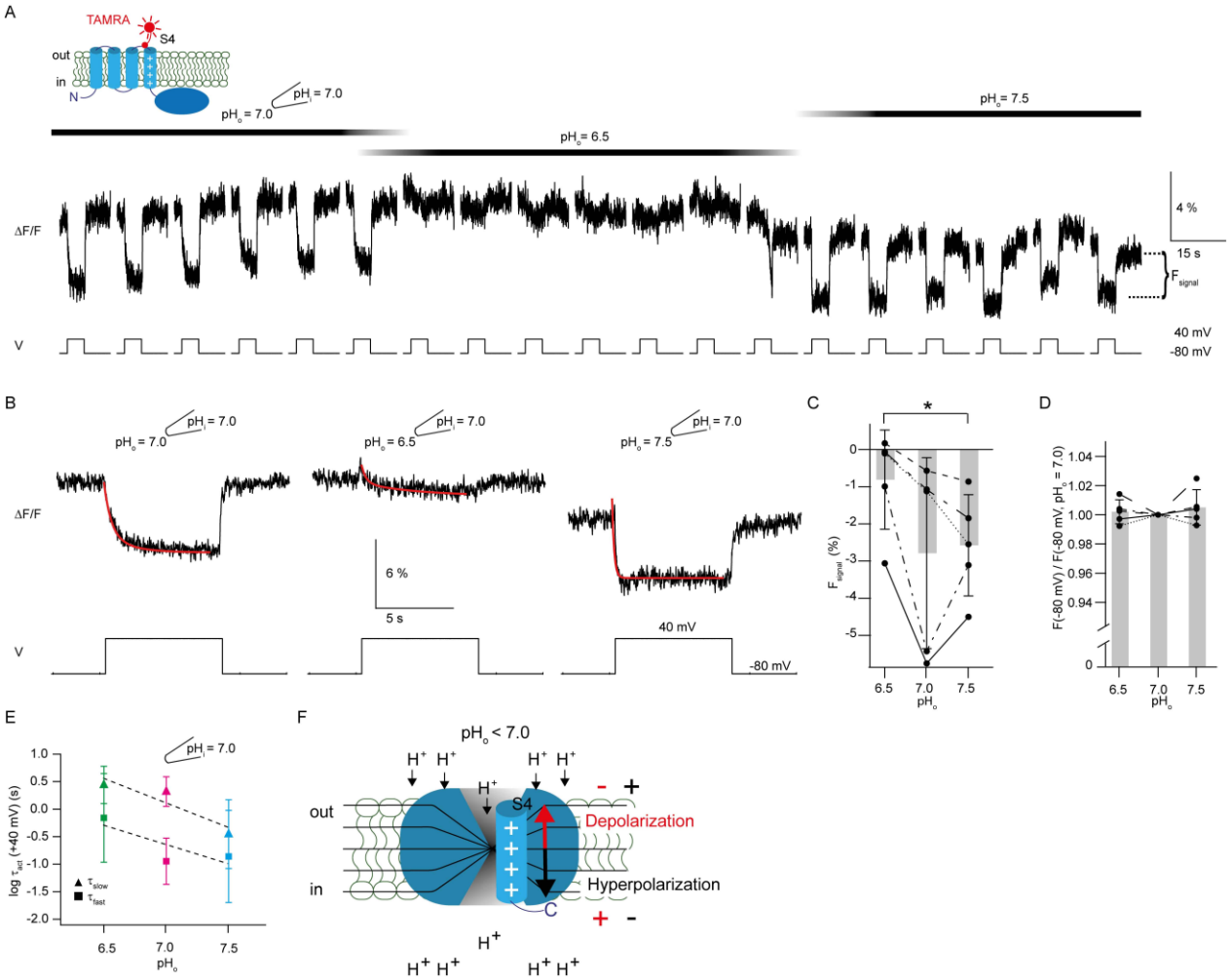

Figure 3.20. Changes in pH_o affect S4 conformational change. *A,* representative outside-out PCF recording of ciVSP-G214C-TAMRA in response to repetitive voltage steps from –80 mV to 40 mV and back while changing pH_o and keeping pH_i = 7.0. *B*, mean fluorescence signals calculated from (A) for different pH_o while pH_i = 7.0. *C,* amplitude of F_{signal} as a function of pH_o while pH_i = 7.0 (n = 5 patches from 5 different cells). For pH_i = 6.5, F_{signal} = -0.8 ± 0.1; for pH_i = 7.0, F_{signal} = -2.8 ± 2.6; for pH_i = 7.5, F_{signal} = -2.6 ± 1.4; repeated measures ANOVA, p = 0.02, p*ost-hoc* analysis: F_{signal} for pH_o =7.0 vs. F_{signal} for pH_o =6.5, p = 0.145; F_{signal} for pH_o =7.0 vs. F_{signal} for pH_o =7.5, p = 1.0; F_{signal} for pH_o =6.5 vs. F_{signal} for pH_o =7.5, p = 0.006. *D,* F(–80 mV) as a function of pH_o while pH_i = 7.0, normalized to F(–80 mV) at pH_o = 7.0 (n = 5 patches from 5 different cells). For pH_o = 6.5, F(– 80 mV) = 1 ± 0.01; for pH_o = 7.5, F(–80 mV) = 1.01 ± 0.01; repeated measures ANOVA, p = 0.5. *E,* fast and slow activation time constants of F_{Signal} of ciVSP-G214C-TAMRA (derived from double-exponential fits as demonstrated in B) as function of pH_o while pH_i = 7.0 (n = 3-5 patches from 3-5 different cells); see Appendix Table 18. The dashed lines are linear fits with the following slopes: slope(τ_{fast}) = -0.6 log(s)/ΔpH unit, r^2 = 0.1, n.s.; slope(τ_{slow}) = –1 log(s)/ΔpH unit, r^2 = 0.4, p < 0.05. Error bars indicate the SD. *F,* cartoon depicting VSP-VSD. S4 position is determined by voltage and pH_o, but not pH_i.

4. Discussion

The gating of Hv1 is complex because it depends on both the voltage and ΔpH across the membrane. Here, I combined PCF with chemical crosslinking of amino acids to resolve structure-function relationships in the Hv1 channel. Furthermore, using PCF and proton uncaging, I report evidence for S4 to serve both as voltage- and also as ΔpH sensor. These results provide novel insights into the molecular mechanism underlying ΔpH sensing and the coupling of voltage- and ΔpH sensing in Hv1.

4.1. A novel approach to investigate structure-function relationships in ion channels

Previous studies identified voltage-induced conformational changes of S1 and S4 by using voltage-clamp fluorometry (Gonzalez *et al.*, 2010; Tombola *et al.*, 2010; Qiu *et al.*, 2013, 2016; Berger & Isacoff, 2015; Mony *et al.*, 2015) and the cysteine-accessibility method (Gonzalez *et al.*, 2010; Mony *et al.*, 2015). Because structural information about open and closed states of full-length Hv1 under physiological conditions is missing, it is still not clear how S1 and S4 conformational changes look like, what constitutes the actual gate, and how conformational changes open and close the gate. Different models of open and closed states are debated (Larsson, 2020). Here, after studying full-length ciHv1, I provide functional data showing that the sulfur atoms of cysteines at 151C on S1 and 262C on S4 in ciHv1 can be crosslinked with MTS-1-MTS in a non-conductive state (Fig. 3.3, 3.7). Assuming that MTS-1-MTS can bridge a distance of 3-4 Å (Zhang *et al.*, 2002; Zhou *et al.*, 2011), my data indicate that the distance between the sulfur atoms of cysteines at 151C on S1 and 262C on S4 is approximately 3-4 Å in the resting or activated state. Given the maximal length of a cysteine side-chain of about 3.35 Å and the predicted length of MTS-1-MTS (Zhang *et al.*, 2002; Zhou *et al.*, 2011), I estimate the maximal Cα-Cα distance between amino-acid positions 151 and 262 in ciHv1 to be 9.7-10.7 Å in the resting or activated state (Fig. 4.1D). In the X-ray crystal structure of mHv1cc, which presumably represents a resting-state conformation, the Cα-Cα distance between the homologous positions is slightly larger (11.7 Å) (Takeshita *et al.*, 2014). In my homology model of ciHv1, which is based on the X-ray crystal

structure of mHv1cc, the Cα-Cα distance between positions 151 and 262 is 10.3 Å (Fig. 4.1A). Thus, the experimentally determined estimate of the Cα-Cα distance is close to the distance in the crystal structure and agrees with the distance estimate in the homology model. In contrast, the recent NMR-solution structure of N- and C-terminally truncated human Hv1 (Δ-Hv1), shows a considerable larger distance between homologous positions (16.6 Å) (Bayrhuber *et al.*, 2019). The NMR structure presumably represents an intermediate resting-state structure. Thus, the discrepancy in the Cα-Cα distance might be explained by structural differences between resting and intermediate-resting states, implying that conformational changes at the intracellular side of S1 and S4 might occur during activation of Hv1. However, the discrepancy in the Cα-Cα distance could also be explained by specific differences between human and ciHv1 orthologues.

Although my homology model of ciHv1 agrees with the experimentally determined estimate of the Cα-Cα distance, the model suggests that the native residue side-chains in S1 and S4 at position 151 and 262 do not point at each other in the resting state (Fig. 4.1A). This is also the case for the native residue side-chains at homologous positions in mHv1cc (Takeshita *et al.*, 2014) and Δ-Hv1 (Bayrhuber *et al.*, 2019) (Fig. 4.1B,C). *In silico* introduction of cysteines in my homology model of ciHv1 at position 151 and 262 suggests that the distance between the two engineered sulfur atoms is 8.8-12.3 Å rather than 3-4 Å. A conformational change, e.g., a helical rotation of S1, could position the engineered cysteine-side chains in the ciHv1-V151C-I262C mutant such that crosslinking with MTS-1-MTS is possible.

To further investigate the molecular mechanism of gating, I crosslinked cysteines with MTS-1-MTS while tracking conformational changes of S1 with the PCF technique. Interestingly, fluorescence changes in response to MTS-1-MTS wash-in showed that crosslinking 151C and 262C results not only in a pore block but also changes gating: A decrease in F_{signal} amplitude suggests that the crosslink inhibits the S1 conformational change. Furthermore, a decrease of F(– 80 mV) suggests that the crosslink stabilizes S1 in a less-frequently occupied resting-state conformation or forces S1 into a non-native resting-state conformation (Fig. 3.7). A conformational change, e.g., a helical rotation of S1, as mentioned above, could underlie the F(–80 mV) decrease. Possibly, the crosslink also changes S4-gating motion and/or the resting-state conformation of S4, however this still needs to be shown by crosslinking S4-labeled Hv1 channels in future experiments. Here, I report functional data showing that two residue side chains far apart from each other in the

NMR or X-ray structure can be crosslinked, implying larger conformational changes and a dynamic region at the intracellular side between S1 and S4 of Hv1.

Constraining the distance between the S1 and S4 segments on the intracellular side via crosslink inhibited S1-gating motion and impeded proton conduction. This result suggests that the distance between S1 and S4 on the intracellular side might change during transition from the resting to the open state. This is in line with cysteine-accessibility data in previous studies: during voltage sensing, in the Hv1 channel, solvent exposure decreases at the intracellular and increases at the extracellular ends of the S4 segment upon depolarization, suggesting a conformational change in form of a vertical motion of the S4 segment (Gonzalez *et al.*, 2010). In addition, during opening of the Hv1 channel, solvent exposure increases mainly at the intracellular but not at the extracellular side of the S1 segment (Mony *et al.*, 2015), suggesting a larger intracellular conformational change of the S1 segment. Channel opening supposedly results in large structural rearrangements that open up an intracellular vestibule that can fit open channel blockers (Hong *et al.*, 2013). The crosslink might prevent conformational changes of S1 that result in a widening of the intracellular vestibule during gating.

Future experiments using other flexible homo-bifunctional crosslinkers of the same chemical characteristics but of different lengths (Zhou *et al.*, 2008) may be useful to probe the widening of the intracellular vestibule. While the short MTS-1-MTS, which introduces the largest constraint, blocks the widening of the intracellular vestibule almost completely, longer, more flexible crosslinkers (Zhou *et al.*, 2008) should constrain gating movements less rigorously. Consequently, this may allow for gating motion that could be observed as the S1 F_{signal} and possibly also via proton-current recordings.

Crosslinking combined with the PCF technique could also probe the interdependence of the S1 and S4 conformational changes. The gating charge of Hv1 appears to reside in the arginine residues of S4 (Gonzalez *et al.*, 2013). Depolarization can induce an S4-conformational change that precedes the S1 conformational change and the actual pore opening (Mony *et al.*, 2015). This suggests that the S4 conformational change might cause the S1 conformational change. The dependence of S1 on S4 can be investigated by crosslinking S4 with a more static part of the channel (maybe S2 or S3) in channels where S1 is fluorescently labeled. Constraining S4 by the crosslink should thus also impede the S1 conformational change, which should then result in a

decrease in S1 F_{signal} amplitude (Fig. 4.1E). Similarly, the dependence of S4 on S1 could be investigated by crosslinking S1 with a non-moving part of the channel, in channels where S4 is fluorescently labeled (Fig. 4.1E). Recently, in human Hv1, a crosslink via a metal-ion bridge between residues on S1 (V109C) and on S2 (F150C) results in an open channel block (Geragotelis *et al.*, 2020). This indicates that the two engineered cysteines come close enough to coordinate Cd^+ in the open state, and Cd^+ binding stabilizes the open-state conformation (Geragotelis *et al.*, 2020). Crosslinking of engineered cysteines at homologous sites in ciHv1 (V157C on S1 and F198C on S2) via metal-ion bridge might also stabilize the open-state conformation of ciHv1 and constrain the S1 conformational change. Doing so in S4-labeled ciHv1 channels might clarify whether the S4 conformation depends on S1 conformational changes.

Taken together, crosslinking with MTS-1-MTS allowed distance measurements of the protein structure at hardly accessible sites, e.g., at the intracellular side of Hv1. In addition, I modified extra- and intracellular engineered cysteines in the same channel with different thiol-reactive molecules to combine PCF and crosslinking. This novel approach allowed to study the gating of Hv1 in more detail. Implications of crosslinking on gating revealed the functional state for binding of the crosslinker and whether the crosslinker acts as a pore blocker and/or as a blocker of gating motions. PCF combined with crosslinking holds the promise to advance structure-function studies in Hv1 and transmembrane proteins in general.

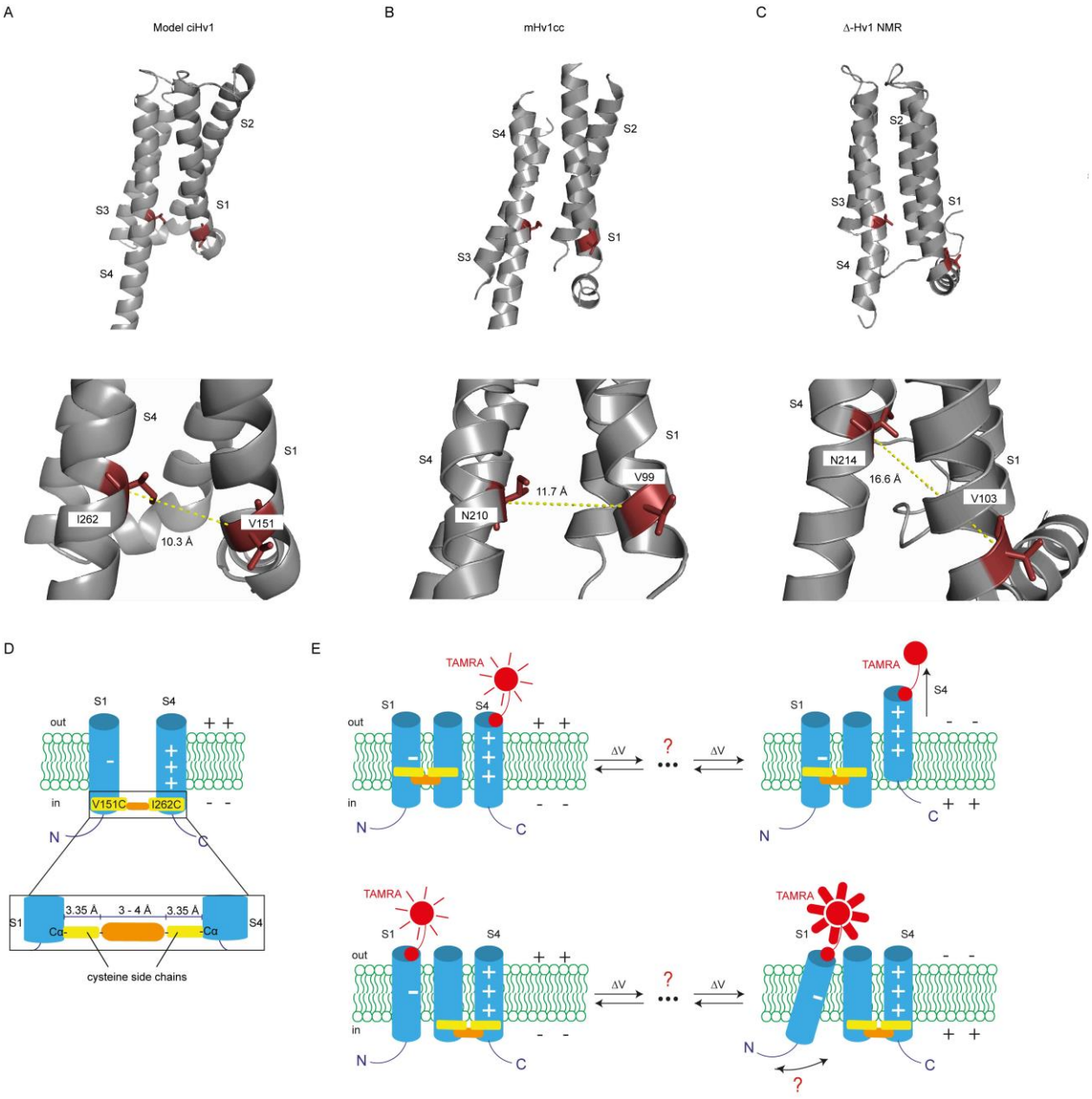

Figure 4.1. Comparison of the ciHv1 model and atomic Hv1 structures. *A-C, top*, homology model of ciHv1 (A), X-ray crystal structure of Hv1 chimera (B) adapted from (Takeshita *et al.*, 2014), NMR solution structure N- and C-terminally truncated human Hv1(Δ-Hv1) (C) adapted from (Bayrhuber *et al.*, 2019); *A-C, bottom*, close up of the respective structures. Residues V151 on S1 (*right*) and I262 (*left*) on S4 in ciHv1 homology model, as well as homologous residues in the other structures are marked in red. The dotted line stretches from Cα of I262 to Cα of V151, the value indicates the distance between the Cαs. *D,* cartoon, showing S1 and S4 of cysteine-double mutant ciHv1-V151C-I262C. Inset, close up showing estimated distances of cysteine side chains and MTS-1-MTS between Cα backbone of S1 and S4. *E,* gating scheme of an MTS-1-MTS-crosslinked Hv1 cysteine mutant. By crosslinking S1 to a non-moving part of the channel (segment between S1 and S4) and observing effects on S4 gating motion during depolarization in S4-labeled channels (*top*), together

with crosslinking S4 to a non-moving part of the channel (segment between S1 and S4) and observing effects on S1 gating motion during depolarization in S1-labeled channels (*bottom*) might clarify interdependencies of S1 and S4. “+” signs on S4 denote the charged arginines on S4, “-“ sign denotes a charged aspartate on S1 (D112 in human Hv1). For clarity, only three of the four segments are shown.

4.2. Potential molecular mechanism underlying ΔpH sensing

Several ion channels are gated or modulated by pH changes (Zheng & Trudeau, 2015). For some channels (e.g. two P-domain K^+ channels), the amino-acid residues that convey pH sensitivity, presumably by titration of acidic or basic side chains, are well characterized (Maingret *et al.*, 1999; Sandoz *et al.*, 2009). However, Hv1 is modulated by ΔpH rather than pH_i or pH_o itself. Although some mutations have been reported to alter ΔpH sensing of Hv1 (Ramsey *et al.*, 2010; Berger *et al.*, 2017; Cherny *et al.*, 2018), an unequivocal identification of amino-acid residues that constitute the ΔpH sensor(s) is lacking. Here, I provide evidence that the S4 segment changes its conformation in response to changes in ΔpH, suggesting that S4 serves as both voltage- and ΔpH-sensor.

During voltage-dependent gating, Hv1 undergoes multiple conformational changes (Gonzalez *et al.*, 2013; Qiu *et al.*, 2013; Villalba-Galea, 2014; De La Rosa & Ramsey, 2018; Carmona *et al.*, 2018). In a previous study, VCF recordings of S4-fluorescently labeled Hv1 showed that membrane depolarization drives at least two conformational changes of the S4 voltage sensor. The first conformational change precedes channel opening and moves the S4 voltage sensor to an activated state, which decreases the fluorescence intensity; a subsequent second conformational change correlates with the opening of the channel, which increases the fluorescence to an intermediate level (Qiu *et al.*, 2013). My PCF recordings agree with the VCF recordings from the previous study (Qiu *et al.*, 2013). In addition, taking advantage of precise intra- and extracellular pH control during PCF recordings, I show that the S4 F_{signal} is similar in overall shape and amplitude for different symmetric pH conditions (Fig. 3.10, ΔpH = 0). This suggests that the conformational changes of the voltage sensor, like voltage-dependent gating, do not depend on the pH itself. By contrast, asymmetric pH conditions can change the S4 F_{signal} (Fig. 3.11, 3.12, 3.17), suggesting that both voltage and ΔpH can drive S4 conformational changes. It remains to be tested in future experiments whether Hv1 enters unique conformational states when ΔpH is changed or whether the identical conformational states can be reached by changes in voltage while keeping ΔpH = 0. F(–80 mV) decreased when changing ΔpH = 0 to ΔpH = 0.5 (Fig. 3.11, 3.12, 3.17). Because most channels are closed at –80 mV for both ΔpH conditions (Fig.

3.10B), this data suggests that the closed state is sensitive to ΔpH (like it is sensitive to voltage). In addition, changing V_m from –80 to –40 mV while keeping ΔpH = 0 also decreases fluorescence (Fig. 3.10, 3.11) (and see also (Qiu *et al.*, 2013)). It is possible that the S4 voltage sensor might undergo the same conformational changes for both ΔpH and voltage stimulation. A voltage step from –80 to –40 mV at ΔpH = 0.5 resulted in a positive F_{signal}, whereas the same voltage step at ΔpH = 0 or ΔpH = –0.5 resulted in a negative F_{Signal} (Fig. 3.11). The positive F_{Signal} at ΔpH = 0.5 might correspond to the second conformational change of S4 that opens the channel as reported previously (Qiu *et al.*, 2013); the same voltage step at ΔpH = 0 just positions the voltage sensor into the activated state (Fig. 3.10) (and see also (Qiu *et al.*, 2013)). Thus, my data could be interpreted as being in line with the idea that ΔpH and voltage act in a similar fashion on the conformation of the S4 voltage sensor. Future PCF experiments that screen both the voltage and the ΔpH parameter spaces extensively should clarify whether voltage and ΔpH are equivalent stimuli for the Hv1 proton channel or whether ΔpH acts as an allosteric modulator.

In Hv1 mutant channels, gating currents, which reflect the movement of charged amino acids across the electric field of the membrane, were identified (De La Rosa & Ramsey, 2018; Carmona *et al.*, 2018). Interestingly, extracellular acidification by one pH unit (introducing ΔpH = –1) shifts the gating charge-voltage (QV) relationship of gating currents of human Hv1-W207A-N214R towards positive membrane potentials by 40 mV (De La Rosa & Ramsey, 2018). Because S4 contains the majority of gating charges (Gonzalez *et al.*, 2013), the pH_o sensitivity of gating currents suggests that the S4 conformation depends on pH_o, which agrees with my results (Fig. 3.12). Moreover, gating currents of monomeric ciHv1-D160N are sensitive to ΔpH: the QV relationship shifted by ~ –40 mV/ΔpH unit, but was not changed under different symmetric pH conditions (Carmona *et al.*, 2021). Quantification of the ΔpH-induced effects on the QV relationship suggests that around 60% of the chemical energy stored in the ΔpH controls the conformation of the S4 voltage sensor segment (Carmona *et al.*, 2021). Taken together, the ΔpH sensitivity of gating currents suggests that the S4 conformation depends on ΔpH, which agrees with my results (Fig. 3.11, 3.12, 3.17). As a change in ΔpH alters the conformation of the S4 segment, independently of the membrane side of pH change (compare Fig. 3.11 and 3.12), my data are consistent with the idea that a low pH_i or a positive membrane potential push S4 to the

extracellular side; a low pH_o or a negative membrane potential push S4 to the intracellular side (Fig. 3.14). Therefore, I suggest that both ΔpH and voltage determine the position of S4 in the membrane. Here, PCF experiments provide evidence that S4 conformation can be changed by pH_i in the resting state (Fig. 3.11, 3.12, 3.17) and proton uncaging showed that the open state is sensitive to changes in pH_o (Fig. 3.15). In a previous study of human Hv1, mutation of the first of the three arginine residues of the S4 segment to histidine („R1H") creates an additional, hyperpolarization-activated proton conductance, termed shuttle conductance (Randolph *et al.*, 2016). The shuttle conductance was pH_o-sensitive, which might reflect the ΔpH sensitivity of the S4 segment for conformational changes between different resting (non-open) states at negative membrane potentials.

Different molecular mechanisms of ΔpH sensing are debated (Islas, 2018). Protonation and deprotonation of amino-acid residues can induce conformational changes in proteins. In Hv1, there might be distinct amino-acid residues on the extracellular and intracellular sites of the membrane, serving as pH sensors for detecting pH_o and pH_i, respectively (Cherny *et al.*, 1995). S4 contains three arginine residues as potentially titratable amino-acid side chains. Because these residues account for almost all of the gating charges in Hv1 and confer voltage sensitivity to the channel (Gonzalez *et al.*, 2013), deprotonation of any of the three arginine residues should result in a significant decrease of voltage sensitivity that should result in shallower slopes of the GVs. I, therefore, expect shallower slopes of the GVs at pH_i = 7.0 or 7.5 compared to the GVs at pH_i = 6.5, for both conditions, i.e., in symmetric pH (pH_o = pH_i) or in ΔpH (keeping pH_o = 7.0). However, these arginine residues, because of their high pKa values, might be difficult to deprotonate under physiological conditions. In line with this assumption, GV slopes at different pH values did not change significantly (Appendix Table 14). Alternatively, the negatively charged amino-acid residues in helices S1 - S3, which serve as counter charges of the arginine residues on S4, might participate in pH sensing (DeCoursey, 2018); titration of those residues might weaken their interaction with the arginine residues and, therefore, affect the S4 position in the electrical field. However, the titration of counter charges should depend on the pH itself rather than ΔpH. Moreover, the strict dependence of $V_{1/2}$ on ΔpH (~ –40 mV/ΔpH) holds for a large ΔpH range (at least 3 pH units) (Ramsey *et al.*, 2010). Because Hv1 senses the ΔpH and not the pH itself, an increase of pH on one side or a decrease of pH on the other side of the membrane, resulting in

the same ΔpH, should trigger the same structural and functional changes in the channel. Thus, if titration of counter charges was the underlying molecular mechanism for ΔpH sensing, protonation of an amino-acid residue at decreased pH on one side of the membrane or deprotonation of an amino-acid residue at increased pH on the other side of the membrane should result in the same functional consequences. Furthermore, the sensitivity to ΔpH over a large pH range would need to involve several different titratable amino acids on both sides of the membrane, with different pK_a values that together cover the pH range. However, the need for several different titratable amino acids for ΔpH sensing in such a model suggests that ΔpH sensing might be abrogated or changed by mutation of single titratable amino acids. On the contrary, mutation of candidate amino acids could not abrogate ΔpH sensing (Ramsey *et al.*, 2010). As an alternative to de- or protonation, it has been suggested that water molecules could be an important component in mediating ΔpH sensitivity. Molecular dynamics simulations suggest that the core of the VSD of Hv1 contains more water molecules than the VSD of classical voltage-gated ion channels (Ramsey *et al.*, 2010). Indeed, several water accessible amino-acid residues are located deep inside the crevice of the Hv1 VSD (Kurokawa & Okamura, 2014; Mony *et al.*, 2015). The water molecules might form a water network with limited mobility within the VSD. Protonation of this network could lead to a rearrangement of the hydrogen bonding between water molecules and amino acids and exert electrostatic forces that change S4 conformation (Ramsey *et al.*, 2010). Such a mechanism is hard to localize to the Hv1 channel itself; it would amount to a distributed effect acting on the channel. A previous study on Zn^{2+} sensitivity in Hv1 provides evidence for allosteric coupling between intra- and extracellular residues induced through coulombic interactions (De La Rosa *et al.*, 2018). This supports the idea that changes in electrostatic forces might propagate over a long distance across the membrane.

In addition to changes in S4, an S1 conformational change, which is concomitant to the opening of Hv1, has been identified (Mony *et al.*, 2015). Interestingly, I did not find evidence for direct ΔpH-induced conformational changes of the S1 segment (Fig. 3.13), reinforcing the idea that the mechanisms of ΔpH- and voltage-sensing occur via the S4 voltage sensor. However, I cannot rule out the possibility that the S4 segment is coupled to unknown ΔpH-sensing elements.

Therefore, further studies are needed to characterize the ΔpH-induced conformational changes of the S4 segment as well as putative conformational changes involving other segments.

The data in this thesis suggest that the entire S4 segment serves as the "ΔpH-sensing element". In this model, the electrochemical potential for protons across the membrane, together with the membrane potential, determines the position of S4 in the membrane (Fig. 3.14B), and thus sets the voltage of half maximal channel activation. Of note, the ΔpH-induced shift of $V_{1/2}$, (–40 mV/ΔpH in the literature and –47 to –57 mV/ΔpH here), is intriguingly close to the electrochemical potential for protons (59 mV/ΔpH unit). Deviations from the electrochemical potential for protons might arise from differences between proton concentration and activity. Mutations that limit water exposure to S4 should decrease ΔpH sensing. Clearly, the identification of the mechanism behind ΔpH sensing of Hv1 requires future studies using electrophysiological and fluorometric techniques on mutants of Hv1 as well as modeling approaches that take the membrane potential and the electrochemical potential for protons into consideration.

4.3. pH_o sensing in the VSD of ciVSP

The S4-voltage sensor of Hv1 moves when ΔpH is changed, even when the channel is closed (Fig. 3.11, 3.12, 3.17). Therefore, proton conduction does not seem to be a prerequisite for ΔpH sensing. VSDs with an S4 segment also exist in other VGICs and voltage-dependent enzymes such as the voltage-sensitive phosphatase (VSP). It is not known whether VSDs of other voltage-sensitive proteins are ΔpH sensitive. I therefore tested in PCF experiments, whether the S4 segment of the VSD of ciVSP depends on pH_o, pH_i, or ΔpH.

A decrease in pH_o that introduced a ΔpH = –0.5 altered the voltage-driven S4 conformational change (Fig. 3.20), suggesting that the S4 segment in the VSD of ciVSP is either sensitive to pH_o. If the VSD of ciVSP was also sensitive to the ΔpH, an increase in pH_i that also introduces a ΔpH = –0.5 should similarly alter the voltage-driven S4 conformational change. However, changes in pH_i did not alter the voltage-driven S4 conformational change (Fig. 3.19). In previous work with a chimera consisting of the VSD of ciVSP and a potassium-channel pore, changes in pH_i did not change voltage-dependent gating of the pore (Rosasco *et al.*, 2015), which is in line with the results of my experiments. In my thesis, I show that the voltage-driven S4 conformational change in the VSD of ciVSP only depends on pH_o but not on pH_i, suggesting that the VSD of ciVSP senses the pH_o itself rather than the ΔpH like Hv1. Thus, not every VSD-containing protein has a ΔpH-sensitive S4 segment; instead, ΔpH sensing might be specific to Hv1. Of note, neither pH_o nor pH_i changed the S4 resting-state conformation in ciVSP, which was, however, the case in Hv1. This indicates that the pH_o sensing in the VSD of ciVSP might rely on a different molecular mechanism than ΔpH sensing in Hv1.

Here, I provide evidence that the S4-voltage sensor of ciVSP is sensitive to pH_o (Fig. 3.20). Villalba-Galea and others (2013), however, showed that sensing currents, which correspond to the gating currents in ion channels, were not pH_o-sensitive in ciVSP (Villalba-Galea *et al.*, 2013). Because the S4 segment contains the majority of sensing charges in ciVSP (Villalba-Galea *et al.*, 2013), sensing currents report on electrical visible conformational changes of the S4 segment. Thus, the pH_o-dependent component in my PCF recordings might rather report on electrically-

silent, S4 conformational changes. The molecular mechanism for pH_o sensing in the VSD of ciVSP remains obscure. Villalba-Galea and others (2008) identified an electrically-silent conformational change that transfers the VSD from the active state to a more stable state, the so-called relaxed state, correlating with changes in voltage dependence. Future experiments are needed to identify the molecular mechanism underlying pH_o sensing in the VSD of ciVSP.

In the proton-activated chloride channel PAC, pH_o is sensed by polar amino acids on the extracellular side and involves protonation of a histidine residue (Ruan *et al.*, 2020). The VSD of ciVSP lacks extracellular histidine residues (Li *et al.*, 2014), excluding such a mechanism. However, three negatively charged amino-acid residues, namely D129 on S1 and D186 and E183 on S3 (Li *et al.*, 2014), constitute the counter charges, which interact electrostatically with the arginine residues on S4. pH_o-dependent protonation of e.g., the more extracellularly located residue D129 might weaken the interaction with its electrostatic partner R226 in the open state and, therefore, influence voltage-driven S4 conformational changes.

Of note, it remains an open question whether the actual enzyme function, the phosphatase activity, also depends on pH_o. Heterologously expressed ciVSP directly translates changes in membrane potential into turnover of phosphoinositides (Murata *et al.*, 2005). It has been suggested that different conformational states in the VSD might correlate to different active states with different substrate preferences (Grimm & Isacoff, 2016). A speculative idea is that the pH_o sensitivity of the ciVSP-VSD might couple pH_o to the substrate preference of the enzyme. CiVSP is expressed in blood cells (Ogasawara *et al.*, 2011), gut epithelium (Ogasawara *et al.*, 2011), nervous system (Murata *et al.*, 2005), and sperm tail (Murata *et al.*, 2005). However, the physiological role of VSP in *Ciona intestinalis* is not understood. CiVSP might be involved e.g., in the control of sperm by coupling changes in pH_o to sperm motility during spawning into the sea water. A recent study suggested that VSP in mouse sperm is involved in the control of sperm motility (Kawai *et al.*, 2019).

5. Appendix

Channel	I_{post}/I_{pre}	n
WT	0.9 ± 0.1	10
H150C-I262C	0.7 ± 0.2	4
H150C-N264C	0.8 ± 0.1	3
V151C-I262C	0.8 ± 0.1	4
V151C-N264C	0.75 ± 0.1	4
I153C-I262C	0.5 ± 0.2	4
I153C-N264C	0.9 ± 0.3	2
I154C-I262C	0.5 ± 0.4	10
I154C-N264C	1.0 ± 0.2	3
V157C-I262C	0.6 ± 0.3	4
V157C-N264C	0.7 ± 0.1	4

Table 11. Current ratios, after and before H_2O_2 incubation, of ciHv1 cysteine double mutants and WT.

Channel	Segments	I_{post}/I_{pre}	Calculated residual current	p(cal)	Distance Cα-Cα	n
WT	-	0.9 ± 0.1	-	-	-	5
H150C	S1	0.4 ± 0.1	-	-	-	5
V151C	S1	0.93 ± 0.1	-	-	-	5
I153C	S1	0.35 ± 0.04	-	-	-	6
I154C	S1	0.8 ± 0.07	-	-	-	4
V157C	S1	0.9 ± 0.02	-	-	-	3
I262C	S4	0.26 ± 0.05	-	-	-	7
N264C	S4	0.26 ± 0.05	-	-	-	4
H150C-I262C	S1-S4	0.5 ± 0.16	0	0.005	9.2	4
H150C-N264C	S1-S4	0.2 ± 0.1	0	0.02	13.3	4
V151C-I262C	S1-S4	0.07 ± 0.04	0.185	0.00002	10.3	9
V151S-I262C	S1-S4	0.43 ± 0.14	-	-	10.3	10
V151C-N264C	S1-S4	0.3 ± 0.1	0.186	0.15	14.1	3
I153C-I262C	S1-S4	0.04 ± 0.01	0	0.01	9.3	3
I153C-N264C	S1-S4	0.07 ± 0.025	0	0.02	14.4	3
I154C-I262C	S1-S4	0.12 ± 0.03	0.08	0.05	7.7	3
I154C-N264C	S1-S4	0.1 ± 0.06	0.08	0.2	12.2	4
V157C-I262C	S1-S4	0.12 ± 0.02	0.13	0.2	9.7	3
V157C-N264C	S1-S4	0.13 ± 0.03	0.13	0.5	14.3	3

Table 12. **MTS-1-MTS block effect and distances between Cα atoms of the respective cysteines.** Cysteines on the same segment were not combined in a cysteine-double mutant. One-way ANOVA for I_{post}/I_{pre}, $p < 0.00001$, *post-hoc* comparison of mutant to WT, $p \leq 0.00001$, n.s. for WT vs. V151C, I154C, and V157C. p(cal) indicates the result of the statistical comparison of mutant I_{post}/I_{pre} to calculated (theoretical) I_{post}/I_{pre} (see Methods 2.5) for the same mutant by two-tailed Student´s t-test. Distances are based on the homology model of ciHv1 and therefore reflect presumably closed-state conformation. Distances were measured using Pymol and are given in Å.

Channel	I_{post}/I_{pre}	p(I)	F_{signal}(post)/ F_{signal}(pre)	p(F_{signal})	F-80 mV (post)/F-80 mV (pre)	p(F-80 mV)	n
I175C*	0.93 ± 0.07	-	0.8 ± 0.3	-	0.97 ± 0.07	-	4
V151C-I175C*	0.94 ± 0.06	0.99	0.7 ± 0.1	0.86	0.94 ± 0.05	0.87	4
I262C-I175C*	0.41 ± 0.15	0.00003	0.5 ± 0.1	0.06	0.95 ± 0.04	0.97	5
V151C-I262C-I175C*	0.2 ± 0.1	0.000001	0.2 ± 0.1	0.0002	0.82 ± 0.05	0.005	4-5

Table 13. Mean current and fluorescence ratios after and before MTS-1-MTS incubation in different labeled ciHv1 mutants. One-way ANOVA for I_{post}/I_{pre}, $p = 0.0000002$; p(I) indicates the significance level of *post-hoc* comparison of I_{post}/I_{pre} in mutant to I175C*. One-way ANOVA for F_{signal} (post) / F_{signal} (pre) $p = 0.0001$; p(F_{signal}) indicates the significance level of *post-hoc* comparison of F_{signal} (post) / F_{signal} (pre) in mutant to I175C*. One-way ANOVA for F-80 mV (post) / F-80 mV (pre), $p = 0.003$; p(F-80 mV) indicates the significance level of *post-hoc* comparison of F-80 mV (post) / F-80 mV (pre) in mutant to I175C*. * indicates cysteine is labeled with TAMRA.

Channel	$V_{1/2}$ shift/ Δ pH unit (mV)	pH_i/pH_o	$V_{1/2}$ (mV)	Slope (mV)	n
WT	–48.6 ± 9.5	6.5/7.0	–8.2 ± 10.7	9.8 ± 2.5	16
		7.0/7.0	17.5 ± 8.0	9.2 ± 3.0	17
		7.5/7.0	39.9 ± 9.0	8.1 ± 3.3	16
		6.5/6.5	24.2 ± 7.1	9.4 ± 2.4	6
		7.5/7.5	15.1 ± 9.6	10.8 ± 1.8	5
L245C-TAMRA	–54.1 ± 4.8	6.5/7.0	–50.5 ± 9.5	7.6 ± 1.9	5
		7.0/7.0	–27.0 ± 12.2	7.4 ± 2.1	8
		7.5/7.0	–2.5 ± 13.7	6.9 ± 2.2	7

Table 14. Fit parameters of the GV relationships of ciHv1-WT and ciHv1-L245C-TAMRA. Statistical comparison of inside-out mutant slope to the respective WT slope at the same ΔpH

condition with Student´s-t-test: p(L245C-TAMRA, pH_i 6.5/ pH_o 7.0) = 0.06, p(L245C-TAMRA, pH_i 7.0/ pH_o 7.0) = 0.3, p(L245C-TAMRA, pH_i 7.5/ pH_o 7.0) = 0.42.

pH_i/pH_o	τ_{fast} (s)	τ_{slow} (s)	n
6.5/7.0	0.16 ± 0.08	0.54 ± 0.44	7
7.0/7.0	0.87 ± 0.69	1.28 ± 0.55	9
7.5/7.0	1.03 ± 0.63	1.58 ± 0.52	6
6.5/6.5	0.49 ± 0.23	0.71 ± 0.36	9
7.5/7.5	1.19 ± 0.83	1.85 ± 1.08	5

Table 15. Activation kinetics (τ_{fast} and τ_{slow}) of the current of ciHv1 WT during a voltage step to 40 mV at different pH_i and pH_o.

pH_i/pH_o	Voltage	τ_{fast} (s)	τ_{slow} (s)	τ_{deact} (s)	n
6.5/6.5	–40 mV	0.77 ± 0.69	1.61 ± 0.56	1.28 ± 0.48	5
	+40 mV	0.09 ± 0.02	0.38 ± 0.26	0.97 ± 0.21	3
7.0/7.0	–40 mV	1.04 ± 1.22	2.67 ± 1.83	1.22 ± 0.59	9
	+40 mV	0.11 ± 0.03	0.89 ± 0.25	1.16 ± 0.78	4
7.5/7.5	–40 mV	2.48 ± 2.37	3.45 ± 2.32	1.35 ± 0.47	9
	+40 mV	0.33 ± 0.13	2.34 ± 1.53	1.62 ± 0.28	4

Table 16. Activation (τ_{fast}, τ_{slow}) and deactivation (τ_{deact}) kinetics of the F_{signal} of ciHv1-L245C-TAMRA during a voltage step to –40 or +40 mV at different symmetric pH (ΔpH = 0).

pH_i/pH_o	$\tau_{I\ fast}$ (s)	$\tau_{F\ fast}$ (s)	$\tau_{I\ slow}$ (s)	$\tau_{F\ slow}$ (s)	n
6.5/7.0	0.05 ± 0.02	0.05 ± 0.01	0.23 ± 0.14	0.44 ± 0.21	4
7.0/7.0	0.17 ± 0.12	0.15 ± 0.15	0.7 ± 0.3	0.47 ± 0.13	4
7.5/7.5	0.2 ± 0.1	0.23 ± 0.16	0.9 ± 0.5	1.5 ± 0.5	4

Table 17. Activation kinetics of the current and F_{Signal} of ciHv1-I175C-TAMRA recorded at pH_o = 7.0.

Configuration		ΔpH = -0.5	ΔpH = 0	ΔpH = 0.5	n
inside-out	τ_{fast}	0.2 ± 0.1	0.6 ± 0.3	0.3 ± 0.2	4
	τ_{slow}	1.8 ± 2.1	1.3 ± 0.8	0.6 ± 0.2	4
outside-out	τ_{fast}	2.0 ± 2.8	0.2 ± 0.1	0.6 ± 1.2	3-5
	τ_{slow}	3.4 ± 3.0	2.4 ± 1.4	0.7 ± 1.0	3-5

Table 18. Activation kinetics of F_{Signal} of ciVSP-G214C-TAMRA recorded at different ΔpH, keeping pH_o = 7.0 in outside-out recordings and pH_i =7.0 in inside-out recordings.

6. References

Abbruzzetti S, Sottini S, Viappiani C & Corrie JET (2005). Kinetics of proton release after flash photolysis of 1-(2-nitrophenyl)ethyl sulfate (caged sulfate) in aqueous solution. *J Am Chem Soc* **127**, 9865–9874.

Aggarwal SK & MacKinnon R (1996). Contribution of the S4 segment to gating charge in the Shaker K^+ channel. *Neuron* **16**, 1169–1177.

Barth A & Corrie JET (2002). Characterization of a new caged proton capable of inducing large pH jumps. *Biophys J* **83**, 2864–2871.

Bayrhuber M, Maslennikov I, Kwiatkowski W, Sobol A, Wierschem C, Eichmann C, Frey L & Riek R (2019). Nuclear Magnetic Resonance Solution Structure and Functional Behavior of the Human Proton Channel. *Biochemistry* **58**, 4017–4027.

Bennett AL & Ramsey IS (2017*a*). Rebuttal from Ashley L. Bennett and Ian Scott Ramsey. *J Physiol* **595**, 6803.

Bennett AL & Ramsey IS (2017*b*). CrossTalk opposing view: proton transfer in Hv1 utilizes a water wire, and does not require transient protonation of a conserved aspartate in the S1 transmembrane helix. *J Physiol* **595**, 6797–6799.

Berger TK, Fußhöller DM, Goodwin N, Bönigk W, Müller A, Dokani Khesroshahi N, Brenker C, Wachten D, Krause E, Kaupp UB & Strünker T (2017). Post-translational cleavage of Hv1 in human sperm tunes pH- and voltage-dependent gating. *J Physiol* **595**, 1533–1546.

Berger TK & Isacoff EY (2011). The pore of the voltage-gated proton channel. *Neuron* **72**, 991–1000.

Berger TK & Isacoff EY (2015). Fluorescent labeling for patch-clamp fluorometry (PCF) measurements of real-time protein motion in ion channels. *Methods Mol Biol* **1266**, 93–106.

Capasso M, Bhamrah MK, Henley T, Boyd RS, Langlais C, Cain K, Dinsdale D, Pulford K, Khan M, Musset B, Cherny VV, Morgan D, Gascoyne RD, Vigorito E, DeCoursey TE, MacLennan ICM & Dyer MJS (2010). HVCN1 modulates BCR signal strength via regulation of BCR-dependent generation of reactive oxygen species. *Nat Immunol* **11**, 265–272.

Carmona EM, Fernandez M, Alvear-Arias JJ, Neely A, Larsson HP, Alvarez O, Garate JA, Latorre R & Gonzalez C (2021). The voltage sensor is responsible for ΔpH dependence in Hv1 channels. *Proc Natl Acad Sci USA* **118**, 1–7.

Carmona EM, Larsson HP, Neely A, Alvarez O, Latorre R & Gonzalez C (2018). Gating charge displacement in a monomeric voltage-gated proton (Hv1) channel. *Proc Natl Acad Sci USA* **115**, 9240–9245.

Cha A & Bezanilla F (1997). Characterizing Voltage-Dependent Conformational Changes in the Shaker K^+ Channel with Fluorescence. *Neuron* **19**, 1127–1140.

El Chemaly A, Okochi Y, Sasaki M, Arnaudeau S, Okamura Y & Demaurex N (2010). VSOP/Hv1 proton channels sustain calcium entry, neutrophil migration, and superoxide production by limiting cell depolarization and acidification. *J Exp Med* **207**, 129–139.

Cherny VV, Morgan D, Musset B, Chaves G, Smith SME & DeCoursey TE (2015). Tryptophan 207 is crucial to the unique properties of the human voltage-gated proton channel, hHv1. *J Gen Physiol* **146**, 343–356.

Cherny VV, Morgan D, Thomas S, Smith SME & DeCoursey TE (2018). Histidine168 is crucial for ΔpH-dependent gating of the human voltage-gated proton channel, hHv1. *J Gen Physiol* **150**, 851–862.

Cherny VV, Markin VS & DeCoursey TE (1995). The voltage-activated hydrogen ion conductance in rat alveolar epithelial cells is determined by the pH gradient. *J Gen Physiol* **105**, 861–896.

De-la-Rosa V, Suárez-Delgado E, Rangel-Yescas GE & Islas LD (2016). Currents through Hv1 channels deplete protons in their vicinity. *J Gen Physiol* **147**, 127–136.

De La Rosa V, Bennett AL & Ramsey IS (2018). Coupling between an electrostatic network and the Zn^{2+} binding site modulates Hv1 activation. *J Gen Physiol* **150**, 863–881.

De La Rosa V & Ramsey IS (2018). Gating Currents in the Hv1 Proton Channel. *Biophys J* **114**, 2844–2854.

DeCaen PG, Yarov-Yarovoy V, Zhao Y, Scheuer T & Catterall WA (2008). Disulfide locking a sodium channel voltage sensor reveals ion pair formation during activation. *Proc Natl Acad Sci USA* **105**, 15142–15147.

DeCoursey TE (2003). Voltage-Gated Proton Channels and Other Proton Transfer Pathways. *Physiol Rev* **83**, 475–579.

DeCoursey TE (2013). Voltage-Gated Proton Channels: Molecular Biology, Physiology, and Pathophysiology of the Hv Family. *Physiol Rev* **93**, 599–652.

DeCoursey TE (2017*a*). Rebuttal from Thomas E. DeCoursey. *J Physiol* **595**, 6801.

DeCoursey TE (2017*b*). CrossTalk proposal: Proton permeation through HV1 requires transient protonation of a conserved aspartate in the S1 transmembrane helix. *J Physiol* **595**, 6793–6795.

DeCoursey TE (2018). Voltage and pH sensing by the voltage-gated proton channel, Hv1. *J R Soc Interface* **15**, 20180108.

Fujiwara Y, Kurokawa T & Okamura Y (2014). Long α helices projecting from the membrane as the dimer interface in the voltage-gated H^+ channel. *J Gen Physiol* **143**, 377–386.

Fujiwara Y, Kurokawa T, Takeshita K, Kobayashi M, Okochi Y, Nakagawa A & Okamura Y (2012). The cytoplasmic coiled-coil mediates cooperative gating temperature sensitivity in the voltage-gated H^+ channel Hv1. *Nat Commun* **3**, 816.

Geißler D, Antonenko YN, Schmidt R, Keller S, Krylova OO, Wiesner B, Bendig J, Pohl P & Hagen V (2005). (Coumarin-4-yl)methyl esters as highly efficient, ultrafast phototriggers for protons

and their application to acidifying membrane surfaces. *Angew Chemie - Int Ed* **44**, 1195–1198.

Geragotelis AD, Wood ML, Göddeke H, Hong L, Webster PD, Wong EK, Freites JA, Tombola F & Tobias DJ (2020). Voltage-dependent structural models of the human Hv1 proton channel from long-timescale molecular dynamics simulations. *Proc Natl Acad Sci USA* **117**, 13490–13498.

Gonzalez C, Koch HP, Drum BM & Larsson HP (2010). Strong cooperativity between subunits in voltage-gated proton channels. *Nat Struct Mol Biol* **17**, 51–57.

Gonzalez C, Rebolledo S, Perez ME & Larsson HP (2013). Molecular mechanism of voltage sensing in voltage-gated proton channels. *J Gen Physiol* **141**, 275–285.

Green NS, Reisler E & Houk KN (2001). Quantitative evaluation of the lengths of homobifunctional protein cross-linking reagents used as molecular rulers. *Protein Sci* **10**, 1293–1304.

Grimm SS & Isacoff EY (2016). Allosteric substrate switching in a voltage-sensing lipid phosphatase. *Nat Chem Biol* **12**, 261–267.

Hamill OP, Marty A, Neher E, Sakmann B & Sigworth FJ (1981). Improved patch-clamp techniques for high-resolution current recording from cells and cell-free membrane patches. *Pflügers Arch Eur J Physiol* **391**, 85–100.

Hamill OP & Sakmann B (1981). A cell-free method for recording single-channel currents from biological membranes. *J Physiol* **312**, 41–42.

Hille B (2001). *Ion channels of excitable membranes*, 3rd. edn. Sinauer Associates, INC. Sunderland, Massachusetts.

Hondares E, Brown MA, Musset B, Morgan D, Cherny VV, Taubert C, Bhamrah MK, Coe D, Marelli-Berg F, Gribben JG, Dyer MJS, DeCoursey TE & Capasso M (2014). Enhanced activation of an amino-terminally truncated isoform of the voltage-gated proton channel HVCN1 enriched in malignant B cells. *Proc Natl Acad Sci USA* **111**, 18078–18083.

Hong L, Pathak MM, Kim IH, Ta D & Tombola F (2013). Voltage-Sensing Domain of Voltage-Gated Proton Channel Hv1 Shares Mechanism of Block with Pore Domains. *Neuron* **77**, 274–287.

Iovannisci D, Illek B & Fischer H (2010). Function of the HVCN1 proton channel in airway epithelia and a naturally occurring mutation, M91T. *J Gen Physiol* **136**, 35–46.

Islas LD (2018). The acid test for pH-dependent gating in cloned HV1 channels. *J Gen Physiol* **150**, 781–782.

Kawai T, Miyata H, Nakanishi H, Sakata S, Morioka S, Sasaki J, Watanabe M, Sakimura K, Fujimoto T, Sasaki T, Ikawa M & Okamura Y (2019). Polarized PtdIns(4,5)P 2 distribution mediated by a voltage-sensing phosphatase (VSP) regulates sperm motility. *Proc Natl Acad Sci USA* **116**, 26020–26028.

Koch HP, Kurokawa T, Okochi Y, Sasaki M, Okamura Y & Larsson HP (2008). Multimeric nature of voltage-gated proton channels. *Proc Natl Acad Sci USA* **105**, 9111–9116.

Kohout SC, Ulbrich MH, Bell SC & Isacoff EY (2008). Subunit organization and functional transitions in Ci-VSP. *Nat Struct Mol Biol* **15**, 106–108.

Kurokawa T & Okamura Y (2014). Mapping of sites facing aqueous environment of voltage-gated proton channel at resting state: A study with PEGylation protection. *Biochim Biophys Acta - Biomembr* **1838**, 382–387.

Lakowicz JR (2006). *Principles of Fluorescence Spectroscopy*, 3rd edn. Lakowicz JR. Springer US, Boston, MA.

Lapointe J-Y & Szabo G (1987). A novel holder allowing internal perfusion of patch-clamp pipettes. *Pflügers Arch Eur J Physiol* **410**, 212–216.

Larsson HP (2020). Zn^{2+} to probe voltage-gated proton (Hv1) channels. **152**, 2–5.

Larsson HP & Elinder F (2000). A conserved glutamate is important for slow inactivation in K^+ channels. *Neuron* **27**, 573–583.

Lee S-Y, Letts JA & MacKinnon R (2008). Dimeric subunit stoichiometry of the human voltage-dependent proton channel Hv1. *Proc Natl Acad Sci USA* **105**, 7692–7695.

Lee S-Y, Letts JA & MacKinnon R (2009). Functional Reconstitution of Purified Human Hv1 H^+ Channels. *J Mol Biol* **387**, 1055–1060.

Lenaeus MJ, Gamal El-Din TM, Ing C, Ramanadane K, Pomès R, Zheng N & Catterall WA (2017). Structures of closed and open states of a voltage-gated sodium channel. *Proc Natl Acad Sci USA* **114**, E3051–E3060.

Li Q, Wanderling S, Paduch M, Medovoy D, Singharoy A, McGreevy R, Villalba-Galea CA, Hulse RE, Roux B, Schulten K, Kossiakoff A & Perozo E (2014). Structural mechanism of voltage-dependent gating in an isolated voltage-sensing domain. *Nat Struct Mol Biol* **21**, 244–252.

Lishko P V., Botchkina IL, Fedorenko A & Kirichok Y (2010). Acid Extrusion from Human Spermatozoa Is Mediated by Flagellar Voltage-Gated Proton Channel. *Cell* **140**, 327–337.

Loo TW & Clarke DM (2001). Determining the Dimensions of the Drug-binding Domain of Human P-glycoprotein Using Thiol Cross-linking Compounds as Molecular Rulers. *J Biol Chem* **276**, 36877–36880.

Maingret F, Patel AJ, Lesage F, Lazdunski M & Honoré E (1999). Mechano- or acid stimulation, two interactive modes of activation of the TREK-1 potassium channel. *J Biol Chem* **274**, 26691–26696.

Mannuzzu LM, Moronne MM & Isacoff EY (1996). Direct physical measure of conformational rearrangement underlying potassium channel gating. *Science* **271**, 213–216.

Mony L, Berger TK & Isacoff EY (2015). A specialized molecular motion opens the Hv1 voltage-gated proton channel. *Nat Struct Mol Biol* **22**, 283–290.

Mony L, Stroebel D & Isacoff EY (2020). Dimer interaction in the Hv1 proton channel. *Proc Natl Acad Sci USA* **117**, 20898–20907.

Morgan D, Capasso M, Musset B, Cherny VV, Rios E, Dyer MJS & DeCoursey TE (2009). Voltage-gated proton channels maintain pH in human neutrophils during phagocytosis. *Proc Natl Acad Sci USA* **106**, 18022–18027.

Murata Y, Iwasaki H, Sasaki M, Inaba K & Okamura Y (2005). Phosphoinositide phosphatase activity coupled to an intrinsic voltage sensor. *Nature* **435**, 1239–1243.

Musset B, Cherny VV, Morgan D, Okamura Y, Ramsey IS, Clapham DE & DeCoursey TE (2008). Detailed comparison of expressed and native voltage-gated proton channel currents. *J Physiol* **586**, 2477–2486.

Musset B, Smith SME, Rajan S, Morgan D, Cherny VV & DeCoursey TE (2011). Aspartate 112 is the selectivity filter of the human voltage-gated proton channel. *Nature* **480**, 273–277.

Neher E & Sakmann B (1976). Single-channel currents recorded from membrane of denervated frog muscle fibres. *Nature* **260**, 799–802.

Noda M, Shimizu S, Tanabe T, Takai T, Kayano T, Ikeda T, Takahashi H, Nakayama H, Kanaoka Y, Minamino N, Kangawa K, Matsuo H, Raftery MA, Hirose T, Inayama S, Hayashida H, Miyata T & Numa S (1984). Primary structure of Electrophorus electricus sodium channel deduced from cDNA sequence. *Nature* **312**, 121–127.

Ogasawara M, Sasaki M, Nakazawa N, Nishino A & Okamura Y (2011). Gene expression profile of Ci-VSP in juveniles and adult blood cells of ascidian. *Gene Expr Patterns* **11**, 233–238.

Payandeh J, Scheuer T, Zheng N & Catterall WA (2011). The crystal structure of a voltage-gated sodium channel. *Nature* **475**, 353–359.

Qiu F, Chamberlin A, Watkins BM, Ionescu A, Perez ME, Barro-Soria R, González C, Noskov SY & Larsson HP (2016). Molecular mechanism of Zn^{2+} inhibition of a voltage-gated proton channel. *Proc Natl Acad Sci USA* **113**, E5962–E5971.

Qiu F, Rebolledo S, Gonzalez C & Larsson HP (2013). Subunit Interactions during Cooperative Opening of Voltage-Gated Proton Channels. *Neuron* **77**, 288–298.

Ramsey IS, Mokrab Y, Carvacho I, Sands ZA, Sansom MSP & Clapham DE (2010). An aqueous H^+ permeation pathway in the voltage-gated proton channel Hv1. *Nat Struct Mol Biol* **17**, 869–875.

Ramsey IS, Moran MM, Chong JA & Clapham DE (2006). A voltage-gated proton-selective channel lacking the pore domain. *Nature* **440**, 1213–1216.

Ramsey IS, Ruchti E, Kaczmarek JS & Clapham DE (2009). Hv1 proton channels are required for high-level NADPH oxidase-dependent superoxide production during the phagocyte respiratory burst. *Proc Natl Acad Sci USA* **106**, 7642–7647.

Randolph AL, Mokrab Y, Bennett AL, Sansom MSP & Ramsey IS (2016). Proton currents constrain structural models of voltage sensor activation. *Elife* **5**, 1–29.

Rodriguez JD, Haq S, Bachvaroff T, Nowak KF, Nowak SJ, Morgan D, Cherny VV, Sapp MM, Bernstein S, Bolt A, DeCoursey TE, Place AR & Smith SME (2017). Identification of a vacuolar proton channel that triggers the bioluminescent flash in dinoflagellates ed. Sokolowski B. *PLoS One* **12**, e0171594.

Rosasco MG, Gordon SE & Bajjalieh SM (2015). Characterization of the Functional Domains of a Mammalian Voltage-Sensitive Phosphatase. *Biophys J* **109**, 2480–2491.

Ruan Z, Osei-Owusu J, Du J, Qiu Z & Lü W (2020). Structures and pH-sensing mechanism of the proton-activated chloride channel. *Nature* **588**, 350–354.

Sandoz G, Douguet D, Chatelain F, Lazdunski M & Lesage F (2009). Extracellular acidification exerts opposite actions on TREK1 and TREK2 potassium channels via a single conserved histidine residue. *Proc Natl Acad Sci USA* **106**, 14628–14633.

Sasaki M, Takagi M & Okamura Y (2006). A voltage sensor-domain protein is a voltage-gated proton channel. *Science* **312**, 589–592.

Seoh SA, Sigg D, Papazian DM & Bezanilla F (1996). Voltage-sensing residues in the S2 and S4 segments of the Shaker K^+ channel. *Neuron* **16**, 1159–1167.

Sigworth FJ & Neher E (1980). Single Na^+ channel currents observed in cultured rat muscle cells. **287**, 447–449.

Smith SME, Morgan D, Musset B, Cherny VV, Place AR, Hastings JW & DeCoursey TE (2011). Voltage-gated proton channel in a dinoflagellate. *Proc Natl Acad Sci USA* **108**, 18162–18167.

Starace DM, Stefani E & Bezanilla F (1997). Voltage-Dependent Proton Transport by the Voltage Sensor of the Shaker K^+ Channel. *Neuron* **19**, 1319–1327.

Takeshita K, Sakata S, Yamashita E, Fujiwara Y, Kawanabe A, Kurokawa T, Okochi Y, Matsuda M, Narita H, Okamura Y & Nakagawa A (2014). X-ray crystal structure of voltage-gated proton channel. *Nat Struct Mol Biol* **21**, 352–357.

Tanabe T, Takeshima H, Mikami A, Flockerzi V, Takahashi H, Kangawa K, Kojima M, Matsuo H, Hirose T & Numa S (1987). Primary structure of the receptor for calcium channel blockers from skeletal muscle. *Nature* **328**, 313–318.

Taylor AR, Chrachri A, Wheeler G, Goddard H & Brownlee C (2011). A voltage-gated H^+ channel underlying pH homeostasis in calcifying Coccolithophores. *PLoS Biol* **9**, 1–14.

Tempel BL, Papazian DM, Schwarz TL, Jan YN & Jan LY (1987). Sequence of a probable potassium channel component encoded at Shaker locus of Drosophila. *Science* **237**, 770–775.

Tombola F, Ulbrich MH & Isacoff EY (2008). The Voltage-Gated Proton Channel Hv1 Has Two Pores, Each Controlled by One Voltage Sensor. *Neuron* **58**, 546–556.

Tombola F, Ulbrich MH, Kohout SC & Isacoff EY (2010). The opening of the two pores of the Hv1 voltage-gated proton channel is tuned by cooperativity. *Nat Struct Mol Biol* **17**, 44–52.

Villalba-Galea CA (2014). Hv1 proton channel opening is preceded by a voltage-independent

transition. *Biophys J* **107**, 1564–1572.

Villalba-Galea CA, Frezza L, Sandtner W & Bezanilla F (2013). Sensing charges of the Ciona intestinalis voltage-sensing phosphatase. *J Gen Physiol* **142**, 543–555.

Villalba-Galea CA, Sandtner W, Starace DM & Bezanilla F (2008). S4-based voltage sensors have three major conformations. *Proc Natl Acad Sci USA* **105**, 17600–17607.

Wang Y, Li SJ, Wu X, Che Y & Li Q (2012). Clinicopathological and biological significance of human voltage-gated proton channel Hv1 protein overexpression in breast cancer. *J Biol Chem* **287**, 13877–13888.

Wisedchaisri G, Tonggu L, McCord E, Gamal El-Din TM, Wang L, Zheng N & Catterall WA (2019). Resting-State Structure and Gating Mechanism of a Voltage-Gated Sodium Channel. *Cell* **178**, 993-1003.e12.

Wu LJ, Wu G, Sharif MRA, Baker A, Jia Y, Fahey FH, Luo HR, Feener EP & Clapham DE (2012). The voltage-gated proton channel Hv1 enhances brain damage from ischemic stroke. *Nat Neurosci* **15**, 565–573.

Yang N & Horn R (1995). Evidence for Voltage-Dependent in Sodium Channels S4 Movement. *Neuron* **15**, 213–218.

Yu FH & Catterall WA (2004). The VGL-Chanome: A Protein Superfamily Specialized for Electrical Signaling and Ionic Homeostasis. *Sci Signal* **2004**, re15–re15.

Zhang W, Guan L & Kaback HR (2002). Helices VII and X in the lactose permease of Escherichia coli: Proximity and ligand-induced distance changes. *J Mol Biol* **315**, 53–62.

Zheng J & Trudeau MC (2015). *Handbook of Ion Channels*, first.ed. Zheng J & Trudeau MC. CRC Press Taylor and Francis Group, Boca Raton.

Zheng J & Zagotta WN (2000). Gating rearrangements in cyclic nucleotide-gated channels revealed by patch-clamp fluorometry. *Neuron* **28**, 369–374.

Zheng J & Zagotta WN (2003). Patch-Clamp Fluorometry Recording of Conformational Rearrangements of Ion Channels. *Sci Signal* **2003**, pl7–pl7.

Zhou Y, Guan L, Freites JA & Kaback HR (2008). Opening and closing of the periplasmic gate in lactose permease. *Proc Natl Acad Sci USA* **105**, 3774–3778.

Zhou Y, Madej MG, Guan L, Nie Y & Kaback HR (2011). An early event in the transport mechanism of LacY protein: Interaction between helices V and I. *J Biol Chem* **286**, 30415–30422.

7. Acknowledgments

This work was carried out in the Department of Molecular Sensory Systems at the Research Center caesar in Bonn, Germany. I would like to thank all staff members for their support and cooperation. Particularly, I want to thank the following persons:

Dr. Thomas K. Berger, for his incredible patience and careful supervision, his helpful advices for experiments, presentations, and for the writing of the thesis. You taught me a lot!

Prof. Dr. U. Benjamin Kaupp for providing an extraordinary scientific environment that allowed me to develop myself scientifically. Thank you for the possibility to attend lectures, seminars, and workshops. Thank you also for your constructive criticism after presentations and during the writing of the thesis!

Elena Grahn, Lea Wobig and Thérèse Wolfenstetter for being the perfect collaborators and friends, thank you for creating such a comfortable work atmosphere! I really enjoyed the time together with you!

Sybille Wolf-Kümmeth for the technical assistance

Prof. Dr. Christopher Volk for being part of my Thesis Advisory Committee and for the generous donation of frog oocytes

Prof. Dr. Günter Mayer, Prof. Dr. Waldemar Kolanus, and Prof. Dr. Gerhard von der Emde for being part of my exam committee and for taking their time to review this thesis

Heike Krause for the help with organizational challenges

And finally my friends and family for their huge support!

Eidesstattliche Erklärung nach § 6 (2) der Promotionsordnung

Teile dieser Arbeit sind bereits in unten aufgeführter Publikation veröffentlicht:

Schladt TM and Berger TK (2020). Voltage and pH difference across the membrane control the S4 voltage-sensor motion of the Hv1 proton channel. *Sci Rep* **10**, 21293.
Doi: 10.1038/s41598-020-77986-z

Publications

Miras M, Pottier M, **Schladt TM**, Ejike JO, Redzich L, Frommer WB, Kim JY (2022). Plasmodesmata and their role in assimilate translocation. *J Plant Physiol* **270**, 153633. Doi: 10.1016/j.jplph.2022.153633.

Schladt TM and Berger TK (2020). Voltage and pH difference across the membrane control the S4 voltage-sensor motion of the Hv1 proton channel. *Sci Rep* **10**, 21293. Doi: 10.1038/s41598-020-77986-z

Molina-Obando S, Vargas-Fique JF, Henning M, Gür B, **Schladt TM**, Akhtar J, Berger TK & Silies M (2019). On selectivity in the drosophila visual system is a multisynaptic process involving both glutamatergic and GABAergic inhibition. *eLife* **8**, 1–34. Doi: 10.7554/eLife.49373

Mycielska ME, Dettmer K, Rümmele P, Schmidt K, Prehn C, Milenkovic VM, Jagla W, Madej GM, Lantow M, **Schladt TM**, Cecil A, Koehl GE, Eggenhofer E, Wachsmuth CJ, Ganapathy V, Schlitt HJ, Kunzelmann K, Ziegler C, Wetzel CH, Gaumann A, Lang SA, Adamski J, Oefner PJ, Geissler EK (2018). Extracellular citrate affects critical elements of cancer cell metabolism and supports cancer development in vivo. *Cancer Res* **10**, 2513-2523. Doi: 10.1158/0008-5472.CAN-17-2959

Schladt TM, Nordmann GC, Emilius R, Kudielka BM, de Jong TR & Neumann ID (2017). Choir versus Solo Singing: Effects on Mood, and Salivary Oxytocin and Cortisol Concentrations. *Front Hum Neurosci* **11**, 430. Doi: 10.3389/fnhum.2017.00430

Jendryke T, Prochazkova M, Hall BE, Nordmann GC, **Schladt TM**, Milenkovic VM, Kulkarni AB & Wetzel CH (2016). TRPV1 function is modulated by Cdk5-mediated phosphorylation: Insights into the molecular mechanism of nociception. *Sci Rep* **6**, 22007. Doi: 10.1038/srep22007